Multibody Approach to Controlled Removal of Large Space Debris with Flexible Appendages

Sunayna Singh

Delft University of Technology

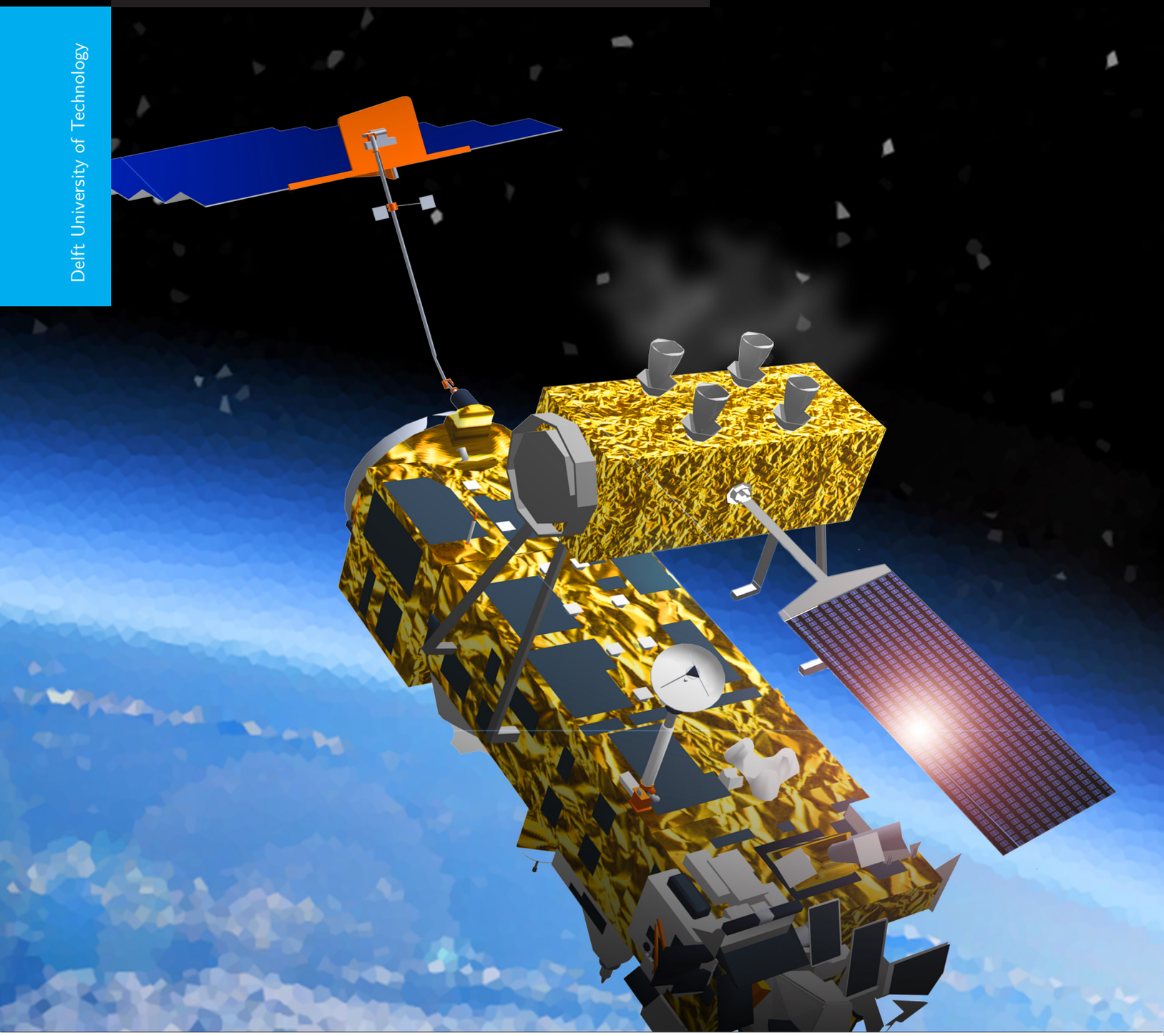

TU Delft Delft University of Technology

Challenge the future

Multibody Approach to Controlled Removal of Large Space Debris with Flexible Appendages

MSc Thesis Report

by

Sunayna Singh

to obtain the degree of Master of Science
at Delft University of Technology,

Student number:	4614399	
Supervisor:	Dr. Ir. E. Mooij	TU Delft
Secondary Supervisor:	Dr. Ir. Derek Gransden	Laurentian University
Thesis committee:	Dr. D. M. Stam	TU Delft
	Dr. Ir. Q. P. Chu	TU Delft
	Dr. Ir. M. Ellenbroek	University of Twente

An electronic version of this thesis is available at `http://repository.tudelft.nl/`.

TU Delft

It is difficult to say what is impossible, for the dream of yesterday is the hope of today, and the reality of tomorrow.

-Robert H. Goddard

Summary

The space environment is ever-changing with the space structures getting larger and the orbits getting increasingly crowded with time. This creates a need for removal of large defunct satellites to avoid the disastrous Kessler syndrome, which poses a major threat to the future of space exploration. According to NASA and some other sources, about 5-10 large objects must be removed annually from the crowded low Earth orbit to stabilise the current situation. Therefore, this research examines the dynamics and control involved in the active removal of a large space debris, Envisat. European Space Agency's e.deorbit mission aims to deorbit Envisat using a chaser satellite, which synchronises with Envisat's rotational motion, docks with it, and detumbles and deorbits the stacked (docked) configuration. In this research, two phases of this mission are modelled, namely the synchronisation and connected phase. In the synchronisation phase, the chaser matches the attitude of the tumbling passive target. Then, in the connected phase, the stacked configuration detumbles to zero angular velocity and reorients itself to a particular attitude to perform the deorbitation manoeuvre.

The presence of large flexible appendages makes the configuration prone to elastic perturbations leading to complex dynamics that cannot be represented using rigid body dynamics. Hence, a unique multibody approach based on the absolute interface coordinates in the floating frame formulation is used to model the Flexible Multibody Dynamics (FMD). The new method proves to be efficient for the control application, while facilitating easy constraint handling. The satellite model is adapted to the new modelling technique using beams to model the solar panels. The rigid body inertia is captured in the multibody formulation using lumped masses.

The controllability characteristics of the two phases of the e.deorbit mission are analysed using a linear PD controller and an Incremental Nonlinear Dynamic Inversion (INDI) controller. To analyse the effect of unpredicted flexible perturbations on controller performance, the control system is designed using rigid body dynamics and the environmental torques are excluded from the dynamics. Additionally, it is assumed that the rotational motion of the system is decoupled from the translational motion. In other words, the satellite remains stationary in its orbit during the whole operation.

For the first phase, both controllers successfully synchronise the chaser with the target debris tumbling at the rate of 3.5 °/s about all axes. The system was controlled, even without structural damping in the flexible system. However, during the connected phase, the detumbling manoeuvre introduces complex dynamics due to the large appendage (14.2 m) in the stacked configuration, which could not be stabilised by the applied controllers. It was found that without damping, the oscillations increase with time and destabilise the system. Also, large control moments act like impulsive forces to the flexible elements and aggravate the vibrations. Inclusion of structural damping (2%) and use of smaller control moments, improved the controllability characteristics considerably and the system achieved convergence with very small oscillations ($\pm 0.1^\circ$/s) for both controllers. Nonetheless, INDI proved to be more stable and showed faster convergence compared to PD, since smaller vibrations are observed in the flexible elements.

Preface

This research study aims to analyse the dynamics and control associated with the active removal of a large uncooperative debris with a large flexible appendage. Through this application, the capabilities of a new multibody modelling technique, which provides a good balance between accuracy and computation time, is demonstrated. Through this study, I hope to reach out to the scientific community to work towards a sustainable future, not only on Earth, but also beyond it.

I would like to start with expressing my gratefulness to my supervisor, Erwin Mooij, for pushing me to do my best and keeping me motivated through the ups and downs of the research. I would also like to thank my secondary supervisor, Derek Gransden for his great "over the seas" supervision. A heartfelt gratitude to Marcel Ellenbroek, for without his support this research would not have been a success. Further thanks to Jurnan Schilder and Koen Dwarshuis, from the University of Twente, for being so helpful and available during the study. Also, thanks to Varun Jois for his endless patience and faith in me. I would also like to thank my mother for helping me keep my calm and focus, and my grandparents for believing in me beyond all odds. Lastly, I would like to thank my friends for their love and support.

Sunayna Singh
Delft, Dec 2018

Contents

List of Acronyms

ADR Active Debris Removal

AOCS Attitude and Orbit Control System

CoM Centre of Mass

DCM Direction Cosine Matrix

DOF Degree of Freedom

ECI Earth Centred Inertial

EOM Equations of Motion

ESA European Space Agency

FEM Finite Element Method

FMD Flexible Multibody Dynamics

FMS Flexible Multibody System

GEO Geostationary Earth Orbit

GNC Guidance, Navigation and Control

IADC Inter-Agency Space Debris Coordination Committee

ISS International Space Station

LEO Low Earth Orbit

LPM Lumped Parameter Model

LQR Linear Quadratic Regulator

LVLH Local Verticle Local Horizontal

MRP Modified Rodrigues Parameters

NASA National Aeronautics and Space Administration

RCS Reaction Control System

RP Rodrigues Parameters

RVD Rendezvous and Docking

SSO Sun Synchronous Orbit

List of Symbols

Symbol	Description	Units
Roman		
$[\boldsymbol{A}]$	Compound matrix containing an assembly of $\boldsymbol{A}$ matrices	-
$\boldsymbol{C}_{\boldsymbol{A}}^{\boldsymbol{B}}$	Transformation matrix from frame A to frame B	-
$\boldsymbol{C}$	Direction Cosine Matrix	-
$\boldsymbol{C}$	Damping Matrix	Nm/s
d	Distance	m
E	Energy	J
E	Modulus of Elasticity	N/m^2
$\boldsymbol{e}$	Control error	-
$\hat{\boldsymbol{e}}$	Unit vector along Euler's Eigenaxis	-
$\boldsymbol{F}$	Applied force	N
$\mathscr{F}_I$	Inertial frame for rigid body model	-
$\mathscr{F}_B$	Body fixed frame for rigid body model	-
f_n	n^{th} natural frequency	Hz
$\boldsymbol{H}$	Angular momentum vector	Nms
$\boldsymbol{I}$	Inertia tensor, with elements I_{ij}	kgm^2
$\boldsymbol{K}$	Stiffness matrix	N/m
$\boldsymbol{K_p}$	Proportional gain vector	Nm/rad
$\boldsymbol{K_d}$	Derivative gain vector	Nms/rad
$\boldsymbol{K_{CB}}$	Stiffness matrix after Craig Bampton reduction	N/m
$\mathscr{L}$	Lagrangian	J
L	Length of element	m
$\boldsymbol{l}$, $\boldsymbol{M}$	Jacobian in INDI controller design	various
$\boldsymbol{M}$	Mass matrix	kg
$\boldsymbol{M}$	External moment (g = gravity, d = disturbance, c = control)	Nm
$\boldsymbol{M_{CB}}$	Mass matrix after CB reduction	kg
$\boldsymbol{N}$	Shape-function vector	-
$\boldsymbol{N}, \boldsymbol{\Gamma}$	Coefficient matrices representing kinematics in NDI and INDI controllers	-
$\boldsymbol{p}, \boldsymbol{q}$	Quaternion vector	-
$\boldsymbol{Q}$	Elastic deformation matrix	-
$\boldsymbol{Q}$	Quaternion transmuted matrix	-
$\boldsymbol{Q_i}$	Non-conservative force vector for generalised coordinate i	-
$\boldsymbol{q}_{\boldsymbol{j}}^{\boldsymbol{i,i}}$	Generalised coordinates of point P_j with respect to floating frame defined at P_i	-
$\boldsymbol{R_i}$	Resultant force acting on particle i	N
$\boldsymbol{r}_{\boldsymbol{i}}^{\boldsymbol{A,B}}$	Position vector of a point P_i in frame A relative to frame B	m
$\boldsymbol{r}$	Rodrigues Parameters vector	-
T	Kinetic energy	J
$\boldsymbol{T^i}$	Transformation matrix defining the relationship between absolute and local motion of the interface coordinates	-

U	Potential energy	J
$\boldsymbol{u}$	Control vector	Nm
$\boldsymbol{u}_j^{i,i}$	Small elastic displacement vector of point P_j with respect to floating frame defined at P_i	-
$\boldsymbol{v}$	Virtual control vector	-
$\boldsymbol{v}_j^{o,o}$	Absolute velocity vector of point P_j	m/s
$\boldsymbol{v}_j^{i,i}$	Relative velocity vector of point P_j with respect to floating frame defined at P_i	m/s
W	Work	Nm
$\boldsymbol{x}$	State vector	-
X_G, Y_G, Z_G	Location Centre of Mass	m
$\boldsymbol{x}_j^{i,i}$	Position vector of point P_j with respect to floating frame defined at P_i	m
$\boldsymbol{Z}^i$	Transformation matrix defining the relationship between absolute motion of interface coordinates and floating frame	-

Greek

α	Mass proportional damping coefficient	-
$\boldsymbol{\alpha}$	Penalty factor matrix	-
β	Stiffness proportional damping coefficient	-
$\boldsymbol{\Gamma}$	Modal participation matrix	-
$\boldsymbol{\delta_e}$	Nodal degrees of freedom vector	-
θ	Euler angle about Y-axis (pitch)	rad
$\boldsymbol{\theta}$	Euler angle vector	rad
$\boldsymbol{\Theta}$	Pseudo Euler angles vector	rad
$\boldsymbol{\lambda}$	Lagrange multipliers vector	-
ξ	Critical damping ratio	-
ρ	Density of the element	kg/m^3
$\boldsymbol{\sigma}$	Modified Rodrigues parameters vector	-
ϕ	Euler angle about X-axis (roll)	rad
$\boldsymbol{\phi}_{\boldsymbol{CB}}^{\boldsymbol{i}}$	Vector containing CB modes of vibration with respect to floating frame defined at point P_i	rad/s
$\boldsymbol{\phi}_{\boldsymbol{rig}}^{\boldsymbol{i}}$	Vector containing rigid body modes of vibration with respect to floating frame defined at point P_i	rad/s
ψ	Euler angle about Z-axis (yaw)	rad
$\boldsymbol{\psi_c}$	Constraint modes matrix	-
$\boldsymbol{\Omega}$	Skew symmetric matrix of angular velocities	rad/s
ω	Natural frequency	rad/s
$\boldsymbol{\omega}$	Angular velocity vector	rad/s
$\boldsymbol{\omega}_{\boldsymbol{i}}^{\boldsymbol{A,B}}$	Angular velocity vector of a point P_i in frame A relative to frame B	rad/s

1 Introduction

Since the onset of Space Age, the number of satellites launched every year has been increasing progressively. Unfortunately, most objects launched into space are still orbiting Earth, even though only a small fraction of them are operational. All these man-made objects in space, which no longer serve a useful purpose, can be defined as space debris. This accumulating debris has become a major threat to current and future space exploration. Thus, to address this problem, the Inter-Agency Space Debris Coordination Committee (IADC) was formed in 1993, with the goal of achieving international co-operation in space debris research and mitigation options.

1.1. The Background

Varying sizes of space debris are produced in many stages of a spacecraft's lifetime. It includes jettisoned rocket bodies, objects released during missions, fragments due to collisions, and uncontrolled dead satellites. While in space, a small 1 cm debris can hit with a force of a hand grenade. There are more than 17,000 trackable objects larger than a coffee cup, posing great risk of collision with the current missions (ESTEC, 2015). An instance of such damage is the solar panel on the Sentinel-1A satellite, which was hit by a millimeter-sized particle as shown in Figure 1.1. The damage, however, was about 100 times its diameter [1].

According to Donald J. Kessler from the National Aeronautics and Space Administration (NASA), if the growth is not controlled, the amount and density of debris in Low Earth Orbit (LEO) will reach a threshold. At that point, the debris will collide with each other leading to a cascade of collisions, thereby leading to an exponential growth of debris (Kessler and Cour-Palais, 1978). Since 1961, more than 300 satellite fragmentation events have already been documented. Some of them are head-on collisions, which produced thousands of fragments, with two such events occurring in the recent past. The first one is the explosion of the anti-satellite missile launched by China in January 2007, which produced more than 3,200 pieces of debris in one of the most populated orbits of operation, at about 850 km altitude. The second event that produced around 2,100 pieces of documented debris was the collision of Iridium 33 and Cosmos 2251 at an altitude of 790 km in 2009 (IADC, 2011). The effects of these events can be seen as a sharp rise of the total debris population in Figure 1.2, which shows the number of catalogued debris, and their growth over years. This number drastically increased from 11,000 to 14,000 in 2007, and from 15,000 to 17,000 in 2009, indicating how one incident can cause an exponential surge in the debris population. Sometimes, short-lived debris are also produced, either accidentally or deliberately. According to IADC (2011), on an average about five catalogued debris are separated from the International Space Station (ISS) every year. Other

[1] https://qz.com/773511/photos-this-is-the-damage-that-tiny-space-debris-traveling-at-incredible-speeds-can-do/, Last Accessed: 12/02/2018

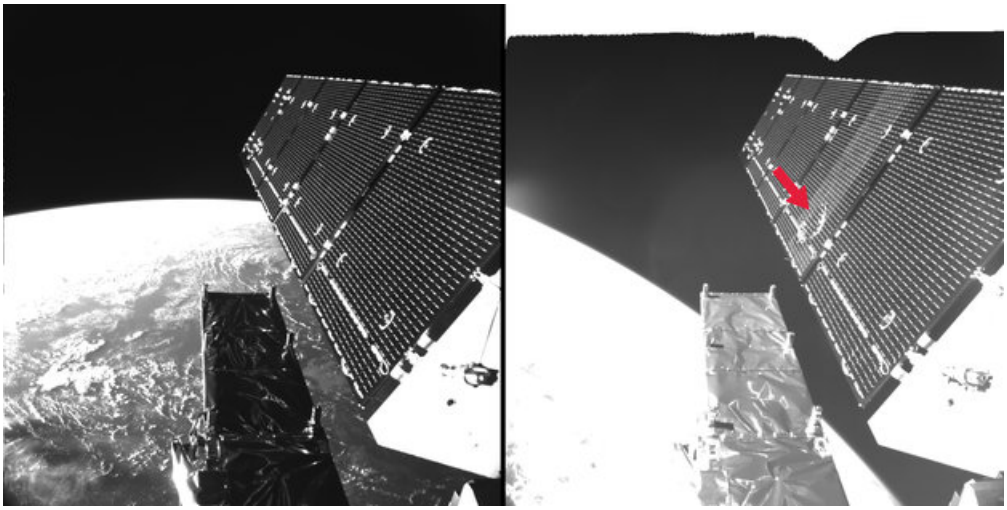

Figure 1.1: Space debris impact on Sentinel-1A satellite

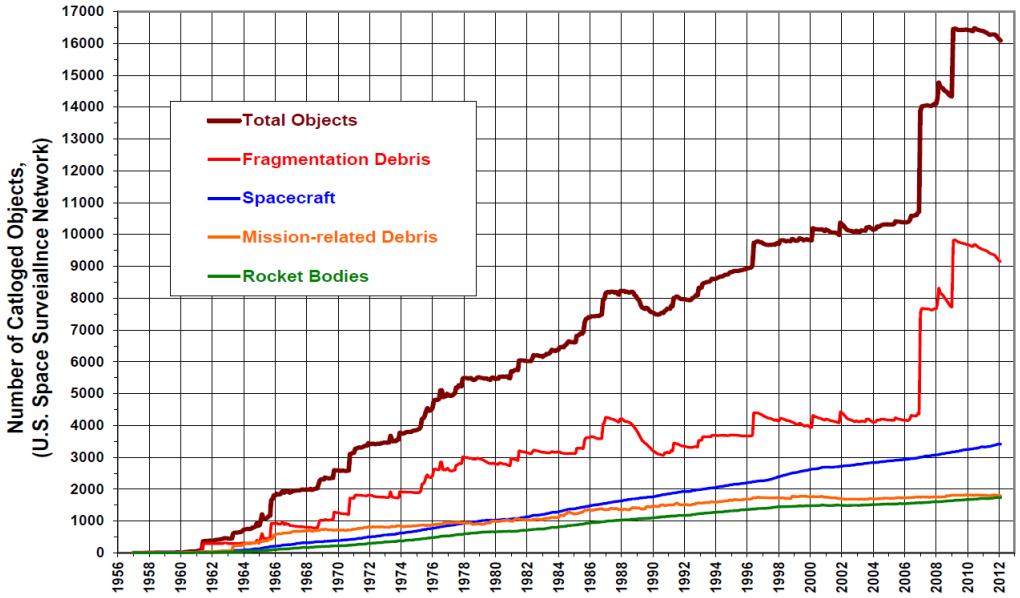

Figure 1.2: History of catalogued debris (IADC, 2011)

sources, like NASA (2008) and Johnson (2006), suggest six and four catalogued debris per year, respectively .

The most populated region in space is LEO, which extends to an altitude of 2000 km. LEO is not only populated by satellites, but also by 75% of the catalogued space debris (which can be attributed to the recent collisions in 2007 and 2009). A special type of polar orbit at an altitude of 800-900 km, known as Sun Synchronous Orbit (SSO), is especially populated by satellites. The availability of solar energy at all times, small repeat cycles and good resolution make it an ideal orbit for Earth observation satellites. This makes SSO a densely populated orbit with high collision risk. The current scenario of space debris in Geostationary Earth Orbit (GEO) and LEO can be visualised with the help of Figure 1.3. Moreover, for satellites in higher orbits where the atmospheric drag is not very evident, orbit decay can take centuries. Simulations have shown that even if there are no more satellites launched into this orbit, the debris will continue to grow exponentially.

Since the collision in 2009, the risk of further collisions has elevated alarmingly. An average of

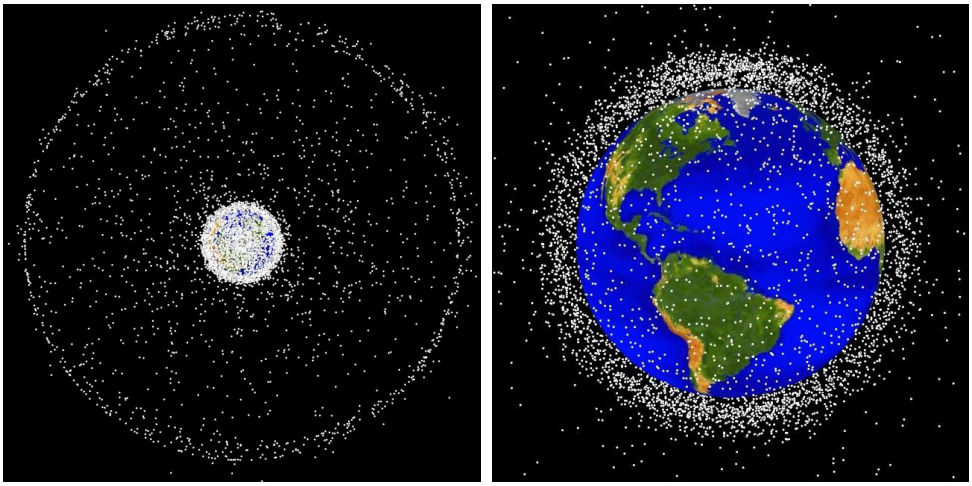

(a) Geostationary Orbit (b) Low Earth Orbit

Figure 1.3: A visualisation of debris distribution in GEO(left) and LEO(right) Image credits: ESA

10-30 close-approach warnings are now transmitted everyday from the U.S. Joint Space Operations Center to satellite operators around the world. In case of risk, the active satellites conduct collision avoidance manoeuvres. In LEO, an approach of debris within 1 km of an operational satellite can lead to a collision avoidance manoeuvre; in GEO, this distance is about 5 km (IADC, 2011). It is possible to avoid collisions of active satellites with documented objects, but without adequate collision avoidance capabilities of the inactive satellites and other debris, there is still a large probability of collisions. Hence, it is not sufficient to avoid collisions between the active satellites, and there is a need to remove any large debris, which can cause a further increase in the debris population. This process is called Active Debris Removal (ADR). According to NASA, at least five large objects need to be removed annually from LEO to stabilise the current situation (IADC, 2011), while the European Space Agency (ESA) suggests an order of 5-10 objects to be removed (ESA, 2017).

1.2. e.deorbit

The e.deorbit mission is part of the Clean Space Programme managed by ESA, which aims to mitigate the space debris scenario and bring increased attention to environmental impacts of its activities in space. The e.deorbit specifically aims at developing new technologies for actively removing debris. Its mission objective, as stated in the ESA (2012) report, is:

> *"The mission aims to perform the active removal of a big ESA owned object from its orbit. By doing so the mission shall actively contribute to the mitigation of the risk of orbital environment degradation due to in-orbit collisions (Kessler syndrome) and demonstrate the required technologies for future ADR missions."*

The "big ESA owned object" stated here is ESA's largest Earth observation satellite, Envisat, which is inoperable since April, 2012. The debris now poses the highest collision risk of all ESA owned satellites in the densely populated altitude of 600-800 km near polar orbit and is an important case study for ADR technology. Some key concepts developed for removal of Envisat are the capturing of debris using:

- Tethers,
- Throw-nets,
- A harpoon, or

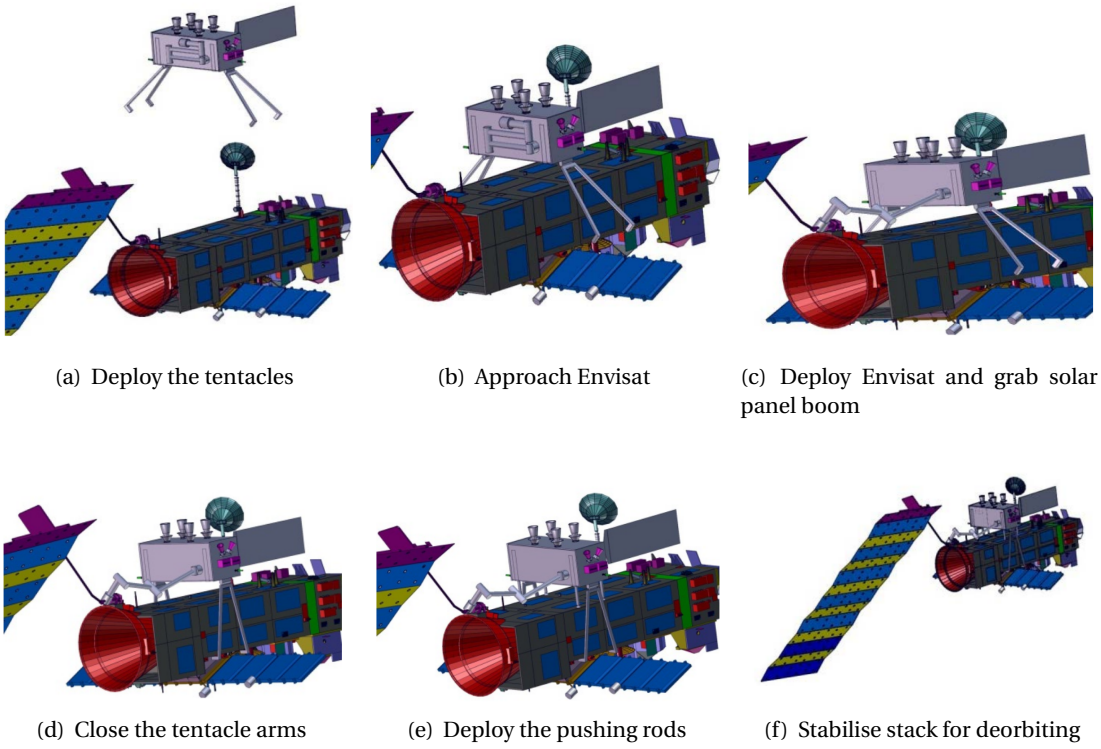

(a) Deploy the tentacles (b) Approach Envisat (c) Deploy Envisat and grab solar panel boom

(d) Close the tentacle arms (e) Deploy the pushing rods (f) Stabilise stack for deorbiting

Figure 1.4: Phases of e.deorbit mission showing interaction of chaser with Envisat (ESA, 2012)

- Tentacles or clamps.

Other less popular concepts include de-orbiting using ion-beam, expanding foam and hybrid sails. Among all options stated above, a chaser with tentacles and a robotic arm to capture the target is among the most promising ones (ESA, 2012), and will also be investigated in further detail in this research.

For this ADR option, the mission starts with the launch and injection of the chaser satellite to an altitude of 300 km into an orbit co-planar to that of Envisat. The chaser approaches the target orbit using Hohmann transfers and commences the rendezvous phase at a relative distance of 3 km. At a distance of about 50 m from the target, the chaser observes the target and starts synchronising with its tumbling attitude (Deloo, 2015). It then docks with the target using tentacles and/or a robotic arm. Finally, it stabilises the attitude of the stacked system and eventually de-orbits it.

The process can be visualised using Figure 1.4. The figure shows six steps, wherein the chaser first deploys its tentacles and prepares for contact with Envisat. Once it is close enough to establish contact, it grabs the solar panel beam using the robotic arm. The tentacles lock themselves around the body of Envisat and push rods are deployed to establish a rigid connection. Lastly, the chaser stabilises the stack for the de-orbiting manoeuvre.

1.3. Problem Statement

In all of the above mentioned phases in the e.deorbit mission, a number of flexible elements, like the robotic arm and the tentacles, are involved. Additionally, both spacecraft have solar panels, which add to the flexibility of the system. According to Junkins and Kim (1993), spacecraft with smaller appendages are often modelled as rigid bodies due to their relatively dominant rigid properties. However, with the configuration of Envisat, which includes a 14.2 m long flexible solar panel, large vibrations can be introduced in the system. Assuming a rigid configuration for long appendages

can overlook important physical properties, like the vibrational and rotational coupling of the rigid and flexible elements. This might lead to faulty models, which can be potentially catastrophic leading to loss of control of the satellite. Also, the presence of large flexible appendages and multiple bodies stacked into one configuration, characterises a nonlinear flexible multibody problem. Such a multibody configuration, with slewing, and translating members in the presence of external disturbances, presents numerous challenges to the field of dynamics and control.

The flexible elements, like any other part of the spacecraft, interact with the space environment, which in turn causes vibrations that can lead to disruptions in the spacecraft attitude. Then, Envisat's uncontrolled attitude adds to the perturbations in these flexible elements. Lastly, control torques applied on the system to attain the required attitude can act like a discrete force to the flexible elements, possibly exciting their natural frequencies of vibration. Clearly, the ADR not only requires state-of-the-art sensors, but also a very robust control system to successfully perform autonomous rendezvous and docking operations, despite all the external disturbances. Once the connection between the Chaser and Envisat is established, the system becomes very dynamic and complex due to the flexibility in the connection itself.

From the above discussion, it can be concluded that there is a large scope of research to address this problem. The dynamics associated with a flexible chaser satellite docking with a large uncontrolled flexible target is especially very intriguing, and different possibilities of formulating such a system will be addressed in further detail in this research. Since the vibrations in the appendages of typical satellite systems are difficult to predict and act like external disturbances to the rigid body attitude, it would be interesting to observe the performance of a control system based on rigid body motion, for a system that is driven by flexible dynamics. Currently, many satellites are controlled by relatively simple, linear controllers. So, another interesting aspect would be to analyse the performance of a linear controller for such a dynamic nonlinear system. The alternative of using a nonlinear controller will also be explored, and the advantages and disadvantages will be weighed against the aforementioned controller. This will help with the understanding of how flexible dynamics of a multibody system affects the controller performance, originally developed for controlling rigid body motion.

Another problem associated with the field of dynamics and control of large flexible space structures is the computation time. Typical software that give reasonable accuracy for such complex structures have high rendering time. Further, modelling of joints or constraints between two bodies along with asymmetric structures and material properties can prove to be cumbersome in operation with the controls. Hence, there is a need for development of modern techniques, which provide good accuracy in the modelling of dynamics, in combination with fast computation time for control applications, while enabling easy constraint modelling. Therefore, a new and unique multibody approach based on floating reference frames, which enables modelling of constraints in a multibody system without the use of Lagrange multipliers, will be used to model the dynamics in this research. The new method proposed by Ellenbroek and Schilder (2017) may facilitate good accuracy with relatively low computation time. To summarise, the research will attempt to examine the integrated dynamics and control of docking with a large tumbling debris with flexible elements.

1.4. Research Question

For this research, the attitude control of a chaser in the vicinity of a target debris will be studied, taking into account the structural dynamics of the two flexible bodies and the stack after docking. For a better analysis, the docking phase can be divided into three sub-phases:

1. *Synchronisation*: In this phase, the system consists of two spacecraft bodies with flexible appendages, which are completely unconnected. The chaser matches the uncontrolled attitude of Envisat. The configuration can be defined as two bodies with one rigid hub and one flexible panel each. Environmental disturbances and flexibility cause perturbations in both space-

craft individually.

2. *Semi-connected*: In this phase, the contact is achieved between the target and chaser, but a rigid connection is not achieved yet. The system is connected by flexible links and prone to additional torques due to attitude differences. The system configuration can be defined as one body with two rigid hubs and two flexible panels connected by a flexible link. It can be visualised as a chain structure with alternating rigid and flexible bodies.

3. *Connected*: In this phase, a relatively more rigid connection is established. Now, the system consists of combined mass and inertia properties, and the chaser makes manoeuvres to stabilise the stacked system. The system configuration can now be defined as a large rigid hub with two flexible panels.

A good attitude control system should be able to achieve the target attitude when unconnected, maintain the attitude in the semi-connected phase, and finally, completely stabilise the stacked system in the connected phase in the presence of perturbations coming from the environment and flexible dynamics. Also, an efficient dynamics model should provide an accurate representation of the system's dynamics during all three phases with good computation time. Since the presence of flexible links between the two satellites in the semi-connected phase can create very complex and specific dynamics, which requires exclusive attention, this phase will not be modelled and analysed in this research.

Therefore, in this research the dynamics of the multibody system will be modelled and controllability characteristics of this system will be analysed for the synchronisation and connected phase of the mission, treating the vibrations due to flexibility as external disturbances. Therefore, the research question can thus be formulated as:-

> *What are the dynamics and controllability characteristics of a flexible chaser spacecraft before and after docking with a large, flexible and uncooperative space debris?*

From this, further questions that can be asked in this research are:

- Does the new multibody technique demonstrate good compatibility with the modelling and control of the flexible multibody system in both synchronisation and connected phases?
- What are the complications introduced in the control of the system due to coupling of rigid and flexible body dynamics?
- Can simple controllers designed for rigid bodies stabilise the system in the presence of flexible perturbations?
- What are the structural aspects that affect the vibrations in the flexible elements?
- How does the controllability of a flexible system differ from that of a rigid system?
- How does a linear controller perform for such a nonlinear dynamic system?
- Will the application of a nonlinear controller show improved response characteristics?

In this research, all the aspects associated with the above stated questions will be analysed.

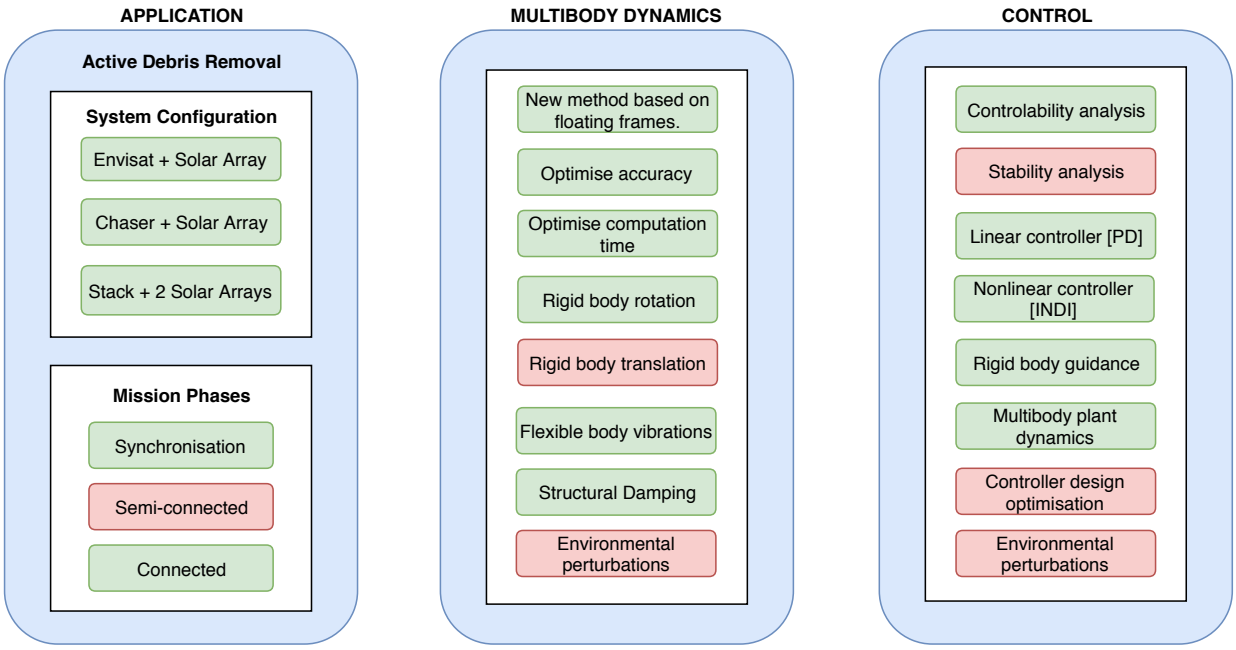

Figure 1.5: Scope of the research

1.5. Scope of the research

As shown in Figure 1.5, the thesis is focussed on three main elements. The first aspect is the application, which is chosen to be the significant function of ADR, with a focus on removing large debris with flexible appendages. The reference debris used for this research is that of Envisat. The chaser models and mission phases examined will also be based on the frame of reference of the e.deorbit mission, which aims to deorbit Envisat. The system configuration will include three different systems. However, only two phases of the mission (synchronisation and connected phase) will be examined.

The next prospect of this thesis is the multibody dynamics, which is derived from the system configuration consisting of a mix of rigid and flexible elements. For this, a new modelling technique, which provides the combined advantage of easy constraint modelling with good accuracy and computation time will be used. The dynamics will be defined only for the rotational state (which is also controlled), and the satellites will be assumed to be stationary in their orbits during the operation. To improve the chances of stabilising the system in the presence of flexible perturbations, structural damping is included in the modelling. Lastly, to analyse the impact of flexibility alone on the controllability characteristics, the effect of external perturbations will be ignored.

The final aspect of this research is the control system. The system will be assessed for its controllability characteristics in both synchronisation and connected phases. This will be performed for two types of controllers, one linear and one nonlinear. The control system will be designed for a rigid body, but applied to a plant based on Flexible Multibody Dynamics (FMD) to analyse the effects of unprecedented flexible perturbations on controller performance. Again, the effect of environmental perturbations is ignored. The performance of the controllers will be analysed in their elementary state and no optimisation will be performed for the control system design.

1.6. Overview of the Report

Attitude control of such a complex flexible chaser-target system before and after docking, requires numerous models to be put together. To model the dynamics accurately, some common characteristics associated with flexibility in large multibody space structures, performing different opera-

tions must be understood. Also, the Attitude and Orbit Control System (AOCS) configuration used for attitude control of these large structures should be analysed. This is discussed in Chapter 2 as a part of the mission heritage. The important properties of chaser and target spacecraft, which together form the system configuration, are also discussed in this chapter along with the environment model. Lastly, mission and system requirements are derived for the e.deorbit mission in light of this research.

Defining the attitude of a spacecraft requires reference frames and attitude-state representations, which are introduced in Chapter 3. Since the rigid body dynamics forms the basis of the guidance system, the Equations of Motion (EOM) are first derived for rigid body motion. Then, the guidance system for different phases of the mission is defined. The theory and motivation behind the chosen linear and nonlinear controllers is also explained in this chapter. Lastly, some benchmark simulations are made with a rigid system to verify the working of the control system and also, to compare the performance of the two controllers.

In Chapter 4, the flexible dynamics for the multibody system is defined. Common multibody approaches are introduced and compared to motivate the choice of the new multibody modelling technique. Different components involved in modelling of a multibody system, such as discretisation methods, constraint modelling, model reduction and internal forces, will be introduced and compared. Then, the new methodology based on floating frames, wherein the dynamics is represented using absolute interface coordinates, is used to derive the generalised EOM for the system. These EOM will be used as the plant for the control system analysis.

Now that all elements for the control systems are introduced, the simulator architecture is explained in Chapter 5. The plant model based on FMD is also verified and validated against some established test cases from literature. Next, Chapter 6 discusses the methodology behind structurally adapting the satellite model to the new formulation. Some sensitivity studies are performed to select the most fitting properties to model both rigid and flexible elements. This is followed by a schematic of the final configuration of the satellite structural model. Lastly, the mathematical formulation of damping is discussed in this chapter and some results of its effect on dynamics are presented.

Finally, the results from the simulations are presented and analysed in Chapter 7 for the two phases of the mission, using different controllers. Based on these results conclusions are drawn about the final outcome of the research in Chapter 8. Some recommendations to further develop and improve the models, and extend the research, are also made in this chapter.

2

Mission Heritage

Over the past few decades, space structures have become larger with high power requirements, which entails large flexible solar panels due to the ample availability of solar energy. This has brought a diverse set of challenges to the field of spacecraft attitude dynamics and control. According to Junkins and Kim (1993), spacecraft with smaller appendages have a dominant rigid property and can be modelled as a rigid structure. However, large appendages can cause considerable disturbing torques due to vibration, leading to instabilities in the system, and therefore cannot be modelled as a rigid body. A comparative study of the rigid and flexible models of attitude maneouvre of multi-body satellites by Teoh et al. (2014), shows that flexibility of solar panels can have significant effect on the satellite attitude dynamics by inducing a sinusoidal component in the attitude. Further, their results show that a flexible model provides a more precise attitude control model. Junkins and Kim (1993) also discuss how assuming a rigid configuration for long appendages can overlook important physical properties like the vibrational and rotational coupling of the rigid and flexible elements. This might lead to faulty models, which can be potentially catastrophic. Hence, the FMD of the system becomes crucial in such cases.

The study of large flexible multibody space systems includes analysis of dynamics associated with many applications and operations performed by these structures. This includes assembly and docking of large space structures, deployment and retrieval of appendages, slew manoeuvres and precision pointing, and lately, active removal of space debris, all to be controlled in the presence of disturbing environmental forces. Elastic perturbations are also introduced due to vibration of the flexible elements like solar panels, robotic arms, and any other parts, which are elementally flexible (for example, joints). In addition, many spacecraft suffer from disturbances associated with fuel sloshing, which aggravate the vibrations induced due to other flexible elements. This chapter addresses certain problems associated with large flexible space structures, which will be studied through a brief outlook of the mission heritage. Nonetheless, the importance of modelling flexibility and its dependency on other prospects in space will be established. The end goal is to understand the typical structural and AOCS configuration used to control the perturbations induced due to flexibility in these structures. Also, the configuration associated with the e.deorbit mission for ADR of Envisat will be discussed in detail. At the end of the chapter, some mission and system requirements will be defined based on this mission heritage.

2.1. Effect of External Torques on Flexibility

A great example of the effect of external torques on the flexible dynamics of a spacecraft is ESA's successful mission to comet 67P/Churyunov-Gerasimenko, Rosetta. The spacecraft was launched in 2004, and after a hibernation period, arrived at the comet in August 2014 and the mission ended

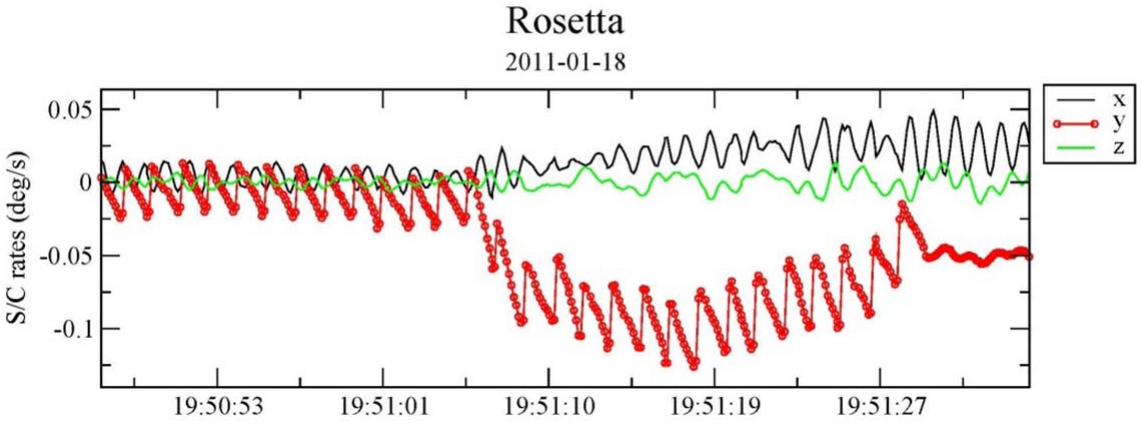

Figure 2.1: Vibrations observed in angular velocity of Rosetta ESTEC (2017)

in September 2016. It is known for being the first deep-space mission ever to entirely rely on solar power generation beyond the main asteroid belt, where the sunlight is 3-4% of that in the LEO. The mission aimed to study the nucleus and environment of the comet for nearly 2 years and also attempted to land a probe on its surface. The 2.8 x 2.1 x 2.0 m orbiter was equipped with two 14 m long solar array wings, which gave reasonable performance at temperatures as low as -100°C. Each wing consisted of five solar panels each of dimensions 2.25×2.74 m. The spacecraft hub had a configuration of 24 thrusters arranged in parallel pairs (12 prime and 12 redundant). Out of them, eight pairs located at the corners of the hub with 10 Nm capacity, were used for attitude control. The remaining four pairs were used for ΔV manoeuvres. Additionally, it had four reaction wheels of 40 Nm capacity, also for attitude control (Stramaccioni, 2017).

One of the main perturbing forces considered in the design of AOCS in Rosetta was the coma drag from the comet as mentioned in Godard et al. (2015). Since the coma drag is directly proportional to the surface area, the intensity of drag affecting the solar panels is more than the spacecraft bus (the area is larger). This drag can induce torques on the solar panel, which may cause instability in the spacecraft attitude. Indeed, during the period when the comet was at its perigee close to the Sun, the coma drag became so evident that the spacecraft had to move away from the comet (still orbiting) to avoid any accumulation of dust or ice on the panels and also to avoid the disturbing torque. Further, the mission involved multiple gravity-assisted manoeuvres and rendezvous with the comet. These activities induced vibrations in the large solar panels, thereby causing attitude disturbances. Figure 2.1 shows that during the mission, even with the operational controllers, the vibrations could not be damped out completely. Therefore, Rosetta is a good case study to analyse the dynamics of spacecraft with large flexible appendages, when exposed to large environmental disturbing torques.

The effect of perturbing forces is also very evident in the vicinity of Earth. Satellites in LEO are exposed to a number of perturbing forces due to atmospheric drag, solar radiation pressure, gravity gradient, and the Earth's magnetic field. Another perturbation that is observed by LEO satellites, is the effect of thermal snap. When the thermal environment around a flexible structure in orbit, such as a solar array, experiences substantial temperature change, vibrations can be induced due to thermal expansion or contraction. These thermal snap vibrations occurring on a flexible solar array are very low frequency, and measuring the motion using sensors, like accelerometers, is very difficult (Oda et al., 2011). The Hubble Space Telescope (HST) was launched on April 25, 1990, to conduct higher-accuracy astronomical observations than ground-based equipment. A pointing control system of HST was designed to hold an image stable at the HST focal plane to 0.007 arcsec (rms) for the

duration of an observation (Oda et al., 2011). However, following the deployment of solar arrays, it suffered from constant attitude errors, which was later found to be thermally induced. The bending motion of the arrays due to the thermal snap occurred rapidly during sunshine/ eclipse transition and disrupted HST's pointing system. In December 1993, the solar array paddles were replaced with new units to counter the problem.

Even though the effect of the environmental perturbations is not taken into account in this thesis, the analysis is important for the future work wherein these effects should be included in the robust controller development.

2.2. On-orbit Assembly of Large Space Structures

As space structures get larger, launching them into orbit as a completely assembled structure becomes critical. A possibility for delivering such large structures to space is by shipping them in pieces and subsequently performing on-orbit assembly. These structures often have high power requirements, which are met through large solar panels. One such structure is the ISS, the largest habitable satellite produced by mankind, which is operating for over 16 years ensuring a continuous presence of mankind in space since 2000. The spacecraft consists of a main body with different modules, which are changed from time to time, assembled with four sets of large solar arrays. The arrays span 2500 m^2, which is more than half the size of a football field. They produce more than 60 % of the space station's electric power. The continuous upgrades and on-orbit assembly of the space station often results in the shift of center of mass of the configuration. This would require updates in the dynamic model of the multibody system and also modifications in the control system.

Ghosh (1997) shows how thermally induced loads generated due to variation in solar power (shadowing), can cause asymmetrical deformations of solar panel as the solar cells expand or contract. These thermal shocks or vibrations can create forces and moments leading to a change in attitude. Buckling of the solar panels due to thermal loads has also been a major threat for the spacecraft's operational stability (Elliott et al., 2012). Additionally, at an altitude of just about 400 km, the ISS experiences atmospheric drag, which can also cause vibrations in the solar panels. Moreover, the drag also slows the spacecraft down, lowering its orbit. As a result, the ISS performs multiple corrective manoeuvres in a year to maintain its altitude. The space station also performs several collision avoidance manoeuvres to avoid any damage due to space debris impact. The attitude control system mainly relies on non-propulsive actuators; four Control Moment Gyros (CMGs) with a capacity of 4760 Nm each, which control the attitude by changing the momentum of the system. Using momentum control devices facilitate changing the attitude without inducing much vibration in the system, as it provides continuous momentum exchange as opposed to the discrete pulses of propulsive units. However, it also includes thruster attitude control to desaturate the CMGs and to support them during large attitude manoeuvres (Memi and Deason-Sharp, 2006). Additionally, the ISS uses a one-, two-, or three-axis Torque Equilibrium Attitude (TEA) seeking controller to determine the smallest amount of momentum required to maintain attitude control. Lastly, vibrations in the solar panel are detected or measured using accelerometers, Lidar instruments, photogrammetry, and so on, which are then accounted for in the control system.

Being a manned space station, it requires frequent supplies for the crew and for scientific research. Hence, the spacecraft performs multiple Rendezvous and Docking (RVD) operations in a year. Additionally, it is equipped with multiple Degree of Freedom (DOF) robotic arms (Dextrous and Canadarm2), provided by the Canadian Space Agency for performing in-orbit repairs, maintenance and upgrade operations. This is another crucial flexible component to the configuration. The ISS, thus, is a good state-of-the-art for this study, not only in terms of dynamics associated with a large multibody spacecraft, but also to study the present technology in RVD operations and AOCS requirements.

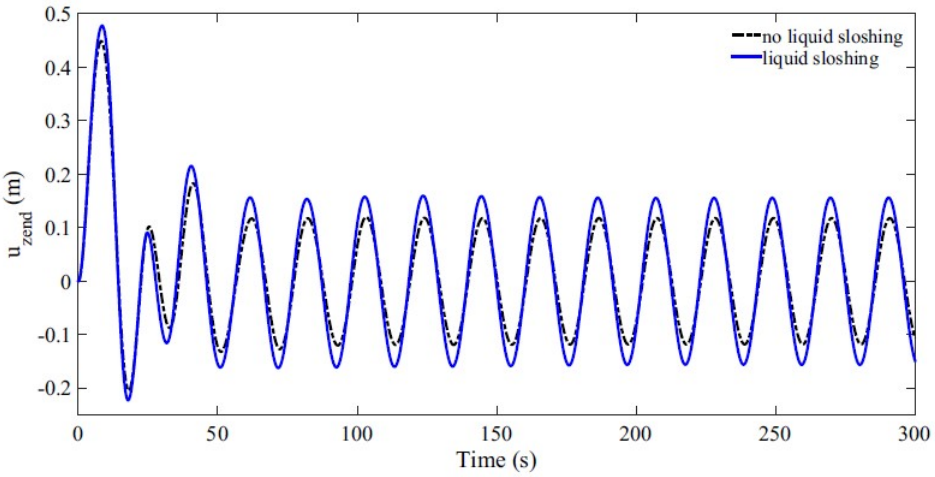

Figure 2.2: Effect of sloshing on tip displacement of a solar panel Deng and Yue (2017)

2.3. Deployment of Flexible Appendages

Large deployable appendages like communication antennae, solar panels, solar sails, radars and so on, are an integral part of modern spacecraft due to space limitation imposed by the launch vehicle. A deployable design allows folding a structure to fit the launcher fairing during launch, and deployed when the required orbit configuration is reached. The deployment of these large appendages often cause a disturbance in the spacecraft attitude. A number of factors, like the body's inertia, present angular rates, structural frequency, fuel sloshing and environmental perturbations, can affect the extent of disturbance in the attitude (Meguro et al., 2006). During this phase, attitude control becomes crucial, because the disturbances can become so large that the satellite can lose its prescribed attitude and even drift out of control. Therefore, extensive testing is performed before the launch to predict these perturbations and plan corrective actions during the deployment.

2.4. Effect of Fuel Sloshing

Vibrations in a spacecraft are not only introduced from flexible appendages, but also, from its own internal dynamics. The rigid hub of a spacecraft is not entirely rigid, because it holds the propellant tanks. Any large manoeuvres or disturbances associated with operations, like docking, spinning, and so on, can introduce large amplitude liquid slosh (and subsequently vibrations) in the system. In the presence of other flexible appendages in the system, the dynamics becomes even more complex with the flexible appendage and liquid slosh coupling with each other. This creates the possibility of slosh dynamics further amplifying the oscillations of the appendages (Deng and Yue, 2017). Figure 2.2 shows the effect of sloshing on the vibration of a solar panel, causing increased amplitude of vibration as compared to the one without sloshing. For spinning spacecraft, fuel sloshing often becomes a source of energy dissipation, causing a nutation about the axis of rotation. The "nutation angle" is defined as the angular displacement between the principal axis of rotation of the spacecraft and its angular momentum vector and is a measurement of the magnitude of the nutation (Schlee et al., 2005). A more vigorous sloshing would lead to more energy loss, thereby causing a larger nutation. In the past, missions have been lost, because of excessive and unanticipated nutation growth, which completely destabilised the system (Explorer I, 1958 and ATS-5, 1969). However, nutation can also be caused by energy dissipation through flexible appendages. From the study of flexible launchers, the slosh dynamics can induce an opposite control effect on the response of the system (Mooij and Gransden, 2019). When a large mass is involved, fluid motion may also lead to a shift in centre of mass of the satellite, which may introduce offsets in the applied control moments.

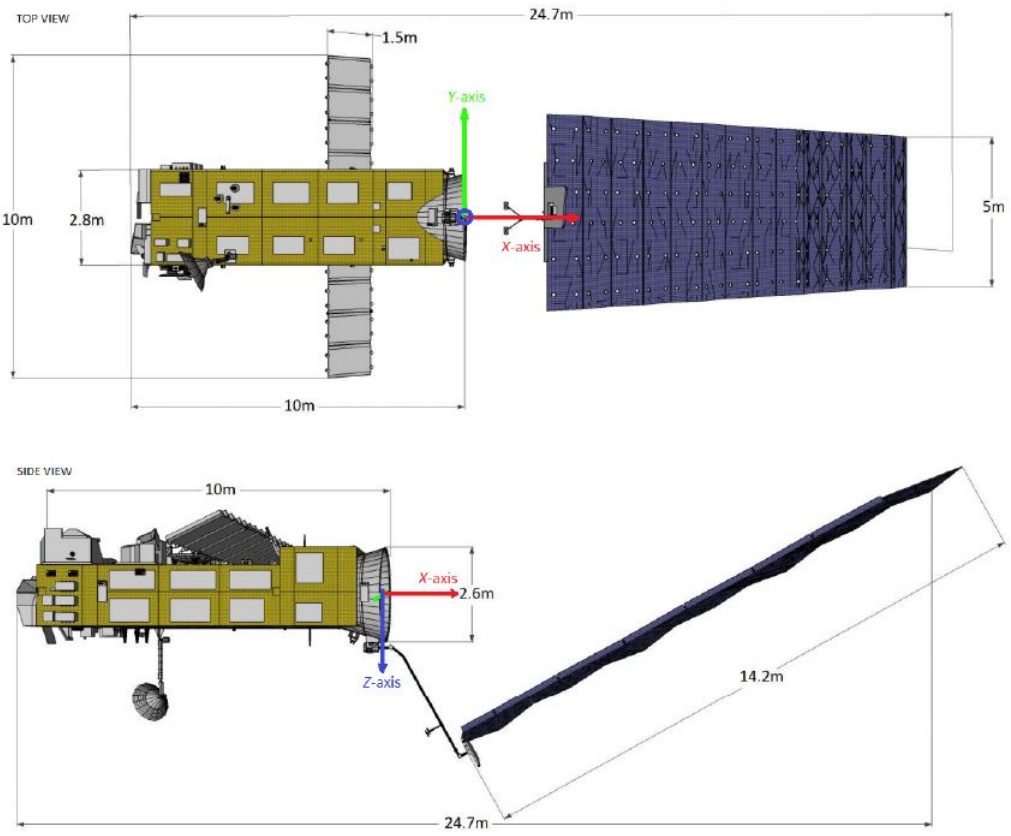

Figure 2.3: top and side view of Envisat in a body fixed frame given by ESA (2012)

Clearly, modelling of slosh dynamics is critical to increasing the safety and reliability of an attitude control system, but it is deemed beyond the scope of this study.

2.5. Active Debris Removal

As discussed in the motivation of this research, there is a need for active debris removal to ensure a sustainable future space environment. Removal of large debris with flexible appendages can prove to be very challenging and would require a robust attitude control system. The ADR technique chosen for this research involves a chaser satellite capturing its target by performing RVD operations and then de-orbiting it. Apart from flexible appendages on the target, flexible appendages on chaser satellite are also prone to vibration. Hence, its effects on the attitude of the system is inevitable. Moreover, during the detumbling and deorbiting manoeuvres, the vibrations may increase and cause instability. Therefore, modelling the flexibility becomes crucial.

2.6. Reference case - Envisat

Envisat, launched on 1 March, 2002 is the largest civilian Earth Observation satellite owned by ESA, which lost contact on April, 2012, after 10 years of successful operation. The debris now poses the highest collision risk of all ESA owned satellites in the densely populated altitude of 600-800 km near polar orbit. A collision at this altitude might lead to a cascade of collisions making it ill-suited for any operations in future. If allowed to decay naturally, the re-entry will be uncontrolled and the consequences may be potentially catastrophic due to its large mass (about 8 tonnes). The large mass, large size, complex capture access due to uncontrollable tumbling and large flexible appendages

Table 2.1: List of Envisat mass properties (Virgili, 2014)

	Value
Mass[kg]	7828
CoG [m]	X_G −3.905 Y_G −0.009 Z_G +0.003
Inertia Matrix [kg m^2]	$\begin{bmatrix} 16969 & 0 & 0 \\ 0 & 124700 & 0 \\ 0 & 0 & 129007 \end{bmatrix}$

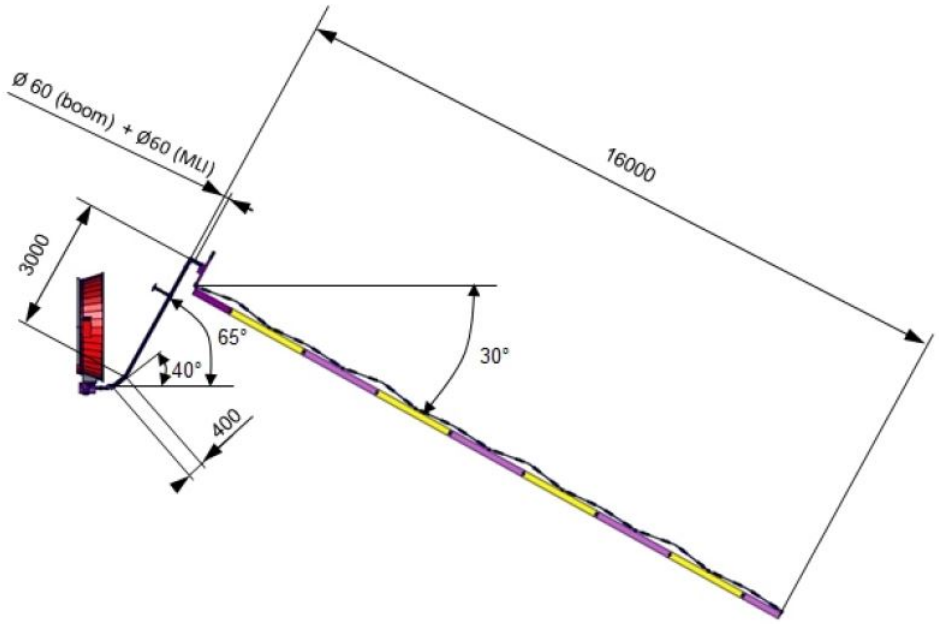

Figure 2.4: Orientation of solar array (Corso et al., 2016)

make it an ideal case study for this research.

2.6.1. Target Analysis

The initial launch mass of Envisat was 8138 kg including 319 kg of hydrazine. According to Virgili (2014), the current mass of Envisat is 7828 kg, that means it is assumed that almost all propellant is consumed. The spacecraft body consists of three major flexible appendages: the large solar array (14.2 m), the SAR antenna (top) and a Ka-dish band (bottom), as seen in Figure 2.3. To reduce the scope of the work, in this research only the flexibility due to the presence of the solar panel will be considered. The risk of fragmentation before and during the de-orbit mission was analysed to be very low by ESA (2012). It was also noted that the orbit altitude has reduced to 768 km (in 2010) compared to the launch orbit of 790 km (in 2002). However, the deterioration is very slow and for the comparatively short period for the RVD of the target and chaser, the orbit can be assumed to be constant. Further, considering a total mass of 7828 kg and the solar panel of mass, 338 kg, the Centre of Mass (CoM) and its moment of inertia about the principle axes (Virgili, 2014) is given in Table 2.1

Table 2.2: Attitude cases

Attitude Case	Angular rate about X-axis [°/s]	Angular rate about Y-axis [°/s]	Angular rate about Z-axis [°/s]
1	3.5	3.5	3.5
2	1.5	1.5	1.5
3	0	0	3.5

Solar Array

As documented by Corso et al. (2016), the size of the deployed solar panel is 16 m×4.972 m and its mass is 338 kg. The solar panel is connected to the body of the Envisat by a boom, which is capable of rotating using the Solar Array Drive Mechanism. However, the boom movement is locked by a Primary Deployment Mechanism (PDM), which consists of a self-locking gear. It is assumed for this research that the PDM is functioning and there is no boom rotation. From ground observations, it was found that the solar array has failed to achieve the desired safe mode position. Further, as shown in Corso et al. (2016), the boom is 3 m long, and forms an angle of 65° with the spacecraft body length. Further, the solar panel is locked at an angle of 30° with the spacecraft body length as shown in Figure 2.4. The figure shows the orientation of the solar panel boom and array with respect to the launcher adapter ring. However, this angled configuration is not typical of satellites with large appendages. Therefore, to get a more general overview, it will be assumed that the solar panel is attached directly to the satellite like a fixed link, and is aligned with the CoM.

Attitude model

Since the loss of connection in 2012, many ground based observations were made to determine the current attitude state of Envisat. The measurements were made by ground based Satellite Laser Ranging (SLR), Inverse Synthetic Aperture Radar (ISAR) and optical telescopes, which determined attitude from laser pulses reflected by the spacecraft. The results from 2013 indicate that the spin axis of Envisat makes an angle of 61.68° with the nadir vector and 90.69° with the along-track vector. Further, the spacecraft is rotating in the counter-clockwise direction with a period of 134.74 s in the inertial frame and slowing down by 36.7 ms/day as reported by Kucharski et al. (2014). The rotation rate about Z-axis (radial direction) is 3.5°/s with a worst case scenario of 5°/s (Virgili, 2014). It is also tumbling about other axes but the rotation rates are relatively smaller. The rates computed using simulation were 20 times slower than that the measured values, implying possible micro-meteorite/ debris impact and/or energy release. However, to understand the system dynamics better, three attitude cases will be simulated as shown in Table 2.2.

Case 1 is taken as the worst case scenario of Envisat tumbling about all axes with the spin rate of 3.5°/s. However, this overestimated scenario can prove to be very computationally expensive and difficult to work with. Therefore, in Case 2, Envisat is assumed to be tumbling about all axes with the spin rate of 1.5°/s. Lastly, Case 3 is closer to the observed scenario, wherein it is only tumbling about the Z-axis.

2.6.2. Chaser Model

According to ESA (2012), the launch mass for the e.deorbit chaser spacecraft is 1628 kg, with 762 kg of dry mass and 826 kg of consumables. As computed by Habets (2015), the final mass on achieving orbit is around 1480 kg. The shape of the chaser is assumed to be a rectangular box of dimensions 1.2×1.2×3 m. It also has a solar panel of dimensions 0.05×2.9×1.1 m of mass 25 kg. The CoM is assumed to be the geometric centre of chaser's box shaped body. The mass and inertia properties can be tabulated in Table 2.3. The chaser design aims to achieve a rigid link connection with the target. It consists of tentacles which are clamped onto the target body. An additional robotic arm can be included for redundancy and reduce the stringent requirements of a Guidance, Navigation

Table 2.3: List of Chaser mass properties (Virgili, 2014)

Property	Value
Mass[kg]	1480
CoG [m]	X_G 0.6 Y_G 0.6 Z_G 1.5
Inertia Matrix [kgm^2]	$\begin{bmatrix} 1521 & 0 & 0 \\ 0 & 1322 & 0 \\ 0 & 0 & 560 \end{bmatrix}$

Table 2.4: Chaser sensor and actuator characteristics (ESA, 2012)

AOCS/GNC	Sensors	3 x Star tracker
		2 x Sun sensor
		2 x IMU
		2 x GPS receiver
		2 x LiQuaRD LiDAR
		2 x Far field camera
		2 x Near field camera
	Actuators	4 x Reaction wheels
	RCS	24 x 22 N thrusters (12 redundant)
Capture technique	Clamping (optional Robotic arm)	

and Control (GNC) system. Instead of a robotic arm, a Lidar can be included for improvement of the AOCS. This improves the tracking capabilities of the spacecraft, thereby reducing the chances of an attitude mismatch, and eliminating the need for a robotic arm. As proposed by the Concurrent Design Facility study team in 2012, the chaser characteristics are tabulated in Table 2.4

Additionally, the chaser will have a bi-propellant system with four engines of 425 N (two active and two redundant). Also, the 24 thrusters (12 active and 12 redundant) will be used for RVD operations, as well as attitude control. The connection should be such that the CoM of the two bodies are aligned. A maximum of 6 cm (both lateral and longitudinal) misalignment can be compensated by the thrusters.

2.6.3. Connection Model

As stated in the introduction, ESA (2012) proposed three basic models for the capture of the target using a chaser spacecraft. All three models achieve connection with the target in different ways: through tentacles, through a robotic arm, or a combination of both. The connection between the target and the chaser plays a crucial role in the attitude of the system. If the connection is too flexible, the two bodies might have different attitudes even though they are connected. On the other hand, if the connection is sufficiently rigid, the connected system acts like one stack and the system can maintain the same attitude. Since all the three models are structurally very different, and the focus is to model the structural dynamics in the synchronisation and connected phase, the connection will not be modelled in this research. It will be assumed that in the connected phase, the

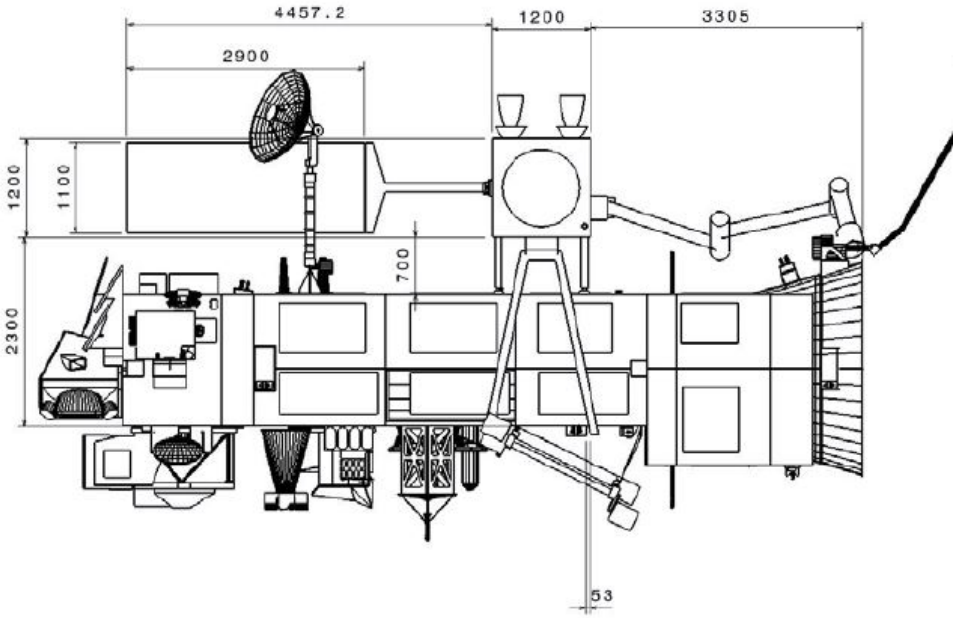

Figure 2.5: Stacked configuration of Envisat (bottom) and Chaser (top) (Credits:ESA)

Table 2.5: List of Stack Parameters (Habets, 2015)

Property	Value
Mass[kg]	9308
CoG [m]	X_G −0.9433 Y_G 0 Z_G −0.0076
Inertia Matrix [kgm^2]	$\begin{bmatrix} 130521 & 0 & 0 \\ 0 & 27282 & 0 \\ 0 & 0 & 134251 \end{bmatrix}$

connection between Envisat and chaser is rigid. With this conjecture, the stacked properties can be defined.

2.6.4. Stacked Configuration

The stacked configuration consists of the Envisat and chaser in docked configuration as shown in Figure 2.5. The geometry of both flexible and rigid elements in this configuration is asymmetric. The total mass of the connected system is given by sum of mass of the two systems involved. The mass, inertia and CoM properties of the stack as computed by Habets (2015), is summarised in Table 2.5. Note that only the inertia about principal axes is considered. The configuration is assumed to be tumbling with the same constant angular rate as that of Envisat. But due to the complexity in dynamics of the connection model between the Envisat and chaser, the configuration can be assumed to be one rigid hub with one large panel (from Envisat) and a smaller panel (from chaser). The asymmetric flexible configuration makes the dynamics of the tumbling stacked system interesting.

Table 2.6: Mission Requirements

Req. ID	Statement
R-MIS-010	The target object shall be assumed uncooperative. Note: no inter-satellite or target-ground communications, no hardware support from the target during rendezvous and docking can be expected.
R-MIS-020	A target angular velocity of 3.5°/s rotating around no single fixed axis shall be considered as a worst case scenario.
R-MIS-030	While matching the target's attitude in the synchronisation phase, the chaser shall be already at the vicinity of the target.
R-MIS-040	During the mission phases, the orbital position shall be assumed to be constant.
R-MIS-050	The effect of environmental perturbations shall be neglected.

2.7. Mission Requirements

Since, this research focuses on mainly controlling the rotational state of the chaser during synchronisation, and the stack during detumbling, in the presence of external perturbations due to flexibility, only mission requirements relevant to the study will be addressed. Some official mission requirements are chosen from ESTEC (2014) and listed in Table 2.6. More requirements, derived from the observations made on mission heritage are also listed in the table.

2.8. System requirements

The system requirements will include the design requirements for the mission. Only the system and subsystem requirements relevant to the research will be discussed here.

2.8.1. Mechanical System

In Table 2.7, the requirements of mechanical system in terms of design and function will be defined as per the system requirements of the mission.

2.8.2. Control System

The requirements of the control system, which includes the sensors, actuators and controllers will be discussed in Table 2.8. The mission requires a robust control system to perform the whole operation autonomously, even in the presence of anomalies.

Table 2.7: Mechanical System

Req. ID	Statement
R-SYS-010	There shall be no flexibility introduced in the stacked system due to the tentacles or robotic arm used for the capture.
R-SYS-020	There shall be 3% structural damping in the flexible appendages.
R-SYS-030	The chaser in the sychronisation phase shall represent a rigid hub with one flexible appendage.
R-SYS-040	The system in the stacked configuration shall represent a rigid hub with two flexible appendages.
R-SYS-050	The mechanical links (tentacles or robotic arm) used to maintain connection between the chaser and target should be strong enough to withstand any torques due to flexibility.
R-SYS-060	A rigid connection shall be assumed between the chaser and Envisat during the connected phase.

Table 2.8: Control system

Req. ID	Statement
R-ACS-010	The chaser spacecraft shall be 3-axis controlled to comply with the requirements for the rendezvous manoeuvres, forced translation, capture manoeuvres from the beginning of the rendezvous phase till the controlled re-entry of the stack.
R-ACS-020	Sensors (like accelerometers) shall be present to record the effect of flexibility on the attitude
R-ACS-030	The chaser spacecraft shall provide the only means of control for the stacked configuration during the detumbling manoeuvre.
R-ACS-040	The stacked configuration shall achieve a set point attitude in a stabilised state to perform deorbiting manoeuvre.
R-ACS-050	The control limit should be chosen such that the induced motion does not result in large vibrations in the panel.
R-ACS-060	Both actuators and sensors shall be assumed to be ideal.

3

Flight Dynamics

To control the attitude of a spacecraft, the first step is to define the attitude with respect to a reference. Depending on the application, the reference can be chosen on the body itself (*e.g.*, to define the rigid body motion of the satellite) or another location away from the body (*e.g.*, to define the motion of a robotic arm relative to the body). For the design of a robust control system, the complete kinematics and dynamics of the system should be modelled correctly. To achieve this, it is important to understand the attitude parametrisation, reference frames and their transformation from one to the other.

To evaluate the controllability characteristics of a Flexible Multibody System (FMS) using the guidance and control based on a rigid system, two kinds of reference frames will be established for each model (rigid and flexible). However, only the aspects associated with the rigid body modelling will be discussed in this chapter. The FMD will be defined in Chapter 4. First, the reference frames relevant to the rigid body formulation will be introduced in Section 3.1. Second, the different types of attitude representation for defining the orientation of the spacecraft itself will be discussed in Section 3.2. Then, a trade-off will be performed and the most fitting attitude representations, which in combination with reference frames form the co-ordinate systems of the Envisat-Chaser model in 3D space, will be selected in the same section. Sometimes the coordinates need to be transformed from one representation to another for interpolation of dynamics. This is achieved using transformation matrices introduced in Section 3.3. Then to define the evolution of the rigid body attitude with time, the kinematic and dynamic equations of motion will be set up in Section 3.4. Since the flexible vibrations are unwanted and can be treated as perturbations to the rigid body system, the guidance and control of the satellite can be modelled based on the rigid body EOM defined in this chapter. This is, because synchronisation, detumbling and all other operations performed on the satellite, are to control the rigid body rotational motion of the satellite. Therefore, in Section 3.5, the guidance logic for different phases of the mission will be explained. To understand the effect of flexible dynamics on controllability, one linear and one nonlinear controller will be chosen. The theory of these controllers will be provided in Section 3.6

3.1. Reference Frames

Reference frames are required to define the attitude of the spacecraft in terms of angular position, velocity and acceleration. Sometimes a combination of reference frames is needed to be able to define the complete dynamics of the system. Based on the application alone, a number of reference frames can be derived. One, a reference frame to define the motion of the body. Two, a reference frame attached to the spacecraft body to define the orientation of the spacecraft in its orbit. And

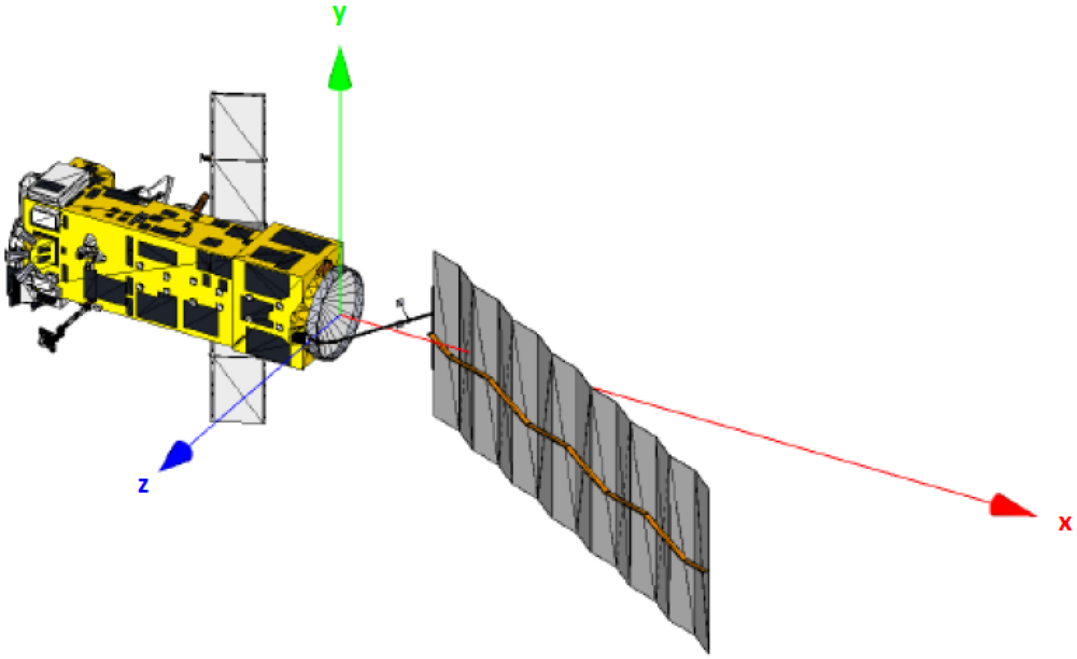

Figure 3.1: Envisat Geometric Frame (Virgili et al., 2014)

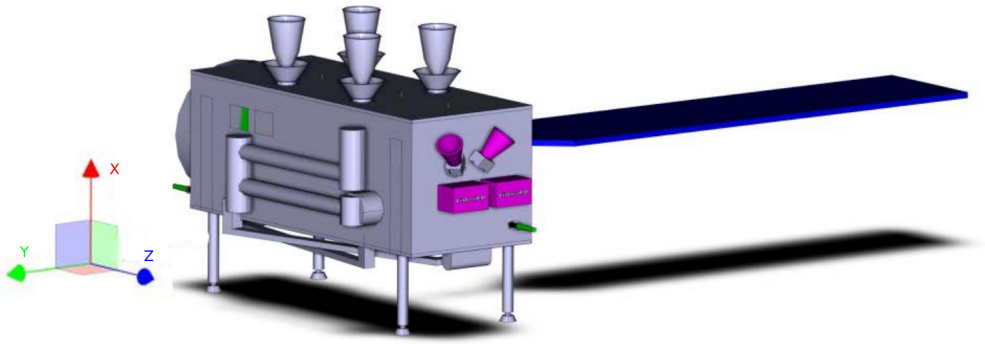

Figure 3.2: Chaser Geometric Frame (ESA, 2012)

three, multiple localised fixed frames on the spacecraft body to define the position of appendages and actuators with respect to its CoM.

3.1.1. Inertial Frame

An inertial frame ($\mathcal{F}_I$) is used to define the attitude of an orbiting body, which is continuously changing with time. An inertial frame can be placed at any point with respect to which the motion of the object remains constant, unless acted upon by an external force. Newton's laws of motion are only valid in the inertial frame, unless apparent forces are introduced. Even though the translational motion will not be simulated in this thesis, the rigid body Euler EOM are derived from Newton's laws. Therefore, an inertial frame is required to obtain even the simplest form of these EOM. Typically for defining the position of the spacecraft in its orbit, Earth is chosen as the reference frame. However, for the current application, only the rotational state of the spacecraft needs to be defined so the inertial frame can be chosen arbitrarily.

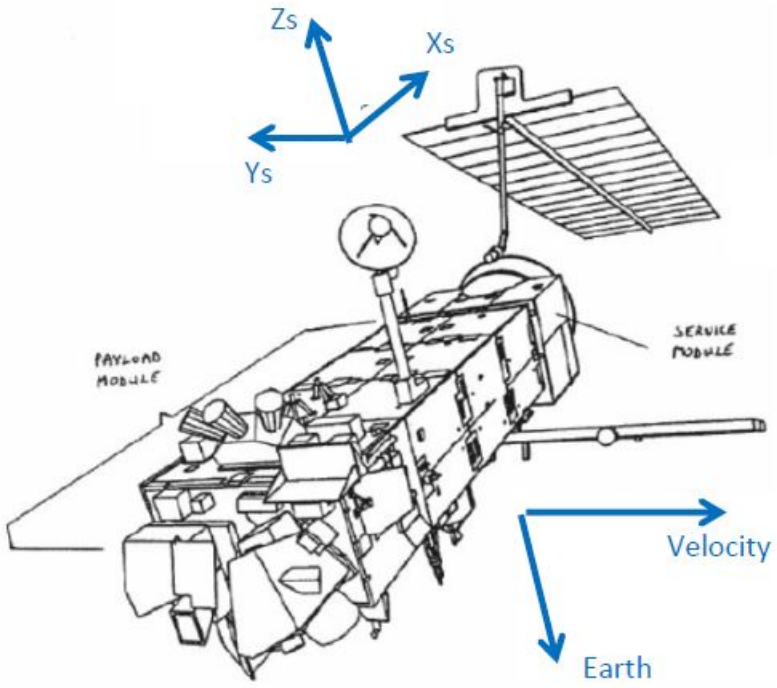

Figure 3.3: Envisat Body Frame (Virgili, 2014)

3.1.2. Geometric Frame

The geometric reference frame is fixed the spacecraft, and can be placed anywhere on the body. It defines the position of any point on the vehicle with respect to its origin. The frame is also useful for efficient formulation of multibody dynamics, which for this research is imperative. It is used to define the contribution of each element to the rotational inertia of the system using Steiner's parallel axis theorem.

For the Envisat model, the geometric frame is shown in Figure 3.1. While the origin can be placed anywhere on the system, the X-axis lies along the length of the Envisat body, the Y-axis is along the SAR antenna, and the Z-axis is perpendicular to the plane completing the right handed system. For the chaser model, the geometric frame is adapted from ESA (2012). The X-axis is along the direction of the thrusters, the Y-axis opposite to the solar panel, and the Z-axis lies along the chaser body length, as shown in Figure 3.2.

3.1.3. Body Fixed Frame

The body fixed frame ($\mathcal{F}_B$) is a geometric frame with its origin at the spacecraft's CoM. It is used to define the position and orientation of the spacecraft with respect to the inertial frame. The rotation of the spacecraft about the body fixed X, Y and Z axis are called roll, pitch and yaw, respectively. Any change in the rotational dynamics of the spacecraft is recorded as the relative change in body fixed frame with respect to the inertial frame. Therefore, the body fixed frame is needed to represent the kinematics and dynamics of the spacecraft.

In case of Envisat, the orientation of the body frame is the same as the geometric frame, but with the origin at the CoM, as shown in Figure 3.3. Similarly, the chaser's body frame is the same as the geometric frame, but located at its own CoM.

Table 3.1: Attitude representation characteristics (Singla et al., 2005)

Parameterisation	**Dimensions**	**Kinematic Equations**	**Singularities**	**Constraints**
DCM (C_{ij})	9	$\dot{\boldsymbol{C}} =$ [Linear functions of ω] $\boldsymbol{C}$	No	$\boldsymbol{C^T C} = \boldsymbol{I}$
Euler Angles (θ_i)	3	$\dot{\boldsymbol{\theta}} =$ [Trigonometric functions of θ_i] $\boldsymbol{\omega}$	$\theta = \pm\frac{\pi}{2}$ or $\theta = 0, \pi$	No
Quaternions (q_i)	4	$\dot{\boldsymbol{q}} =$ [Linear functions of q_i] $\boldsymbol{\omega}$	No	$\boldsymbol{q^T q} = 1$
RP (r_i)	3	$\dot{\boldsymbol{r}} =$ [Non – linear functions of r_i] $\boldsymbol{\omega}$	$\phi = \pm\pi$	No
MRP (σ_i)	3	$\dot{\boldsymbol{\sigma}} =$ [Non – linear functions of σ_i] $\boldsymbol{\omega}$	$\phi = \pm 2\pi$	No

3.2. Attitude State Representation

The attitude can be represented in different formulations based on the application (*e.g.*, simulation, interpolation or visualisation). Based on the requirements for the current system and characteristics of different parametrisations, a fitting model will be selected. Further, it is imperative to understand the orientation of the frames with respect to each other to visualise the dynamics, since it is often defined using a computationally efficient, but less visual representation. The common representations are the Direction Cosine Matrix (DCM), Euler angles, quaternions, Rodrigues Parameters (RP) and Modified Rodrigues Parameters (MRP). An analysis of their characteristics and trade-off will help the selection of the most fitting attitude representations for the research.

3.2.1. Trade-Off and Selection

A trade-off can be done based on the characteristics of each attitude parametrisation as tabulated in Table 3.1. At any time and for the application in hand, the use of the representation should be free of singularities. In case of uncontrolled debris like Envisat, encountering a singularity is a potential danger, because of the chaotic attitude tumbling. For simulation of dynamics and for control applications, the representation should minimise the computation time and be numerically stable for the chosen integration method. It should allow for the largest possible stepsize driven by local truncation errors, and user specified tolerances. Lastly, to analyse the attitude evolution with time, the representation must be easy to visualise. Thus, based on this analysis the advantages and disadvantages are tabulated in Table 3.2

Based on these criteria, DCM can be eliminated as an option for formulating the EOM, even though it has no singularities. This is because the attitude is represented using nine terms, which becomes computationally heavy. Additionally, it requires six constraint equations in addition to the three independent time propagation equations to define the attitude. DCM is also known to be computationally unstable while integrating non-linear dynamics and needs frequent re-normalisation and re-orthogonalisation to prevent poor results. However, the DCM itself is an important means for transformation between the inertial and body frame, and will be thoroughly used in this research.

Euler angles have comparatively lower computational effort compared to DCM. They are very easy to transform from one reference frame to another. However, they are not always the best suited model for computer simulation, because of the presence of a singularity. Euler's rotation theorem states that any attitude definition based on three independent parameters will contain a singularity

Table 3.2: Analysis of parameterisation (Singla et al., 2005)

Parameterisation	**Advantages**	**Disadvantages**
DCM (C_{ij})	• No singularities, because the matrix is invertible. • Orientations define unique direction cosine matrices.	• Nine elements make parametrisation computationally expensive. • Requires six constraint equations in addition to the three independent ones for time propagation.
Euler Angles (θ_i)	• Minimal set of parameters, computationally faster. • Easy to interpret and widely used to visualise attitude. • Reference-frame transformations are very easy.	• Contains singularity, which could cause problems for the attitude parametrisation of tumbling satellites. • To avoid singularity, book-keeping is required, so that the angles can be switched to an alternate set representing the same attitude.
Quaternions (q_i)	• Low computational effort. • Kinematic equations are linear. • No singularity.	• Frame transformations are relatively more complex compared to Euler. • Constraint $\boldsymbol{q}^T\boldsymbol{q} = \boldsymbol{I}$ (orthogonality) must be maintained in simulations.
RP (r_i)	• Minimal parameterisation.	• Singularity present • Non-linear kinematic differential equations
MRP (σ_i)	• Minimal parametrisation	• Non-linear kinematic differential equations. • Singularity present, but delayed and can be avoided using shadow parameter technique.

in one of them. This means that this particular attitude cannot be simulated. As long as the attitude of the satellite will not get close to that attitude, the chosen set of Euler angles can be safely used, otherwise one could switch to an alternative set, which has the singularity in another parameter. However, this book-keeping may prove cumbersome when also a commanded attitude is involved. Further, for a tumbling target, which can easily move towards the singularity, attitude representation through Euler angles is not preferred.

Quaternions seem to be a very attractive choice for this research with their low computational effort and absence of singularities. With respect to Euler angles, the quaternions contain a redundant dimension, which eliminates the singularity. Moreover, unlike Euler angles with trigonometric expressions, in quaternions the equations of motion are linear, making it computationally more efficient. However, the disadvantages of quaternions are that they cannot be used for visualisation of the attitude and also have a normalisation constraint. The normalisation requires special attention during integration and controller design. Lastly, since they can only define an attitude ranging between $\pm 180°$, it may complicate the application of continuous attitude tracking.

Lastly, RP and MRP, which are again three parameter representations, are less computation-

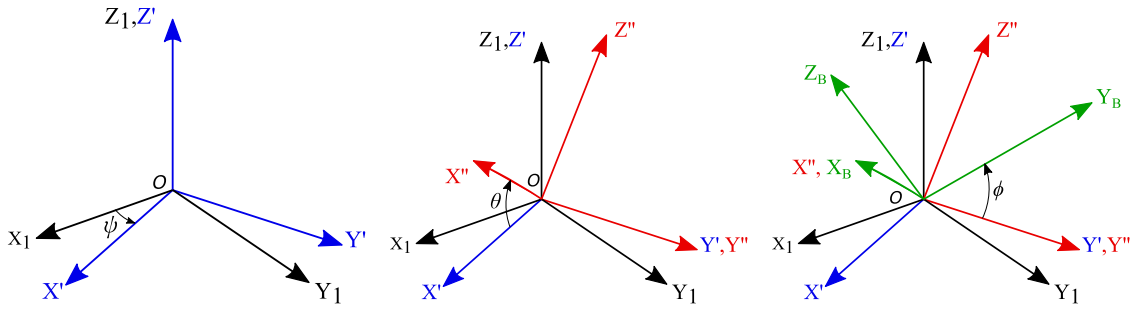

(a) Rotation about Z-axis (b) Rotation about Y-axis (c) Rotation about X-axis

Figure 3.4: Euler angles - rotation sequence ZYX

ally expensive, but do contain singularities. Nonetheless, the singularities in RP cannot eliminated, which is not sufficient to model the dynamics of a tumbling body. Lastly, the singularities in MRP can be avoided using shadow sets where the sign of quaternion vectors are flipped without affecting the rotation. However, implementing the shadow parameter technique requires book-keeping, which is not very favourable for controller design.

Therefore, based on the analysis, quaternions can be selected as the most fitting model for this study. For analytical purposes (like visualisation and interpretation of attitude) and transformation of reference frames, Euler angles are also discussed. In the coming sections, quaternions and Euler angles are developed in more detail. The transformation between the two attitude representations will also be discussed, so that the attitude obtained using quaternions can be anticipated using Euler angles.

3.2.2. Euler Angles

Euler angles are a commonly used minimal dimension representation for attitude in the aerospace industry. The orientation of the body is expressed as rotations about a single axis of a body-fixed frame. A total of 12 unique Euler-angle combinations (six symmetric and six asymmetric) are possible, which are commonly applied in 3-2-1 (ZYX) sequence. Figure 3.4 shows the rotation of inertial frame ($\mathcal{F}_I$) to body-fixed frame ($\mathcal{F}_B$). In Figure 3.4(a), it can be seen that the first rotation is about the Z_I-axis by an angle ψ (yaw), resulting in the new frame I'. Then in Figure 3.4(b), the rotation happens about Y' by an angle θ (pitch), giving reference frame I". Lastly, Figure 3.4(c) shows the rotation about the X''-axis over an angle ϕ (roll). These rotations can be numerically represented as:

$$\begin{pmatrix} X' \\ Y' \\ Z' \end{pmatrix} = \boldsymbol{C_3}(\psi) \begin{pmatrix} X_I \\ Y_I \\ Z_I \end{pmatrix} = \begin{bmatrix} \cos\psi & \sin\psi & 0 \\ -\sin\psi & \cos\psi & 0 \\ 0 & 0 & 1 \end{bmatrix} \begin{pmatrix} X_I \\ Y_I \\ Z_I \end{pmatrix} \tag{3.1}$$

$$\begin{pmatrix} X'' \\ Y'' \\ Z'' \end{pmatrix} = \boldsymbol{C_2}(\theta) \begin{pmatrix} X' \\ Y' \\ Z' \end{pmatrix} = \begin{bmatrix} \cos\theta & 0 & -\sin\theta \\ 0 & 1 & 0 \\ \sin\theta & 0 & \cos\theta \end{bmatrix} \begin{pmatrix} X' \\ Y' \\ Z' \end{pmatrix} \tag{3.2}$$

$$\begin{pmatrix} X_B \\ Y_B \\ Z_B \end{pmatrix} = \boldsymbol{C_1}(\phi) \begin{pmatrix} X'' \\ Y'' \\ Z'' \end{pmatrix} = \begin{bmatrix} 1 & 0 & 0 \\ 0 & \cos\phi & \sin\phi \\ 0 & -\sin\phi & \cos\phi \end{bmatrix} \begin{pmatrix} X'' \\ Y'' \\ Z'' \end{pmatrix} \tag{3.3}$$

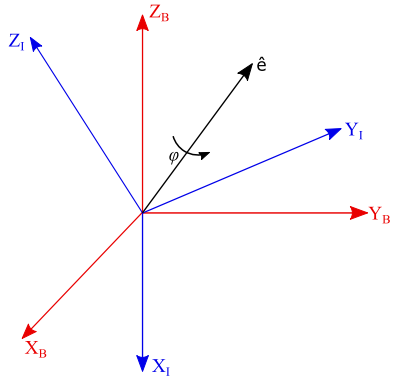

Figure 3.5: Rotation about Euler eigenaxis

Equations (3.1) through (3.3) can be combined to get:

$$\begin{pmatrix} X_B \\ Y_B \\ Z_B \end{pmatrix} = \boldsymbol{C_1}(\phi)\boldsymbol{C_2}(\theta)\boldsymbol{C_3}(\psi)\begin{pmatrix} X_I \\ Y_I \\ Z_I \end{pmatrix} = \boldsymbol{C_I^B}\begin{pmatrix} X_I \\ Y_I \\ Z_I \end{pmatrix} \tag{3.4}$$

where $\boldsymbol{C_I^B}$ is an orthonormal matrix such that $(\boldsymbol{C_I^B})^{-1} = (\boldsymbol{C_I^B})^{T}$. It is called a rotation matrix to obtain body frame B from inertial frame I, and can be expanded as:

$$\boldsymbol{C_I^B} = \boldsymbol{C_1}(\phi)\boldsymbol{C_2}(\theta)\boldsymbol{C_3}(\psi) = \begin{bmatrix} c\theta c\psi & c\theta s\psi & -s\theta \\ s\phi s\theta c\psi - c\phi s\psi & s\phi s\theta c\psi + c\phi c\psi & s\phi c\theta \\ c\phi s\theta c\psi + s\phi s\psi & c\phi s\theta s\psi - s\phi c\psi & c\phi c\theta \end{bmatrix} \tag{3.5}$$

where c ≡ cos and s ≡ sin. Therefore, Euler angles are used in this research, for transformation of reference frames and for visualisation of attitude.

3.2.3. Quaternions

Another method used for representing the orientation can be achieved by introducing a unit vector $\hat{\boldsymbol{e}}$ along the Euler's eigenaxis. The orientation of both $\mathscr{F}_B$ and $\mathscr{F}_I$ can be defined with respect to this axis, as shown in Figure 3.5. Thus, the unit vector can be written as (Wie, 1998):

$$\hat{\boldsymbol{e}} = e_1\hat{\boldsymbol{x}}_{\boldsymbol{I}} + e_2\hat{\boldsymbol{y}}_{\boldsymbol{I}} + e_3\hat{\boldsymbol{z}}_{\boldsymbol{I}} \tag{3.6}$$

or

$$\hat{\boldsymbol{e}} = e_1\hat{\boldsymbol{x}}_{\boldsymbol{B}} + e_2\hat{\boldsymbol{y}}_{\boldsymbol{B}} + e_3\hat{\boldsymbol{z}}_{\boldsymbol{B}} \tag{3.7}$$

where e_1,e_2 and e_3 represent the direction cosines of the Euler axis relative to both $\mathscr{F}_B$ and $\mathscr{F}_I$, and maintain a relation such that ${e_1}^2 + {e_2}^2 + {e_3}^2 = 1$. The four quaternions, also known as Euler parameters are given by:

$$q_1 = e_1 \sin(\varphi/2) \tag{3.8}$$

$$q_2 = e_2 \sin(\varphi/2) \tag{3.9}$$

$$q_3 = e_3 \sin(\varphi/2) \tag{3.10}$$

$$q_4 = \cos(\varphi/2) \tag{3.11}$$

where φ denotes the rotation about the Euler axis. For simplicity, in this section the Euler vector will be denoted by $\boldsymbol{e}$ and vector $\boldsymbol{q} = (q_1, q_2, q_3)$ such that,

$$\boldsymbol{q} = \boldsymbol{e}\sin(\varphi/2) \tag{3.12}$$

It is important to note that these quaternions are not independent of each other because ${e_1}^2 + {e_2}^2 + {e_3}^2 = 1$. This implies,

$$\boldsymbol{q}^{\boldsymbol{T}}\boldsymbol{q} + q_4^2 = q_1^2 + q_2^2 + q_3^2 + q_4^2 = 1 \tag{3.13}$$

Also,

$$\boldsymbol{q} \otimes \boldsymbol{q}^{-\mathbf{1}} = \boldsymbol{q}^{-\mathbf{1}} \otimes \boldsymbol{q} = \begin{bmatrix} 0 & 0 & 0 & 1 \end{bmatrix}^T \tag{3.14}$$

where $\otimes$ indicates the quaternion multiplication. The multiplication between two quaternion vectors $\boldsymbol{p} = (p_1, p_2, p_3, p_4)$ and $\boldsymbol{q} = (q_1, q_2, q_3, q_4)$ is given by:

$$\begin{pmatrix} r_1 \\ r_2 \\ r_3 \\ r_4 \end{pmatrix} = \begin{bmatrix} p_4 & p_3 & -p_2 & -p_1 \\ -p_3 & p_4 & p_1 & -p_2 \\ p_2 & -p_1 & p_4 & -p_3 \\ p_1 & p_2 & p_3 & p_4 \end{bmatrix} \begin{pmatrix} q_1 \\ q_2 \\ q_3 \\ q_4 \end{pmatrix} \tag{3.15}$$

or $\boldsymbol{r} = \boldsymbol{p} \otimes \boldsymbol{q}$. Note that the quaternion multiplication is not commutative. The transformation from $\mathscr{F}_A$ to $\mathscr{F}_B$ can be done using a rotation matrix, like in the case of Euler angles. The rotation matrix can be written as (Wie, 1998):

$$\boldsymbol{C}_{\boldsymbol{A}}^{\boldsymbol{B}} = \boldsymbol{C}(\boldsymbol{q}, q_4) = \begin{bmatrix} 1-2(q_2^2+q_3^2) & 2(q_1q_2+q_3q_4) & 2(q_1q_3-q_2q_4) \\ 2(q_1q_2-q_3q_4) & 1-2(q_1^2+q_3^2) & 2(q_2q_3+q_1q_4) \\ 2(q_3q_1+q_2q_4) & 2(q_2q_3-q_1q_4) & 1-2(q_1^2+q_2^2) \end{bmatrix} \tag{3.16}$$

Due to the absence of trigonometric functions, the quaternions provide a computationally fast and robust representation without singularities. However, just like Euler angles the quaternions are not unique. The quaternion $\boldsymbol{q}$ represents the same orientation as $-\boldsymbol{q}$. Moreover, quaternions are not the best fit for visualisation purposes and are relatively harder to interpret than Euler angles. Therefore, the quaternions will only be used in the EOM to simulate the kinematics of the system.

3.3. Coordinate Transformations

This section describes the transformation between Euler angles and quaternions.

3.3.1. Euler Angles to Quaternions

This transformation is used when a commanded attitude (or setpoint attitude) given by Euler angles is to be converted to quaternions. According to Wie (1998), this transformation can be achieved by assuming each rotation axis as an Euler axis. Then, the consecutive rotations can be represented using quaternions as:

$$\boldsymbol{q} = \boldsymbol{q}''' \otimes (\boldsymbol{q}'' \otimes \boldsymbol{q}') \tag{3.17}$$

where q''', q'' and q' represent rotations ψ (yaw), θ (pitch) and ϕ (roll), respectively. The equation can be further expanded in matrix form as follows:

$$\begin{pmatrix} q_1 \\ q_2 \\ q_3 \\ q_4 \end{pmatrix} = \begin{bmatrix} q_4''' & q_3''' & -q_2''' & q_1''' \\ -q_3''' & q_4''' & q_1''' & q_2''' \\ q_2''' & -q_1''' & q_4''' & q_3''' \\ -q_1''' & -q_2''' & -q_3''' & q_4''' \end{bmatrix} \begin{bmatrix} q_4'' & q_3'' & -q_2'' & q_1'' \\ -q_3'' & q_4'' & q_1'' & q_2'' \\ q_2'' & -q_1'' & q_4'' & q_3'' \\ -q_1'' & -q_2'' & -q_3'' & q_4'' \end{bmatrix} \begin{pmatrix} q_1' \\ q_2' \\ q_3' \\ q_4' \end{pmatrix} \tag{3.18}$$

Using the definition of quaternion from Equations (3.11) and (3.12), the matrix of individual quaternions can be written as:

$$q' = \begin{pmatrix} 0 \\ 0 \\ \sin\psi/2 \\ \cos\psi/2 \end{pmatrix}, \quad q'' = \begin{pmatrix} 0 \\ \sin\theta/2 \\ 0 \\ \cos\theta/2 \end{pmatrix} \quad q'' = \begin{pmatrix} \sin\phi/2 \\ 0 \\ 0 \\ \cos\phi/2 \end{pmatrix} \tag{3.19}$$

Substituting this back into Equation (3.18), the equation can be simplified to:

$$\begin{pmatrix} q_1 \\ q_2 \\ q_3 \\ q_4 \end{pmatrix} = \begin{bmatrix} \sin\frac{\phi}{2}\cos\frac{\theta}{2}\cos\frac{\psi}{2} - \cos\frac{\phi}{2}\sin\frac{\theta}{2}\sin\frac{\psi}{2} \\ \cos\frac{\phi}{2}\sin\frac{\theta}{2}\cos\frac{\psi}{2} + \sin\frac{\phi}{2}\cos\frac{\theta}{2}\sin\frac{\psi}{2} \\ \cos\frac{\phi}{2}\cos\frac{\theta}{2}\sin\frac{\psi}{2} - \sin\frac{\phi}{2}\sin\frac{\theta}{2}\cos\frac{\psi}{2} \\ \cos\frac{\phi}{2}\cos\frac{\theta}{2}\cos\frac{\psi}{2} - \sin\frac{\phi}{2}\sin\frac{\theta}{2}\sin\frac{\psi}{2} \end{bmatrix} \tag{3.20}$$

3.3.2. Quaternions to Euler Angles

According to Shuster (1993), the quaternions can be converted into Euler angles by comparison of their DCM, which represent the same rotation sequence. Considering the 3-2-1 rotation sequence, gives:

$$\begin{pmatrix} \phi \\ \theta \\ \psi \end{pmatrix} = \begin{bmatrix} \text{atan2}(2(q_2q_3 + q_1q_4)), {q_4}^2 + {q_3}^2 - {q_1}^2 - {q_2}^2 \\ \text{asin}(2(q_2q_4 + q_1q_3)) \\ \text{atan2}(2(q_1q_2 + q_3q_4)), {q_4}^2 + {q_1}^2 - {q_2}^2 - {q_3}^2 \end{bmatrix} \tag{3.21}$$

Here, atan2 is used to determine the right quadrants of the angles ϕ and ψ. Furthermore, using the constraints on Euler angles to avoid singularity given by,

$$-\pi \leq \phi < \pi, \quad -\pi/2 \leq \theta \leq \pi/2, \quad -\pi \leq \psi < \pi \tag{3.22}$$

and the property of quaternions as stated in Equation (3.13),

$$q_1^2 + q_2^2 + q_3^2 + q_4^2 = 1 \tag{3.23}$$

$$q_2q_4 - q_1q_3 = 0.5 \tag{3.24}$$

which gives:

$$(q_1 + q_3)^2 + (q_2 - q_4)^2 = 0 \tag{3.25}$$

From this equation, it can be concluded that the equation holds when $q_1 = -q_3$ and $q_2 = q_4$. Using these conditions in Equation (3.21), it is found that ϕ and ψ are ambiguously defined at these values. That means, Euler angles for the corresponding values cannot be found due to the presence of singularity in Euler angles at these points. This transformation is used when the orientation is difficult to visualise using the quaternions. However, for computation purposes the Euler angles will not be used at all.

3.4. Kinematics and Dynamics of rotational motion

The attitude of a spacecraft can be completely defined using two sets of equations - kinematic equations and dynamic equations. They can be defined as:

- *Kinematic Equations*: Kinematics is the study of motion of a body irrespective of the forces and torques acting on it. The kinematic equation defines the time evolution of position and/or attitude. Here, it relates time derivatives of orientation angles to (angular) velocity.

- *Dynamic Equations*: Dynamics is the study of motion of a body in response to the forces and torques acting on it. In this thesis, the dynamic equations define the time evolution of angular velocity vector due to torque.

Since the kinematics and dynamics of a rigid and flexible spacecraft are quite different, it is important to understand both models for this research. This section will describe the complete EOM of a rigid body, adapted from Wie (1998).

3.4.1. Kinematic Equations

For a rigid body, the position of one point with respect to another point on the body remains constant throughout its attitude evolution. Therefore, in this section the kinematic differential equations will be developed using time-dependent relations of two reference frames. The equations will be derived in terms of quaternions.

Consider the angular velocity of $\mathcal{F}_B$ with respect to $\mathcal{F}_I$, expressed by vector $\boldsymbol{\omega}_{\boldsymbol{B}}^{\boldsymbol{B,I}}$. Further, the direction cosine matrix to transform from $\mathcal{F}_I$ to $\mathcal{F}_B$ is denoted by $\boldsymbol{C} = \boldsymbol{C}_{\boldsymbol{I}}^{\boldsymbol{B}}$. The transformation can be written as:

$$\begin{pmatrix} \boldsymbol{b_1} \\ \boldsymbol{b_2} \\ \boldsymbol{b_3} \end{pmatrix} = \boldsymbol{C} \begin{pmatrix} \boldsymbol{i_1} \\ \boldsymbol{i_2} \\ \boldsymbol{i_3} \end{pmatrix} \tag{3.26}$$

or

$$\begin{pmatrix} \boldsymbol{i_1} \\ \boldsymbol{i_2} \\ \boldsymbol{i_3} \end{pmatrix} = \boldsymbol{C}^T \begin{pmatrix} \boldsymbol{b_1} \\ \boldsymbol{b_2} \\ \boldsymbol{b_3} \end{pmatrix} \tag{3.27}$$

Taking the time derivative of this equation results in:

$$\begin{pmatrix} 0 \\ 0 \\ 0 \end{pmatrix} = \dot{\boldsymbol{C}}^T \begin{pmatrix} \boldsymbol{b_1} \\ \boldsymbol{b_2} \\ \boldsymbol{b_3} \end{pmatrix} + \boldsymbol{C}^T \begin{pmatrix} \dot{\boldsymbol{b_1}} \\ \dot{\boldsymbol{b_2}} \\ \dot{\boldsymbol{b_3}} \end{pmatrix} = \dot{\boldsymbol{C}}^T \begin{pmatrix} \boldsymbol{b_1} \\ \boldsymbol{b_2} \\ \boldsymbol{b_3} \end{pmatrix} + \boldsymbol{C}^T \begin{pmatrix} \boldsymbol{\omega} \times \boldsymbol{b_1} \\ \boldsymbol{\omega} \times \boldsymbol{b_2} \\ \boldsymbol{\omega} \times \boldsymbol{b_3} \end{pmatrix} \tag{3.28}$$

The last term is the derivative of basis vector in inertial frame with components solved along the body axis (Wie, 1998). The derivative of the DCM is defined as:

$$\dot{\boldsymbol{C}} = \begin{bmatrix} \dot{C}_{11} & \dot{C}_{12} & \dot{C}_{13} \\ \dot{C}_{21} & \dot{C}_{22} & \dot{C}_{23} \\ \dot{C}_{31} & \dot{C}_{32} & \dot{C}_{33} \end{bmatrix} \tag{3.29}$$

Therefore, the kinematic differential equations in terms of direction cosines can be written as:

$$\dot{\boldsymbol{C}} - \boldsymbol{C}^{\boldsymbol{T}} \boldsymbol{\Omega} = \boldsymbol{0}, \quad \text{or} \quad \boldsymbol{\Omega} = -\dot{\boldsymbol{C}} \boldsymbol{C}^{\boldsymbol{T}} \tag{3.30}$$

On simplification, $\boldsymbol{\Omega}$ can be written as:

$$\boldsymbol{\Omega} = \begin{bmatrix} 0 & -\omega_3 & \omega_2 \\ \omega_3 & 0 & -\omega_1 \\ -\omega_2 & \omega_1 & 0 \end{bmatrix} \tag{3.31}$$

$\boldsymbol{\Omega}$ represents a skew-symmetric matrix, typically also represented by a tilde ("~") symbol on top of the variable. Some properties of the skew-symmetric matrix are stated in Appendix A. Substituting

quaternion elements into the DCM (see Equation (3.16)) such that $\boldsymbol{q} = [q_1\ q_2\ q_3\ q_4]^T$, gives:

$$\begin{aligned}\omega_1 &= 2(\dot{q}_1 q_4 + \dot{q}_2 q_3 - \dot{q}_3 q_2 - \dot{q}_4 q_1)\\ \omega_2 &= 2(\dot{q}_2 q_4 + \dot{q}_3 q_1 - \dot{q}_1 q_3 - \dot{q}_4 q_2)\\ \omega_3 &= 2(\dot{q}_3 q_4 + \dot{q}_1 q_2 - \dot{q}_2 q_1 - \dot{q}_4 q_3)\end{aligned} \tag{3.32}$$

Differentiating the quaternion unit constraint as shown in Equation (3.13) gives:

$$0 = 2(\dot{q}_1 q_1 + \dot{q}_2 q_2 - \dot{q}_3 q_3 - \dot{q}_4 q_4) \tag{3.33}$$

Rearranging the above equations and re-writing in matrix form gives:

$$\begin{pmatrix}\dot{q}_1\\ \dot{q}_2\\ \dot{q}_3\\ \dot{q}_4\end{pmatrix} = \frac{1}{2}\begin{bmatrix} q_4 & -q_3 & q_2\\ q_3 & q_4 & -q_1\\ -q_2 & q_1 & q_4\\ -q_1 & -q_2 & -q_3\end{bmatrix}\begin{pmatrix}\omega_1\\ \omega_2\\ \omega_3\end{pmatrix} \tag{3.34}$$

Or,

$$\dot{\boldsymbol{q}} = \frac{1}{2}\boldsymbol{Q}\boldsymbol{\omega}, \qquad \boldsymbol{Q} = \begin{bmatrix} q_4 & -q_3 & q_2\\ q_3 & q_4 & -q_1\\ -q_2 & q_1 & q_4\\ -q_1 & -q_2 & -q_3\end{bmatrix} \tag{3.35}$$

Equation (3.35) shows the change in orientation of two reference frames with time, rotating with an angular velocity ($\boldsymbol{\omega}$) in terms of quaternion co-ordinates.

3.4.2. Dynamic Equations

The dynamics of a body acted upon by forces can be formulated using several methods. Most commonly used methods are Newtonian, Lagrangian and Hamiltonian mechanics. According to Likins (1974), the Newton-Euler method is a better fit for simple geometries and rigid bodies. However, Lagrange's and Hamilton's principle are best suited for deriving more complex and flexible multi-body systems.

Assuming a rigid body with constant mass and angular momentum about its CoM,$\boldsymbol{H}$, is given by (Wie, 1998):

$$\boldsymbol{H} = \boldsymbol{I}\boldsymbol{\omega} \tag{3.36}$$

where $\boldsymbol{\omega}$ is the angular velocity and $\boldsymbol{I}$ is the inertia tensor given by,

$$\boldsymbol{I} = \begin{bmatrix} I_{xx} & -I_{xy} & -I_{xz}\\ -I_{xy} & I_{yy} & -I_{yz}\\ -I_{xz} & -I_{yz} & I_{zz}\end{bmatrix} \tag{3.37}$$

Further, the external moment around the CoM would result in a rate of change of angular momentum:

$$\boldsymbol{M} = \left(\frac{\mathrm{d}\boldsymbol{H}}{\mathrm{d}t}\right)_I = \left(\frac{\mathrm{d}\boldsymbol{H}}{\mathrm{d}t}\right)_B + \boldsymbol{\omega}^{B,I} \times \boldsymbol{H} \tag{3.38}$$

The time derivative of angular momentum vector can be further evaluated as:

$$\left(\frac{\mathrm{d}\boldsymbol{H}}{\mathrm{d}t}\right)_B = \boldsymbol{\omega}^{B,I}\left(\frac{\mathrm{d}\boldsymbol{I}}{\mathrm{d}t}\right)_B + \boldsymbol{I}\left(\frac{\mathrm{d}\boldsymbol{\omega}^{B,I}}{\mathrm{d}t}\right)_B \tag{3.39}$$

For a rigid body, $\left(\frac{d\boldsymbol{I}}{dt}\right)_B = 0$. Therefore, using Equations (3.38) and (3.39), Euler's rotational EOM can be written as:

$$\boldsymbol{M} = \boldsymbol{I}\dot{\boldsymbol{\omega}} + \boldsymbol{\omega} \times \boldsymbol{I}\boldsymbol{\omega} \tag{3.40}$$

Re-arranging to get the expression for angular acceleration:

$$\dot{\boldsymbol{\omega}} = \boldsymbol{I}^{-1}(\boldsymbol{M} - \boldsymbol{\omega} \times \boldsymbol{I}\boldsymbol{\omega}) \tag{3.41}$$

The $\boldsymbol{\omega} \times \boldsymbol{I}\boldsymbol{\omega}$ term represents the coupling between the three axes, also known as gyroscopic coupling, and $\boldsymbol{M} = \boldsymbol{M_g} + \boldsymbol{M_d} + \boldsymbol{M_c}$ constitutes all external moments including gravity ($\boldsymbol{M_g}$), other environmental disturbances ($\boldsymbol{M_d}$), and the control moment ($\boldsymbol{M_c}$). However, as stated before, the effect of environmental torques is not considered, so $\boldsymbol{M_d} = \boldsymbol{0}$. Therefore, $\boldsymbol{M}$ only consists of control moments acting on the system.

The equations of motion were derived assuming that the body is rigid. But in some cases, the body may not have a constant mass throughout and cannot be assumed to be rigid by definition. For example, in case the propellant of the spacecraft is burnt or leaked. In such a scenario, two additional external forces come into picture, namely, the Coriolis moment and relative moment due to variable mass. However, in case of Envisat, all the fuel in the tanks is assumed to be completely exhausted and there are no possible modes for a change in mass. Though there will be variation in mass of the chaser during thrusting and de-orbiting, the change in mass is very small, and the associated torques are negligible compared to the control torques and flexibility.

The kinematics and dynamics for a flexible spacecraft strongly depend on the type of formulation. Additionally, the distance between any two points on a FMS can change with its motion (due to flexibility), which in turn affects the EOM. It also depends on the configuration of the spacecraft, the internal forces and the constraints at the contact points between different elements of the multibody system. The flexible body requires special attention and therefore, will be discussed in detail in Chapter 4.

3.5. Guidance

As stated before, the goal of this thesis is to analyse the effect of flexibility on the controllability characteristics of a chaser spacecraft performing ADR operations on a large passive debris with flexible appendages. The guidance system is a block in the GNC system, which generates the commanded state to be achieved by the controller. To analyse the effect of disregarding the flexible body dynamics in the control system design, the guidance is based on the dynamics of a rigid body. By doing this, perturbations due to flexibility are treated as unpredicted external disturbances. This also proves to be advantageous, because flexible bodies react differently, to different kinds of forces in the space environment. For instance, the response or induced vibration due to a debris impact (an impulsive force) will be different from vibrations induced due to slew manoeuvres. It is also assumed that the chaser spacecraft is already in the vicinity of Envisat, and the orbital position is frozen. Since the two phases of the mission being examined are essentially different, the guidance for each phase will be discussed separately.

3.5.1. Synchronisation phase

In the synchronisation phase, the chaser needs to match the attitude of the target debris, which is rotating with an angular velocity of 3.5°/s about all axes (worst case scenario). This means that the guidance must be based on the target attitude, and the target mass moment of inertia, $\boldsymbol{I_{tar}}$ (as stated in Table 2.1) must be used for the EOM. So, the initial target state vector ($\boldsymbol{x_0}$) used for the guidance system with the angular velocity and quaternions (in the same order) can be written as:

$$\boldsymbol{x_0} = (3.5,\ 3.5,\ 3.5,\ 0,\ 0,\ 0,\ 1)^T \tag{3.42}$$

It must be noted that the target attitude changes continuously with time, as it tumbles about all axes. Therefore, the chaser, which is assumed to start with zero angular velocity must be able to accelerate to the target angular velocity, achieve and maintain a stable predefined attitude to perform the docking operation using its tentacles. Because of the large error in angular rates, first this error must be reduced (below certain threshold through control) and after that the commanded attitude can be achieved and stabilised.

3.5.2. Connected phase

In the connected phase, the chaser is assumed to have successfully docked with the target. At this point, detumbling of the stacked configuration can be performed. The stack is assumed to have the same state as that of the tumbling target during synchronisation. In other words, there was no change in angular velocity due to the docking operation. Therefore, the guidance system will now be based on the state expected after de-tumbling. However, for this phase, a number of operations associated with deorbiting will be examined. These include:

- *Detumbling:* Detumbling is associated with the control problem of reducing the angular velocity from the current value (refer Table 2.2) to zero. Therefore, the guidance will command just zero angular rates (for rate control only).
- *Detumbling + reorientation:* This operation involves a combined control of the angular rates as well as the attitude, which results in detumbling and reorientation to a specified attitude for the final deorbitation manoeuvre.
- *Reorientation:* In this operation, the goal is to achieve a specified attitude to execute the deorbitation manoeuvre. It is assumed here that detumbling has already been performed and the initial angular rates are zero. So, the guidance command consists of both zero angular rates and a specified attitude, because angular velocities must remain zero even after the reorientation attitude is achieved.

3.6. Attitude Control

Attitude control of satellites with large, flexible appendages can become complicated in the presence of oscillations induced due to (sudden) attitude changes. The stacked configuration of a chaser spacecraft with a large, passive target aggravates the controller even more, considering the asymmetry in both mass properties and geometry. The classical PD (Proportional and Derivative) controller, which is still widely used in spacecraft attitude control, may not be robust enough to handle the perturbations due to flexibility caused by abrupt commanded manoeuvres. Further, if the control input is not smooth, it may result in adding to the vibration of the solar panels. Robust control algorithms that can counteract the uncertain nonlinear dynamics provide a possible way to guarantee the stability of the satellite. According to Liu and Tavakoli (2011), by appropriately inverting the dynamic model of the plant to be controlled, a control law can be constructed such that the nonlinear part of the dynamics is linearised, the interactions between the regulated variables are decoupled, and time characteristics of the decay of the state errors can be analysed individually. This allows the controller with non-linear perturbations better. One such control system that is based on the dynamics of the system is, Nonlinear Dynamic Inversion (NDI). The NDI controller enables multivariable control and avoids gain-scheduling by directly incorporating the nonlinear dynamics in the control law. However, NDI is sensitive to model mismatches and measurement errors, which can result in instability. Therefore, a variation of NDI called Incremental Nonlinear Dynamic Inversion (INDI) was developed to retain the advantages and to reduce vehicle model dependency of NDI (Sieberling et al., 2010). This controller with its increased robustness may become a good fit for attitude control in the presence of elastic disturbances. It must be noted that the primary goal is to study the effect of flexibility on controller performance, without trying to optimise the controller.

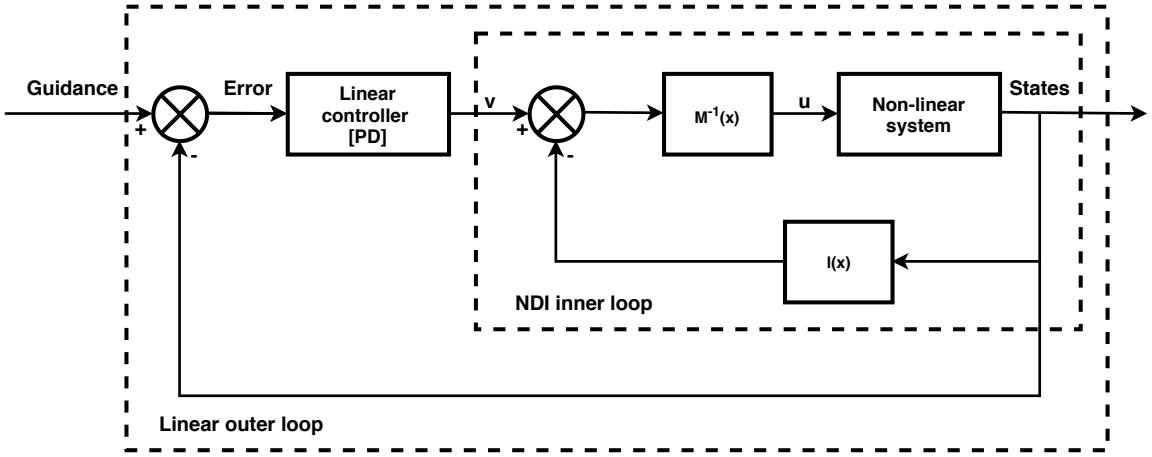

Figure 3.6: Schematic of a typical NDI controller

3.6.1. PD Controller

A linear PD controller is still among the most widely used controllers for attitude control. These controllers are mostly used for problems, where the steady-state error is not zero. The control moment is defined using:

$$\boldsymbol{M_c} = -(\boldsymbol{K_p e} + \boldsymbol{K_d \dot{e}}) \tag{3.43}$$

where $\boldsymbol{K_p}$ and $\boldsymbol{K_d}$ are proportional and derivative gains, respectively. The error in state and state derivative are defined by $\boldsymbol{e}$ and $\boldsymbol{\dot{e}}$, respectively. For quaternions, the error state is denoted by $\boldsymbol{q_e}$ instead of $\boldsymbol{e}$, and $\boldsymbol{\dot{q}_e}$ instead of $\boldsymbol{\dot{e}}$. Quaternions being a four parameter representation, cannot be simply subtracted to get the error. The error, $\boldsymbol{q_e}$ is computed using the quaternion multiplication as shown in Equation (3.15), and its derivative is simply calculated using differentiation. This is given by:

$$\boldsymbol{q_e} = \boldsymbol{Q_c q} \tag{3.44}$$

$$\boldsymbol{\dot{q}_e} = \boldsymbol{\dot{Q}_c q} + \boldsymbol{Q_c \dot{q}} \tag{3.45}$$

where

$$\boldsymbol{Q_c} = \begin{bmatrix} q_{4c} & q_{3c} & -q_{2c} & -q_{1c} \\ -q_{3c} & q_{4c} & q_{1c} & -q_{2c} \\ q_{2c} & -q_{1c} & q_{4c} & -q_{3c} \\ q_{1c} & q_{2c} & q_{3c} & q_{4c} \end{bmatrix} \tag{3.46}$$

and $\boldsymbol{q}$ is the quaternion vector and $\boldsymbol{Q_c}$ is a square matrix of commanded quaternions.

3.6.2. Incremental Nonlinear Dynamic Inversion

As stated before, the INDI controller is an enhanced modification of the NDI controller. In a spacecraft attitude control problem, where the dynamics are nonlinear and often changing from one operation to another, for a linear controller often a single set of gains is insufficient to ensure efficient control. In such a case, gain scheduling needs to be done to adapt the controller according to the operations. However, by using a nonlinear feedback controller like NDI (or INDI), the need for gain scheduling can be eliminated and closed-loop stability is ensured.

An NDI controller typically consists of two loops. The outer loop linearises the system introducing a virtual control, $\boldsymbol{v}$, which is used in the inner loop as shown in Figure 3.6. The control moment is then obtained using:

$$\boldsymbol{M_c} = \boldsymbol{M^{-1}(x)(v - l(x))} \tag{3.47}$$

where $\boldsymbol{M(x)}$ and $\boldsymbol{l(x)}$ depend on the state variables ($\boldsymbol{x}$) and are given by:

$$\boldsymbol{M(x)} = \frac{\partial}{\partial \boldsymbol{x}}(\boldsymbol{N\omega} + \boldsymbol{\Gamma}) \begin{bmatrix} \boldsymbol{0_{3\times 3}} \\ \boldsymbol{I^{-1}} \end{bmatrix} \tag{3.48}$$

$$\boldsymbol{l(x)} = \frac{\partial}{\partial \boldsymbol{x}}(\boldsymbol{N\omega} + \boldsymbol{\Gamma}) \begin{bmatrix} \boldsymbol{N\omega} + \boldsymbol{\Gamma} \\ \boldsymbol{I^{-1}(\omega \times I\omega + M_g + M_d)} \end{bmatrix} \tag{3.49}$$

Here, the notations used are the same as those used to derive the rigid body EOM. The PD controller is used as the outer loop linear controller, which gives the virtual control by using Equation (3.43). The terms $\boldsymbol{N}$, $\boldsymbol{\Gamma}$ and the associated Jacobian depend on the state and the kinematic equations of the system. Using Equation (3.34), $\boldsymbol{N}$ and $\boldsymbol{\Gamma}$, which are basically the coefficient matrices in the EOM, can be written as:

$$\boldsymbol{N} = \frac{1}{2}\boldsymbol{Q}, \qquad \boldsymbol{Q} = \begin{bmatrix} q_4 & -q_3 & q_2 \\ q_3 & q_4 & -q_1 \\ -q_2 & q_1 & q_4 \\ -q_1 & -q_2 & -q_3 \end{bmatrix} \tag{3.50}$$

$$\boldsymbol{\Gamma} = \begin{pmatrix} 0 & 0 & 0 & 0 \end{pmatrix}^T \tag{3.51}$$

After evaluating the Jacobian, it is substituted into Equations (3.48) and (3.49) to find $\boldsymbol{M(x)}$ and $\boldsymbol{l(x)}$, and the final control moment can be computed.

In cases where the dynamic models are very complex, dynamic inversion becomes difficult and may lead to incorrect results. Therefore, an alternative approach of INDI alters the structure of NDI in such a way that only a small part of the model is used and the model mismatch is minimised (Sieberling et al., 2010). The change in dynamics (or angular velocity) per unit time is approximated by a first-order Taylor series. With the notation “0" indicating the nominal case, the dynamics can be approximated by:

$$\dot{\boldsymbol{\omega}} \approx \dot{\boldsymbol{\omega}}_{\boldsymbol{0}} + \frac{\partial \dot{\boldsymbol{\omega}}}{\partial \boldsymbol{\omega}}\Big|_{\boldsymbol{\omega_0}} (\boldsymbol{\omega} - \boldsymbol{\omega_0}) + \frac{\partial \dot{\boldsymbol{\omega}}}{\partial \boldsymbol{u}}\Big|_{\boldsymbol{u_0}} (\boldsymbol{u} - \boldsymbol{u_0}) \tag{3.52}$$

The first term of the equation is the angular acceleration that can be obtained from onboard sensors in a real life implementation. For high sampling rates, when the difference between new and current angular acceleration becomes small, the equation can be further reduced. The partial derivative with respect to the state, i.e., the second term, can then be neglected. Therefore, the equation becomes

$$\dot{\boldsymbol{\omega}} \approx \dot{\boldsymbol{\omega}}_{\boldsymbol{0}} + \frac{\partial \dot{\boldsymbol{\omega}}}{\partial \boldsymbol{u}} (\boldsymbol{u} - \boldsymbol{u_0}) \tag{3.53}$$

The second partial derivative can be derived from the dynamic equation of motion, Equation (3.41), which is simply found to be $\frac{\partial \dot{\omega}}{\partial \boldsymbol{u}} = \boldsymbol{I^{-1}}$. Using the notation $\Delta \boldsymbol{M_c} = \boldsymbol{u} - \boldsymbol{u_0}$ to represent the difference between the control moments of the current and the previous timesteps, and re-arranging Equation (3.53), we get:

$$\Delta \boldsymbol{M_c} = \boldsymbol{I}(\boldsymbol{\nu} - \dot{\boldsymbol{\omega}}_{\boldsymbol{0}}) \tag{3.54}$$

The virtual control term ($\boldsymbol{\nu}$) is computed using a PD controller with dynamic inversion, which is applied in two loops. This is to obtain a Time Scale Separation (TSS) in the inversion of the dynamics, which allows quicker control. The outer loop is defined by:

$$\dot{\boldsymbol{x}}_{\boldsymbol{2}} = \boldsymbol{N}\boldsymbol{u}_{\boldsymbol{2}} \tag{3.55}$$

where $\boldsymbol{x_2} = \boldsymbol{\theta}$, $\boldsymbol{u_2} = \boldsymbol{\omega}$ and $\boldsymbol{N}$ is a matrix used for dynamic inversion of the plant given by Equation (3.50). However, it was found that $\boldsymbol{N}$ matrix, that represents the rigid body kinematics in the INDI

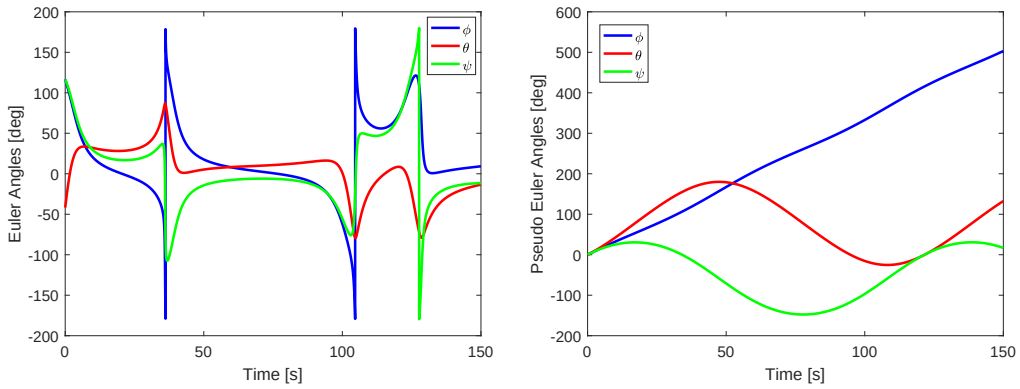

(a) Euler angles (b) Pseudo Euler angles

Figure 3.7: Synchronisation phase

controller degenerates once the attitude exceeds ±180° of rotation. While it is possible to correct the problem by using the MRP representation, an easier alternative was used to solve the problem. By observing the angular rates of a body about an axis, it is possible to derive the evolution of attitude about the same axis by simple integration. This virtually represents the Euler angles without the singularity, and will be referred to as "*pseudo Euler angles*" for the rest of the research. From Figure 3.7, it can be seen that for Euler angles, discrete jumps are observed in the target attitude during the synchronisation phase. Pseudo Euler angles being infinitesimal increments in angles, show a continuous representation of attitude. The kinematics of the rigid body system can be simply defined using the angular velocity. This gives:

$$\dot{\boldsymbol{\Theta}} = \begin{pmatrix} \dot{\Phi} \\ \dot{\Theta} \\ \dot{\Psi} \end{pmatrix} = \begin{pmatrix} \omega_1 \\ \omega_2 \\ \omega_3 \end{pmatrix} \tag{3.56}$$

$\boldsymbol{N}$ is defined as the coefficient matrix that establishes the relation between the rate of change of attitude, $\dot{\boldsymbol{\Theta}}$, with the angular rates of the system, $\boldsymbol{\omega}$. From Equation (3.56), it can be concluded that $\boldsymbol{N}$ becomes an identity matrix for this formulation.

Going back to the outer loop, the virtual control is defined by the error in attitude (as compared to commanded) and the proportional gain.

$$\boldsymbol{v_2} = -\boldsymbol{K_p}\boldsymbol{e} \tag{3.57}$$

Here, for pseudo Euler angles, $\boldsymbol{e}$ can be mathematically represented as:

$$\boldsymbol{e} = \boldsymbol{\Theta_c} - \boldsymbol{\Theta} \tag{3.58}$$

where $\boldsymbol{\Theta_c}$ are the commanded pseudo Euler angles and $\boldsymbol{\Theta}$ are the current pseudo Euler angles. It must be stated that:

- Pseudo Euler angles cannot be used for complete attitude representation with respect to a reference frame in the classical sense, because they are derived from the angular rates and simply represent an incremental change in attitude with time. However, it should be noted that they are only used for the controller design, which is mainly aimed at angular rate control in both synchronisation (rate change from 0°/s to 3.5°/s) and detumbling (rate change from 3.5°/s to 0°/s). The attitude is still represented using quaternions. The kinematics are fully representative by using pseudo Euler angles and serve the objective of this research.

- For the re-orientation manoeuvre (see Section 3.5), which is performed for the connected phase, the initial rate is assumed to be zero. Therefore, any angle change specified using Euler angles will require the same amount of rotation as that when using pseudo Euler angles. Therefore, the choice to use these angles still holds.

The virtual control is used by the outer loop to get the first control vector $\boldsymbol{u_2}$,

$$\boldsymbol{u_2} = \boldsymbol{N}^{-1}(\boldsymbol{v_2}) \tag{3.59}$$

This control vector, $\boldsymbol{u_2}$, is then fed as a reference to compute the virtual control again into the inner loop, given by:

$$\boldsymbol{v} = -\boldsymbol{K_d}(\boldsymbol{x_1} - \boldsymbol{u_2}) \tag{3.60}$$

This can be substituted into Equation (3.54) to obtain the change in control effort ($\Delta \boldsymbol{M_c}$). The final control torque is given by:

$$\boldsymbol{M_c} = \boldsymbol{M_{c,0}} + \Delta \boldsymbol{M_c} = \boldsymbol{M_{c,0}} + \boldsymbol{I}(\boldsymbol{v} - \dot{\boldsymbol{\omega}}_{\boldsymbol{0}}) \tag{3.61}$$

Having discussed the theory for the two controllers used in this research, the FMD used to define the plant will be discussed in the coming chapter. Since the goal is to analyse the effect of flexible dynamics originating from the plant, it will be assumed that both sensors and actuators measuring rigid body motion are ideal. When optimising the controller design, more realistic models for sensors and actuators should be used to assess the controller performance. However, this is currently beyond the scope of this thesis. Before proceeding to the next chapter, a benchmark for the controller performance will be established in the next subsection.

3.6.3. Benchmark Simulations

The controllers can be tested for the rigid body model to establish their performance against a more nonlinear flexible model. Additionally, it will be interesting to see the performance of PD and INDI controllers for a rigid body model without any perturbations, as compared to the flexible model with vibrations. Therefore, in this section some results from rigid body simulations will be presented and analysed. All the rigid body simulations were performed with a controller frequency of 25 Hz and a standard RK4 (Runge Kutta 4th order) integrator. The gains used for the synchronisation and connected phase for all controllers are stated in Table 3.3. In the table, $\boldsymbol{K_p}$ represents the proportional gains and $\boldsymbol{K_d}$ the derivative gains.

From Table 3.3, on analysing the gains, it can be observed that in the synchronisation phase, the same gain for all three axes could be used for both PD and INDI. This is because the chaser satellite does not have a large variation in the moment of inertia, and does not have large differences in the dynamics about the three axes. Contrarily, the dynamics in the connected phase, is very different about the three axes, due to large disparity in inertia about these axes. This is reflected on the PD gains, which had to be tuned separately for the three axes. The INDI does not suffer from this problem, because it is based on the inverse dynamics and already accounts for the change in dynamics in the controller.

Figure 3.8 shows the performance of both PD and INDI controller for the synchronisation

Table 3.3: Controller Gains

	Synchronisation Phase		Connected Phase	
Controller	$\boldsymbol{K_p}$	$\boldsymbol{K_d}$	$\boldsymbol{K_p}$	$\boldsymbol{K_d}$
Rate	-[500,500,500]	-	-[5000,1500,4500]	-
PD	[250,250,250]	[500,500,500]	[30,15,52.5]	[5000,1500,6000]
INDI	-[1.44,1.44,1.44]	[0.935,0.935,0.935]	-[0.0075,0.0075,0.0075]	[0.1125,0.1125,0.1125]

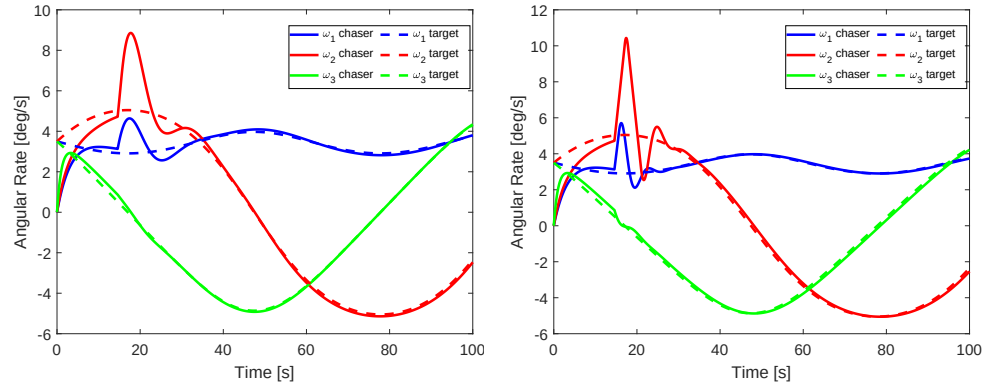

(a) PD angular rates (b) INDI angular rates

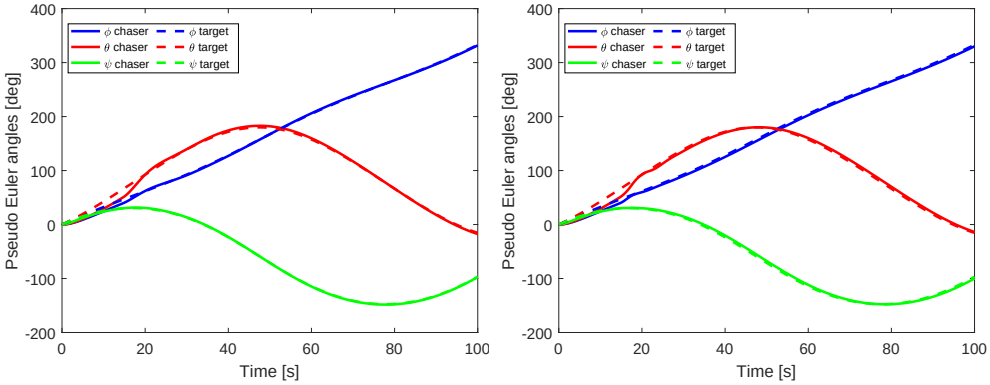

(c) PD pseudo Euler angles (d) INDI pseudo Euler angles

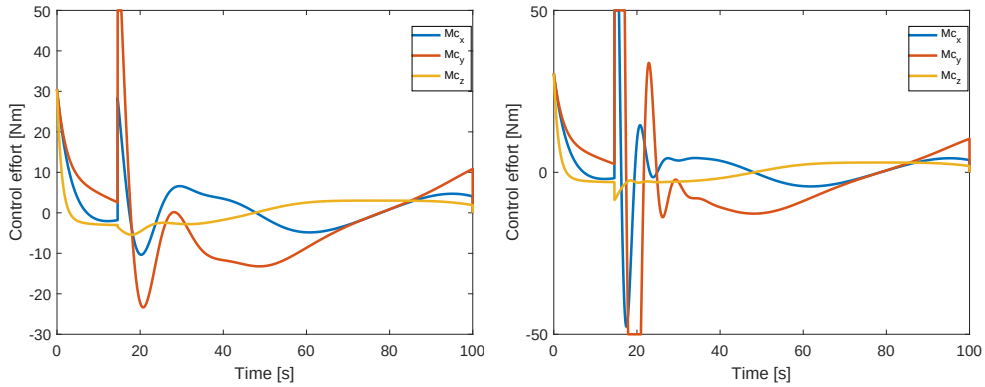

(e) PD control effort (f) INDI control effort

Figure 3.8: Rigid body control - Synchronisation phase

phase. Since the guidance command (Envisat) is constantly changing with time, first rate control (simple proportional control) is performed until the angular rate error reaches a norm of 0.5 °/s and then, the PD and INDI controllers are used to achieve full state stabilisation. For the synchronisation phase, both controllers achieve steady state with comparable performance. The INDI seems to have a faster settling time, but also suffers from a larger overshoot, when the switch from the rate control to full control is performed. On comparing the convergence of angular rates from Figure 3.8(a) and Figure 3.8(b), it can be observed that both controllers suffer from small steady state errors. From

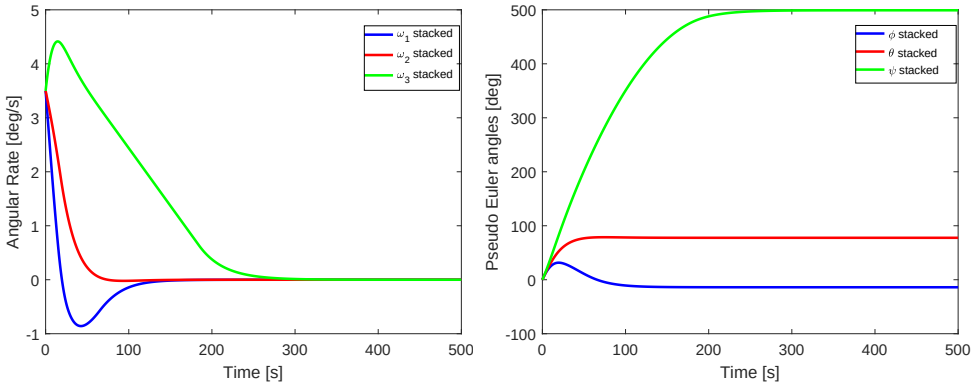

(a) Angular rates (b) Pseudo Euler angles

Figure 3.9: Rigid body control - Detumbling phase

analysis, it was found that the performance of both the controllers can be slightly improved by increasing the sampling frequency of the controller. However, the INDI controller still suffered from a slight steady state error, which could be due to the large overshoot when switching from the rate to full control. This can be confirmed by observation of controller performance in the connected phase.

Figure 3.9 shows a simple detumbling control performed using a rate controller. Here, the controller did not make an effort to stabilise the attitude. However, from Figure 3.9(a) it can be seen that the basic proportional controller successfully detumbles the satellite in its stacked configuration. Also, from Figure 3.9(b), it can be seen that the attitude has also been stabilised.

Figure 3.10 shows the performance of PD and INDI controllers for the detumbling as well as reorientation phase. Again both controllers successfully stabilise the system and give comparable performances in terms of settling time. However, the response of INDI is slightly smoother compared to PD controller, with the penalty of more saturated controls. Another observation that can be made here, is that there is no steady state error in INDI controller as it was seen in the synchronisation phase. This confirms the fact that the error was induced due to the switch between the controllers.

Lastly, Figure 3.11 shows the performance of the two controllers to achieve a prescribed attitude starting from zero angular velocity. Again, both controllers show comparable performance in terms of convergence and settling time. A more dynamic system would help analyse the performance of the two controllers better. Another observation that can be made about all phases except setpoint control (or reorientation), is that the time history of the pseudo Euler angles show that large excursions take place about all axes, which cannot be represented using Euler angles due to the singularity. This confirms the choice of quaternions for attitude representation in the EOM. As the angular displacement is beyond the range of $\pm 180°$, it also shows that quaternions could not be used in the INDI controller.

With these results as a benchmark, now the flexible model can be added to the system, and the analysis will be performed again using the same gains as for the benchmark simulations.

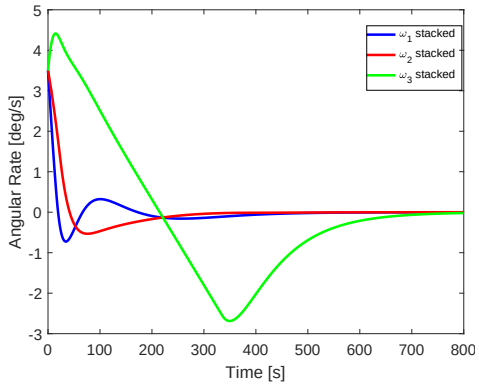

(a) PD angular rates

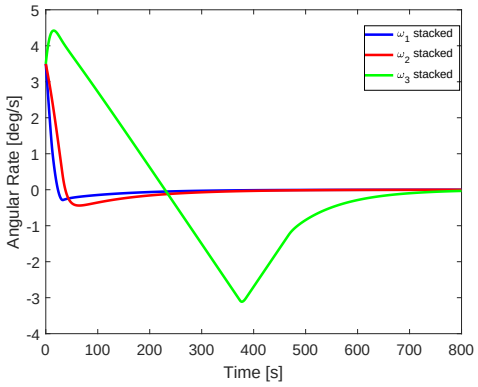

(b) INDI angular rates

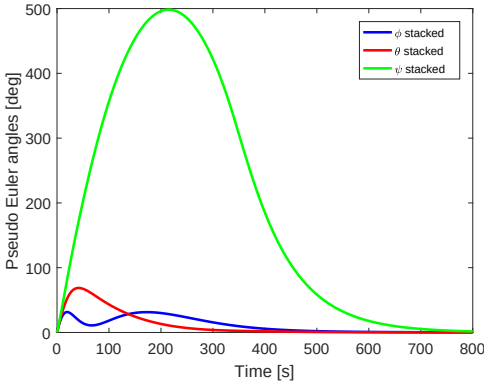

(c) PD pseudo Euler angles

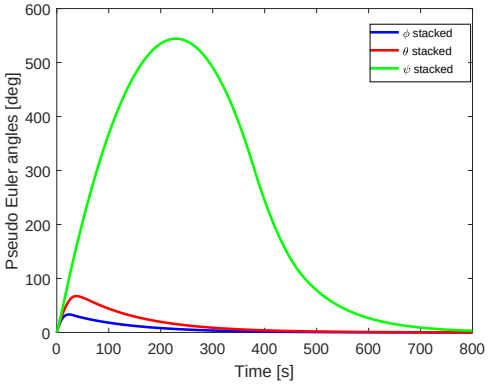

(d) INDI pseudo Euler angles

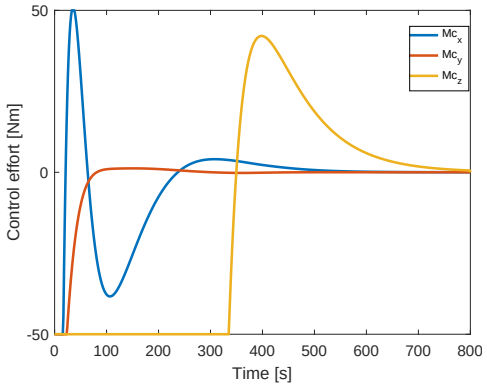

(e) PD control effort

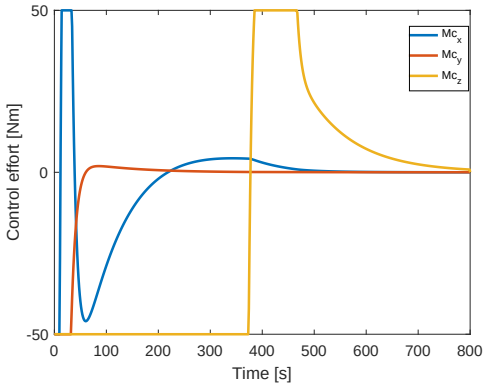

(f) INDI control effort

Figure 3.10: Rigid body control - Detumbling + Reorientation phase

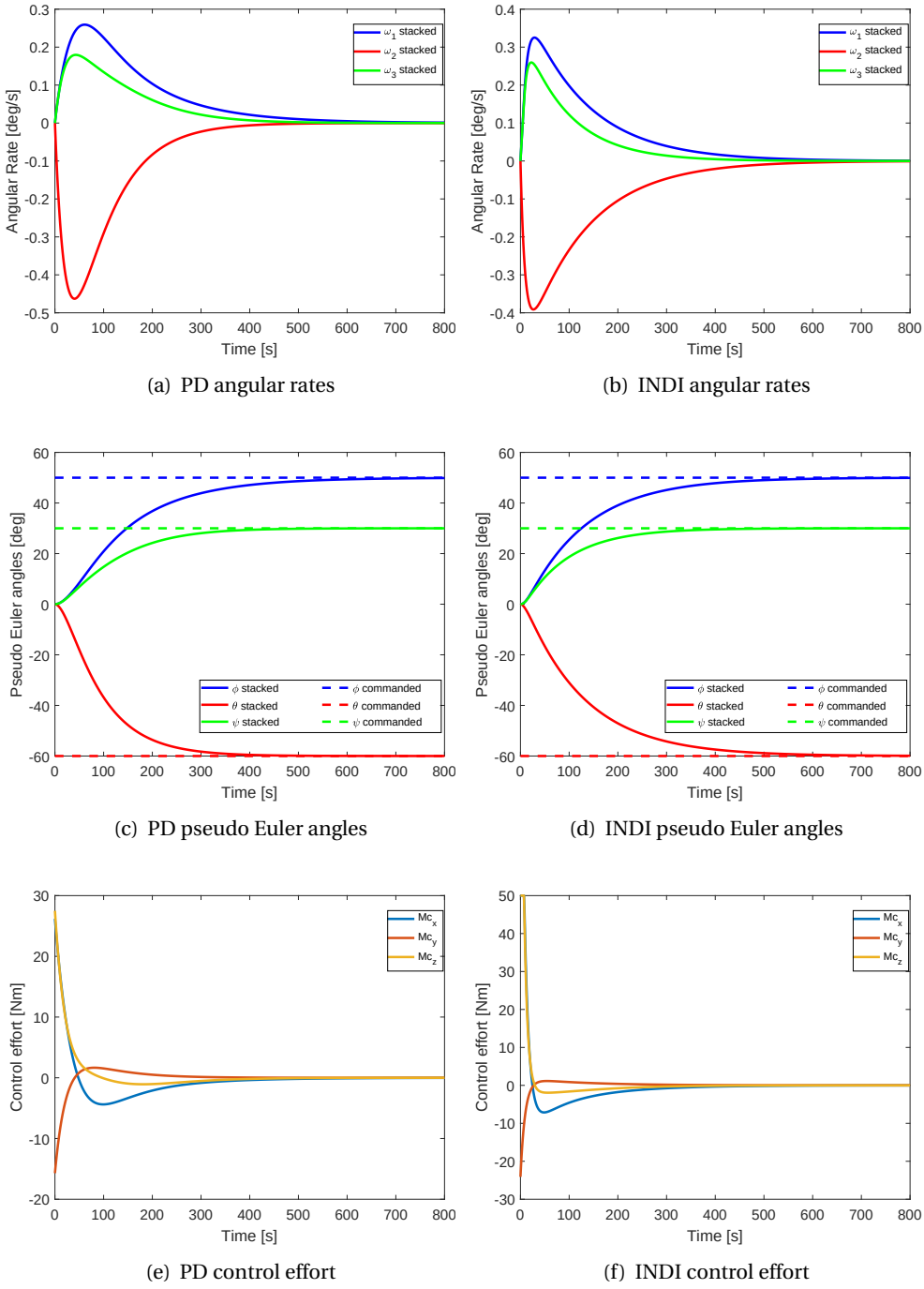

(a) PD angular rates

(b) INDI angular rates

(c) PD pseudo Euler angles

(d) INDI pseudo Euler angles

(e) PD control effort

(f) INDI control effort

Figure 3.11: Rigid body control - Set point control

4

Flexible Multibody Dynamics

In the past, spacecraft were small and modelled as rigid bodies for its (system) attitude control design. However, many satellites today have large flexible appendages to meet the high power requirements of current day missions. For a quick judgement of motion in a multibody system, often it is acceptable that the elements of the system are considered rigid. However, when high accuracy is required (like to maintain precision pointing of a satellite), the flexibility in the structural elements cannot be ignored. To minimise computation time and capture the dynamics of vibration due to flexible elements, an accurate yet computationally inexpensive formulation is required. The FMD deals with the study of machines and mechanisms, especially when multiple deformable bodies are involved. This requires the mindful choice of a number of elements, including reference frames, coordinate systems, internal forces associated with flexibility, constraints and so on.

In this chapter, first the different formulations for reference frames for a flexible multibody system will be studied and the most fitting model will be selected in Section 4.1. This will be followed by the derivation of the generalised EOM and possible discretisation of flexible elements to describe the vibrations in Section 4.2. Then, in Section 4.3, the force, modal reduction techniques (to optimise computation time) and constraint modelling for the selected formulation will be investigated. Lastly, the kinematic and dynamic EOM will be derived for the current multibody system in Section 4.4.

4.1. Reference Frame Formulation For Flexible Multibody Systems

To define the complete kinematics and dynamics of a FMS, a number of reference frame formulations can be used. To reduce the simulation time and to capture the vibrational motion of the flexible appendages, the effect of deformation can be approximated by superimposing small linear vibrations on the rigid body motion, also called mean rigid body motion. So, the formulation should be such that the resulting EOM can define the mean rigid body motion of the system, when exposed to large rotations. Three essentially different, but commonly used formulations in FMD are: the inertial frame formulation, the co-rotational frame formulation, and the floating frame formulation. In this section, first the three formulations will be briefly defined. Then, a detailed comparison will be made based on characteristics relevant to the research.

4.1.1. Inertial Frame Formulation

The inertial frame formulation directly defines the motion of the FMS with respect to the central body, which is Earth (in this case). In other words, the inertial frame serves as a global reference for the system. According to Wasfy and Noor (2003), it is derived from the nonlinear Finite Element Method (FEM) and continuum mechanics, which will be discussed in Section 4.2.2. Each body is

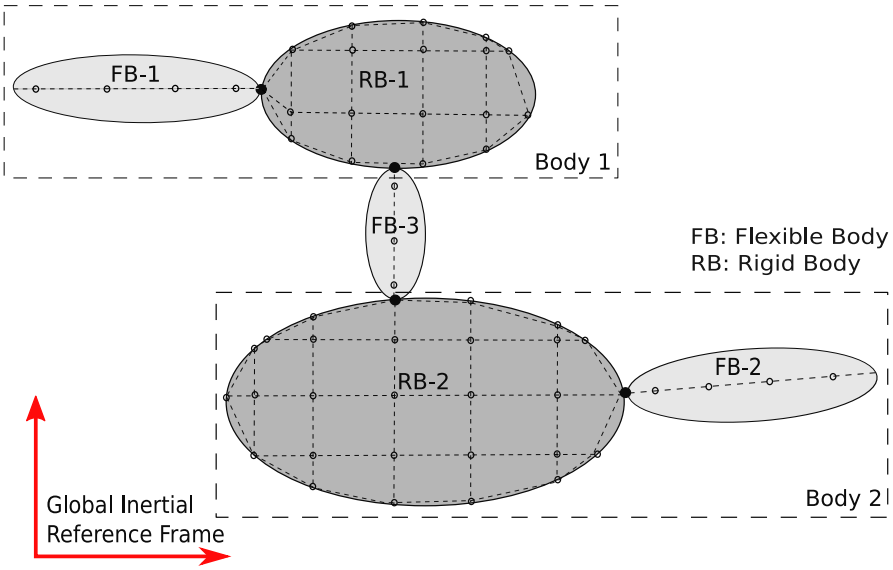

Figure 4.1: Multibody representation in an inertial reference frame

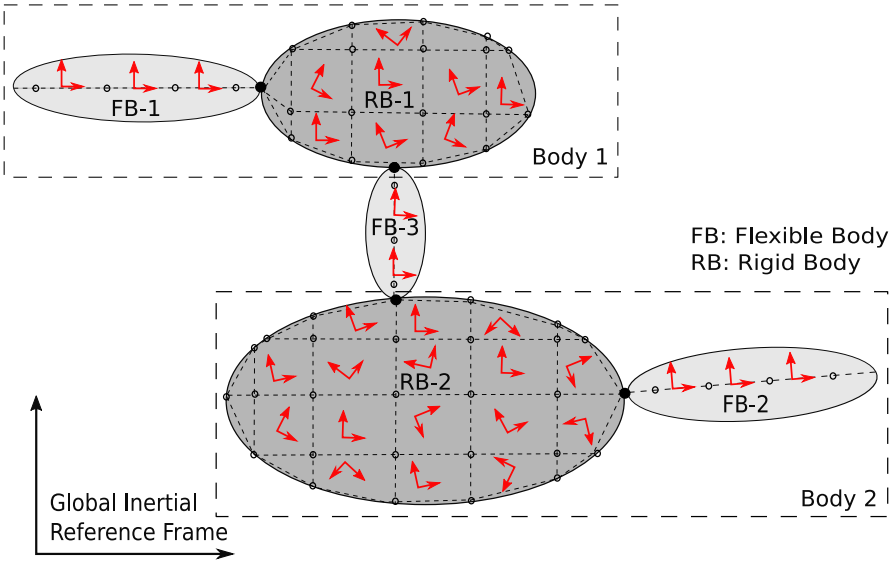

Figure 4.2: Multibody representation in a co-rotational reference frame

then discretised forming a finite mesh. The DOF of such a system are defined by absolute position and orientation of the local coordinate frames at the nodes of the discretised body. This can be visualised using Figure 4.1, in which the complete system is divided into nodes and defined with respect to the global inertial reference frame (marked in red). Some important characteristics of this formulation relevant to this research, like modelling of deformation, angular velocities, computation time, accuracy, and so on, are listed in Table 4.1 with respect to the current application. These will be discussed in more detail in Section 4.1.4

It is often desirable to establish additional reference formulations to be able to analyse individual contributions of flexible elements to the mean rigid motion of the body. Two such formulations are: co-rotational frame and floating frame.

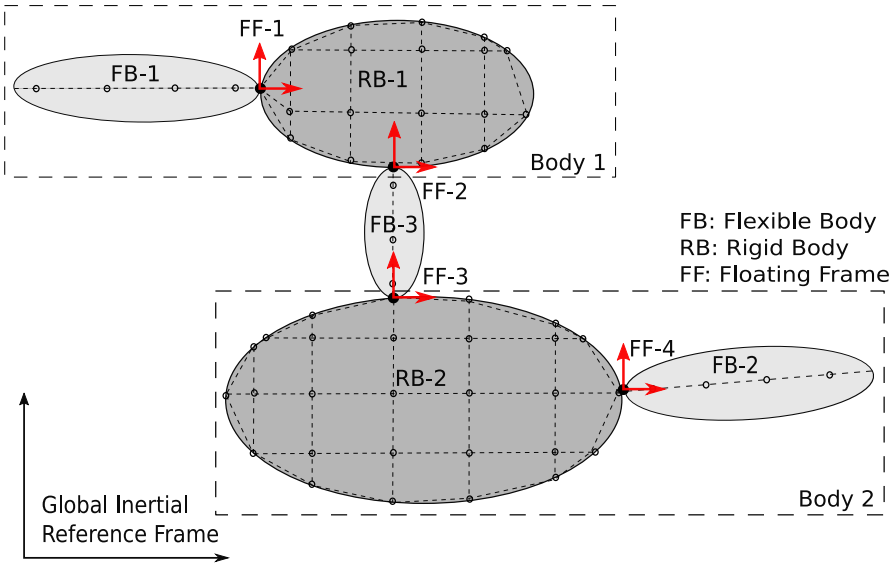

Figure 4.3: Multibody representation in a floating reference frame

4.1.2. Co-rotational Frame Formulation

The Co-rotational Frame Formulation can be defined as a nonlinear extension of the linear FEM formulation. The motion of the body is defined using rigid body motion and flexible modes at their natural frequency. This formulation is derived from the field of structural dynamics, wherein the (large) rigid body motion is defined with respect to the inertial frame, and small elastic deformations in the elements are superimposed using linear FEM mass and stiffness matrices. The formulation still captures the nonlinear elastic deformation within an element, because each discretised element has its own reference frame, as visualised in Figure 4.2, with the co-rotational frames marked in red. This can be simply transformed into the global inertial frame (nonlinear formulation) using rotation matrices. The individual reference frame at the nodal points or any other point (defining the mean rigid body motion) of the discretised element is a type of reference frame called co-rotational frame. As for the inertial frame formulation, some key characteristics of this formulation are discussed in Table 4.1.

4.1.3. Floating Frame Formulation

The Floating Frame Formulation is an extension of rigid multibody dynamics to a flexible multibody system. In this method, small elastic deformations are superimposed on large rigid body motion to represent the motion of floating frame, which moves along with the body. The elastic deformations are obtained from mode shapes and eigenfrequencies, which are either computed numerically or experimentally for each flexible link. From Figure 4.3, it can be observed that the floating reference frame is present for every element at the interface points of the system. The interface points are the point of connection between two elements or the end nodes of the multibody system. The floating frames can be placed anywhere on the multibody system, but placing them at the interface points, where rigid and/or flexible bodies connect, allows easy application of constraints and facilitates modelling of rigid-flexible or flexible-flexible coupling (Wasfy and Noor, 2003). However, the interface coordinates do not contribute to the DOF of the system and require additional constraint equations in the EOM, which are nonlinear and add to the total number of unknowns to be solved for. This disadvantage can be eliminated using the new formulation of the floating frame in terms of absolute interface coordinates given by Ellenbroek and Schilder (2017). In this method, the floating frame is defined in terms of the local coordinates at the interface points (instead of the typical definition with respect to inertial). The local coordinates are then defined directly in the inertial frame.

Some other important characteristics of the floating frame are summarised in Table 4.1.

4.1.4. Comparison of the approaches

Table 4.1 summarises the properties of the three approaches for FMD modelling. In this section, some of the desirable properties required for the current application will be discussed and then, Table 4.1 will be used to find the most fitting approach/approaches based on their advantages and disadvantages. Some desirable properties are stated below:

- **Deformation:** The deformation of all flexible elements should be represented in the formulation. The approach should be able to record the deformation either in the local frame or in the global frame. From Table 4.1, all the approaches are capable of denoting the deformation in flexible components. However, for this research the computations will be performed within the frame of linear elastic theory and the elastic deformation in the flexible appendages will be considered small. The floating frame is better suited for this application as compared to the other two formulations, which model larger deflections better.

- **Angular velocity:** Since Envisat is tumbling with a relatively large, uncontrolled angular velocity of 3.5°/s, the reference frame formulation should be able to model large angular velocities. Again, all three approaches can be used to model large angular velocities.

- **Mixed rigid and flexible body configuration:** The system comprises of multiple flexible appendages as well as rigid bodies, when in stacked configuration. The formulation should be able to capture both rigid and flexible body motion. It should also be easy to model the rigid bodies alone to analyse the effect of flexibility on the system. From the table, it can be concluded that the floating reference frame is very adaptable with modelling both rigid and flexible configurations, while many co-rotational and the inertial frame formulations have some restrictions for a completely rigid body.

- **Inertial forces:** When a body is defined in a non-inertial frame, the effect of apparent forces, like centrifugal and Coriolis forces, need to be taken into account. Additionally, if the flexible motion is defined in the local frame, coupling terms should be introduced to link the rigid body motion with the flexible modes (refer to Section 4.3.2 for details). These forces are mainly introduced in the floating frame, because the frame also translates with respect to inertial and the flexible modes are defined with respect to the floating frame. The inertial forces are absent in the other two formulations, because the inertia tensor is defined directly with respect to the inertial frame.

- **Possibility of modal reduction:** By considering only the low frequency modes, which are the major contributors of the vibration characteristics, the model can be made computationally less expensive without loss in accuracy. Nonlinear modal reductions can easily be applied in the floating frame formulation, which is updated every time step. This is not practical in the other two formulations, because the internal forces are calculated at the nodes (in terms of generalised coordinates), and then transformed into a nonlinear formulation through a rotation matrix. Additionally, they need to be updated every time step, which means that the reduction needs to be applied at every time step as well. This beats the purpose of saving computation time.

- **Deflection:** According to Wasfy and Noor (2003), a typical flexible space structure does not suffer from large deflections. Especially for the current test case, large deflections are not expected. Therefore, the formulation should be able to model small deflections correctly. From the table, it can be seen that floating frame is more fitting for small deflections, while the other two are more fitting for large deflections.

- **Computation time:** The computation time should be as low as possible to allow multiple simulations for the control system design. Modal reduction with floating reference frames reduces the computation time almost twofold. This makes the co-rotational and inertial frame formulation relatively slower. Moreover, these two formulations also perform the same with respect to computation time for small and large deformations, because both models are formulated in the same way. The computation time is also dependent on the resolution of discretisation in the FEM model.

- **Constraint handling:** Since the interface points are usually located at the joints, which allow relative rotation between the two bodies, the problem becomes geometrically nonlinear in nature. In such cases, additional constraint equations are required in the floating frame formulation, which cannot be solved analytically (though a new alternative formulation as stated before can rectify the problem). In the inertial and co-rotational frame formulation, such constraints can be imposed in a very simple way by placing the interface points on the body's finite element node at the joint. By doing this, the degrees of freedom of the nodes shared by both bodies can be equated and therefore, constrained.

- **Accuracy:** The accuracy should be high within a reasonable computational load (CPU time), which is superior for the floating reference frame, as compared to the co-rotational and the inertial frame formulations, because it takes the nonlinear coupling terms associated with flexible inertia forces into consideration. The co-rotational formulation also loses some efficiency (and experiences increased computational effort) due to its inability to differentiate between rigid and flexible parts. In other words, rigid bodies are modelled as flexible bodies with high stiffness. Lastly, the inertial frame formulation suffers from frame invariance, which is an apparent lack of variation in some physical quantities (like material properties, mass) due to interpolation of large rotations.

- **Control applications:** To perform multiple control simulations for a complex configuration in the presence of perturbations, there has to be a good balance between accuracy and computation time. This requires an accurate representation of the vibrations in the dynamics of the system in the most condensed or reduced form possible to save computation time. Floating frame formulation dominates in these aspects because the models can be reduced without losing accuracy.

- **Complexity:** The formulation should be easy and less prone to error to ensure correct formulation of the two phases - synchronisation and connected phase. This aspect makes floating frames a risky choice, because the formulation is very dependent on the correct choice of interface points, which requires a certain experience. It is also different for different configurations, which makes the method mathematically exhausting. The other two formulations are based on discretisation models, which can easily be simulated with any FEM software.

Based on the analysis, it can be concluded that the most fitting formulation for this multibody system with small deformations and relatively large rotation speed is the floating frame formulation. Despite its complexity, it provides the advantage of reduced computation time and good accuracy for the control model. Further, it is an extension of rigid multibody dynamics, which allows easy comparison of the rigid and flexible models. The new formulation of floating frames, based on the principle of absolute nodal coordinates given by Ellenbroek and Schilder (2017), even enables straightforward constraint handling, while still allowing the use of linear model reduction techniques. This new method will be discussed in further detail in Section 4.3. Since the floating reference frame is non-inertial, some additional modelling techniques will be required to model the inertial coupling terms. The modal reduction techniques should also be studied along with

Table 4.1: Comparison of three FMD approaches (Wasfy and Noor, 2003)

		Corotational Frame	**Inertial Frame**	**Floating Frame**
1.	**Deformation**	Denoted by corotational frame at each finite element.	Denoted directly with respect to inertial frame.	Denoted by floating frame for each flexible component.
2.	**Angular velocities**	No restriction on angular velocity magnitude.		
3.	**Mixing rigid and flexible bodies**	Most implementations place some restrictions on configuration of a rigid body. For instance, a closed loop system (like a parallel mechanisms) must have at least one flexible body.		Based on multibody dynamics that can easily model both rigid and flexible systems in the same configuration.
4.	**Inertial forces**	The translational part of mass matrix is constant. Effects of coupling between rigid and flexible system, Coriolis and centrifugal forces are absent because the inertia forces (inertia tensor) are defined with respect to inertial frame and remain constant.		The mass matrix consists of nonlinear rigid-flexible coupling terms, which are necessary to account for dynamic response of flexible inertia forces.
5.	**Possibility of modal reduction**	Not practical, because element vector for internal forces is nonlinear in nodal coordinates, since it involves a rotation matrix.	Not practical, because the element vector for internal forces is nonlinear in nodal coordinates since it involves a finite strain measure.	Nonlinear modal reduction can be applied to bodies with non-uniform, large angular velocity. Modal reduction needs to be performed at every time step.
6.	**Deflection**	Suitable for FMS with large deflections and large rotation speeds.		Suitable for FMS undergoing small deflections.
7.	**Computation time**	The computation time does not reduce, even when small deflections are assumed.	The computation time remains the same for both large and small strains.	Reduced almost twofold because of modal reduction.
8.	**Accuracy**	This formulation cannot differentiate between a rigid and a flexible body, and assumes that the rigid body is a stiffer flexible body. This results in a less efficient formulation.	Interpolation of large rotations with respect to the inertial frame leads to frame invariance, which again leads to a less efficient formulation.	Superior accuracy because the coupling between rigid-flexible elements and inertial forces due to flexibility are well accounted for.
9.	**Control application**	Computationally expensive for good accuracy.		Provides a good balance between accuracy and speed.
10.	**Constraint handling**	Possibility of enforcing constraints directly by equating DOF of nodes shared by 2 bodies.		Typically requires Lagrange Multipliers to constrain EOMs.
11.	**Complexity**	Easy to model using discretisation tools like Abaqus, Ansys and so on.		Requires experience and insight to select correct interface points for the application. Relatively complex to model.

the application of constraints, which will be discussed in further detail in the same section. Before jumping into the kinematics and dynamics written in this particular formulation, first the basic steps to set up the generalised equations of motion will be discussed.

4.2. Generalised Equations of Motion

One of the objectives of this research is to model the dynamics of multibody flexible space structures to obtain a realistic simulation of attitude control. The EOM can be derived in many forms depending on the configuration of the system and other properties, like computation time, accuracy and so on. The dynamics governing the attitude should include the vibration of appendages, joint motion, flexibility in connection model (between chaser and Envisat) and any other possible elastic deformations. For this research, it will be assumed that there is no plastic deformation (in the form of bending, elongation, etc.), that is, the computation will be performed within the frame of linear theory of elasticity.

According to Rutkovsky et al. (1970), the most typical way to model a large spacecraft with branched appendages and docked transportation models is by dividing the multi-body elements into two groups :

- *Elastic bodies*: They represent the solar panels and antenna reflectors (like of Envisat).
- *Rigid bodies*: These are assumed to be connected to the rigid central hub via massless links.

The rigid bodies and flexible appendages are strongly coupled. This means that any manoeuvres or perturbations causing vibrations in the flexible appendages will affect the attitude of the entire spacecraft. Additionally, the external torques, like gravity gradient, solar radiation or even a perturbation resulting from a debris impact can also cause disturbances in attitude. Therefore, a good dynamic model is an essential part of an effective three-axes control system. A flexible body has an infinite number of DOFs. By discretising the body into a finite number of DOFs, using discretisation techniques like FEM, Lumped Parameter Model (LPM) and so on, one can represent the dynamics of the entire system with a reasonable accuracy. In this section, different dynamics approaches and discretisation methods for multibody flexible systems are investigated, and the most fitting method for the research is chosen based on the following requirements.

1. The model should be computationally fast and robust for the control system to achieve convergence of attitude error within a finite time.
2. The model should be numerically simple, compact and effective (a good approximation) for the control of Envisat-chaser system.
3. The model should be compatible with the chosen multibody reference frame formulation.

To derive the EOMs, first the concept of generalised coordinates should be introduced. In the study of multibody systems, the generalised coordinates define the local parameters that uniquely define the configuration of any element or system with respect to a reference. The choice of generalised coordinates for a physical system is based on a number of factors. Two such factors are: (a) The configuration of the system (open loop or closed loop), and (b) Easy solution to the equations of motion. Usually, the generalised coordinates are selected such that they provide the minimum number of independent coordinates to define the configuration of a system, which simplifies the formulation of EOM. However, it is possible that a set of generalised coordinates may be dependent and require constraint equations to model the coupling between them, for instance, at the interface points between two bodies.

4.2.1. Dynamics Approaches

Before studying the mathematical modelling (or discretisation) methods for structures, it is important to understand the dynamics approaches used to derive the EOM. The dynamics approach should be able to model the complex asymmetric geometry of a FMS with variable mass distribution in the presence of internal coupling forces (like rigid-flexible coupling) and external torques

coming from the environment. There are different methodologies to derive equations of motion of multi-body systems. The two common categories are the vectorial (or numerical) approaches and the analytical approaches.

Vectorial approaches use theorems based on conservation of linear and angular momentum. Also known as the Newton-Euler method, all physical coordinates and forces in this method are represented by vector quantities. The formulation depends on free-body diagrams, which makes inclusion of reaction forces and interactive forces inevitable. Main limitation of using this method is that it considers the dynamics of individual components of the system separately. This further requires computation of some extra equations due to kinematic constraints and interaction forces (coupling). The vectorial approach becomes laborious and complicated in terms of computations (especially for a FMS) and therefore, it is not the preferred model (Meirovitch, 1980).

On the other hand, analytical approaches (also called Lagrange's method) model the system as a whole without any additional equations for interacting forces. The equations are derived using the Conservation of Energy principle, thereby representing the system mechanics in terms of two scalar functions, kinetic energy and potential energy, and one infinitesimal term, virtual work associated with non-conservative forces (*e.g.*, friction). The formulations also follow the principle of virtual work, which states that, "*The virtual work of the external applied forces on the virtual displacements compatible with the kinematics is zero*". This gives a robust mathematical model, which is independent of the coordinate system used. This makes it an ideal choice for the structural modelling of a flexible spacecraft. Some variational models of this approach are D'Alembert's principle, Hamilton's principle, and Lagrange's principle as stated in Junkins and Kim (1993), which will be discussed below.

D'Alembert's principle

D'Alembert's principle extends the principle of virtual work to structural dynamics. It states that, "*a problem of dynamic equilibrium can be transformed into a problem of static equilibrium by adding the inertia forces — $m_i\ddot{\boldsymbol{x}}_{\boldsymbol{i}}$ to the externally applied forces $\boldsymbol{F_i}$ and constraints forces $\boldsymbol{F_i'}$*". Here, $\ddot{\boldsymbol{x}}_{\boldsymbol{i}}$ denotes the acceleration of i^{th} particle where $i = 1...N$. According to Newton's law, the resultant force $\boldsymbol{R_i}$ for every particle is given by,

$$\boldsymbol{R_i} = \boldsymbol{F_i} + \boldsymbol{F_i'} - m_i\ddot{\boldsymbol{x}}_{\boldsymbol{i}} = \boldsymbol{0} \tag{4.1}$$

The total for all particles can be found by summation and taking into account the constraint forces (which cause zero displacement according to the principle of virtual work). This can be written as:

$$\sum_{i=0}^{N}(\boldsymbol{F_i} - m_i\ddot{\boldsymbol{x}}_{\boldsymbol{i}}).\delta\boldsymbol{x_i} = \boldsymbol{0} \tag{4.2}$$

where $\boldsymbol{\delta x_i}$ is the virtual displacement. The sum $\sum_{i=0}^{N}(\boldsymbol{F_i} - m_i\ddot{\boldsymbol{x}}_{\boldsymbol{i}})$ of the applied external forces and the inertia forces is called the effective force. Unfortunately, this principle is difficult to apply on multibody systems, which are continuously varying with time. It still uses vector quantities expressed in an inertial frame and cannot be translated directly into generalised coordinates. This will be achieved with Hamilton's principle as shown below.

Hamilton's principle

D'Alembert's principle, despite being a complete formulation of dynamic equilibrium, cannot be used, because it defines the position coordinates of particles in the system, which, in general, are not independent of each other as well as time, and thus cannot be formulated in generalised coordinates. Hamilton's principle solves the problem by expressing the dynamic equilibrium in the form of a scalar energy function, which is independent of the coordinate system. The virtual work, δW, due to external forces can be written in the form:

$$\delta W = \sum \boldsymbol{F_i}\delta\boldsymbol{x_i} \tag{4.3}$$

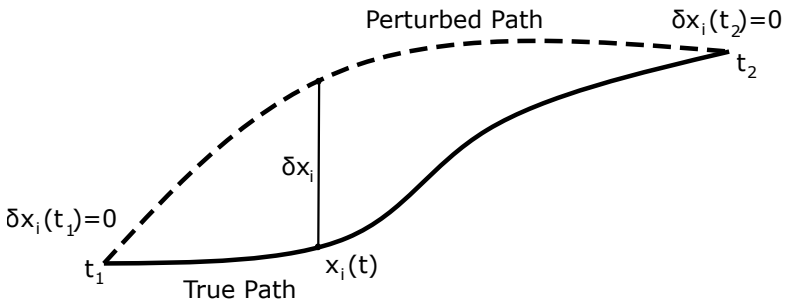

Figure 4.4: True path and perturbed path for dynamic equilibrium

If some of the external forces are conservative, then

$$\delta W = -\delta U + \delta W_{nc} \tag{4.4}$$

where U is the potential energy and δW_{nc} is the virtual work due to non-conservative forces. The dynamic equation then derived using Hamilton's principle (expressed using a Variational Indicator (V.I.) is of the form (see Preumont (2013) for detailed derivation),

$$V.I. = \int_{t_1}^{t_2} [\delta \mathscr{L} + \delta W_{nc}] \mathrm{d}t = 0 \tag{4.5}$$

where

$$\mathscr{L} = T - U \tag{4.6}$$

$\mathscr{L}$ stands for the Lagrangian of the system and T is the kinetic energy of the system. This dynamic formulation changes with time and, therefore, is capable of defining the variable mass distribution and deflection with time. The statement of dynamic equilibrium as stated by Preumont (2013) says that "*the actual path is the one that cancels the value of the variational indicator with respect to all arbitrary variations of the path between two instants t_1 and t_2, compatible with the kinematic constraints such that $\delta \boldsymbol{x_i}(t_1) = \delta \boldsymbol{x_i}(t_2) = 0$*" as shown in Figure 4.4. Another formulation used to solve similar problems is the Lagrange's principle.

Lagrange's principle

Using Hamilton's principle, the flexible system can be defined using generalised coordinates ($\boldsymbol{q_i}$). When the generalised coordinates are independent, the change in the configuration can be represented in terms of virtual variation in generalised coordinates, $\boldsymbol{q_i}$. This allows transformation of Equation (4.5) into a differential equation form. Therefore, T, U and $\mathscr{L}$ can be written as:

$$T = T(q_1, ..., q_n, \dot{q}_1, ..., \dot{q}_n; t) \tag{4.7}$$

$$U = U(q_1, ..., q_n; t) \tag{4.8}$$

$$\mathscr{L} = T - U = \mathscr{L}(q_1, ..., q_n, \dot{q}_1, ..., \dot{q}_n; t) \tag{4.9}$$

On derivation, the Lagrange equations can be written as:

$$\frac{\mathrm{d}}{\mathrm{d}t}\left(\frac{\partial \mathscr{L}}{\partial \boldsymbol{q_i}}\right) - \frac{\partial \mathscr{L}}{\partial \boldsymbol{q_i}} = \boldsymbol{Q_i} \tag{4.10}$$

where $i = 1, ..., n$, equal to number of independent coordinates. $\boldsymbol{Q_i}$ represents all the non conservative forces. This formulation allows us to write the governing EOM in an easy and straightforward way.

Table 4.2: Analysis of modelling techniques

Approach	Advantages	Disadvantages
Global Mode Approach	• Accuracy is high for simple configurations. • Flexibility of the whole system is included directly.	• Needs extensive assumptions to solve complex configurations, which may be impractical.
Rayleigh Ritz Approach	• Good accuracy for low DOF systems. • Quick convergence when the right admissible functions are chosen.	• Higher frequencies show poor convergence characteristics. • Difficult to find fitting admissible functions for complex models.
Lumped Parameter Approach	• Good model for geometrically complex systems. • Mathematically simple and easy to simulate.	• Deflections need to be known at a finite number of locations. • Accuracy low, compared to the mathematical models (like FEM) for the same amount of discretisation.
Finite Element Model	• Structure can be discretised into very small elements for high accuracy. • Every node only affects its neighbour - highly uncoupled system. • Complex geometries can be modelled using dedicated FEM software.	• High-order system matrix - computationally heavy. • Not easy to accommodate physical insights due to design changes (like constraints at joints).

4.2.2. Discretisation Techniques for Structural Modelling

While each mode of vibration contributes to the attitude in some way, the vibration of even a simple beam attached to the spacecraft can have infinite modes. Fortunately, by expressing the elastic deformations as a product of finite mode shapes and generalised coordinates (known as discretisation), one can represent the entire system with reasonable engineering accuracy (Grewal, 1994). Some popular techniques of discretisation include Global Modes Method, Rayleigh-Ritz, Lumped Parameter Method, and Finite Element Method. Another possible way to model the vibrations is by assuming an infinite number of DOF. Such a system is considered to be a distributed or continuous system. It should be noted that discrete and distributed systems are just two mathematical models that can be used to define identical physical systems, it has nothing to do with dynamic characteristics of the system (Meirovitch, 1986). In this section, the most fundamental techniques for structural modelling used for formulating equations of motion are discussed. Mathematical models for such a dynamic system are in the form of differential equations, which can be ordinary differential equations for discrete systems and partial differential equations for continuous systems. The section focusses on understanding how to formulate differential equations and how to solve them efficiently for a flexible spacecraft model. For this, four discretisation options will be analysed. They are:

1. **Global Modes Method:** This approach is a classical method of modelling the equations of motion. The structure is regarded as a distributed parameter system (or continuous system),

which allows the representation of the total flexibility of a body directly. The governing equations consist of differential equations in terms of spatial variables and time dependent factors. The approach can be very accurate for infinite DOF models, provided it has a simple geometry. Sometimes explicit physical assumptions are made to simplify the system and make modelling by this approach more practical. Many appendages, however, are not simple in configuration and partial differential equations of structural dynamics become cumbersome through continuum mechanics.

2. **Rayleigh Ritz Method:** According to Meirovitch (1986), *"The Rayleigh Ritz method is simply a procedure for lowering the estimate of first eigenvalue (λ_1) by producing a trial function ($z_{i,u}$) reasonably close to the first natural mode of vibration"*. In other words, the method discretises the system by assuming certain mode shapes of the elements. Depending on the problem, a sequence of approximate solutions are constructed using admissible or comparative functions. These approximate solutions can be used to solve an arbitrary continuous system (uniform or non uniform) by defining it in the form of discrete linear elements (reducing infinite degrees of freedom to a finite model with n degrees of freedom). For simpler configurations, Rayleigh Ritz acts like the Global Modes Method, because then the system does not require discretisation, and the total flexibility of the system can be represented by a single function. This method can also be used instead of or along with lumped parameter method for a good approximative model.

3. **Lumped Parameter Method:** One simple assumption of this method is that the deflections need to be known at a finite number of locations. The distributed parameters of mass and stiffness are taken to be equivalent to lumped masses at these locations, with lumped stiffness describing the resistance to relative motion, thereby, discretising the system. The sum of the lumped masses and lumped stiffness should be equal to the total mass and stiffness of the system. Since the model is based on approximations of where the deformation might happen, it proves to be less accurate compared to other models with the same discretisation. However, the accuracy can be improved by increasing the lumped parameters. For instance, an infinite number of lumped masses can represent the system exactly.

4. **Finite Element Method:** The mathematical theory of Rayleigh Ritz forms the foundation of the FE model. The displacements of a structure can be expressed in terms of a finite number of discrete coordinates. The structure is first divided into a finite number of elements, which are connected at nodal points. Then, the displacements of these nodal points are marked as the generalised coordinates of the structure, and express the deflection of the complete structure by means of assumed displacement functions. Basically, the complications of developing admissible functions for a complex model over the entire domain (globally) can be avoided by developing the admissible functions for smaller domains (locally). Therefore, in FEM, the partial differential equations of motion are transformed into second-order differential equations called interpolation functions, which are functions of displacements, velocities and accelerations of the FEM coordinates. The interpolation functions can be evaluated in closed form, which eliminates any integration errors and giving very accurate results.

The characteristic advantages and disadvantages of these discretisation models are summarised in Table 4.2. The best fitting models will be selected based on the requirements and system characteristics stated in the coming section.

Analysis of Modelling Techniques

There are a number of challenges associated with modelling a flexible multibody spacecraft. An adequate model of a FMS is a high-order one, due to the large number of flexible modes with minimal or no damping. Moreover, elastic frequencies are small and closely packed, with unknown

frequencies and mode shapes (Levine, 1999). Further, based on the requirements of this research, a trade-off can be done with four desirable characteristics:

- *Accuracy of model*: The model should give a good approximation of physical effects of flexibility to an extent such that its influence on the attitude dynamics and control can be studied effectively. The global modes model seems to be a very attractive option, because it gives simple yet accurate models for high degree of freedom systems. However, for this research, the system has a complex multibody structure, which would require extensive assumptions for simplification. Moreover, the model does not show good accuracy for systems with variable mass and geometry. Correspondingly, Rayleigh Ritz can become less accurate with the wrong choice of admissible functions, which become very difficult to choose for a FMS with a mixed rigid and flexible configuration. Then, LPM being an approximation of where the deformation can happen (due to an assumed lumped mass distribution) will perform inferior to FEM for the same discretisation. However, if sufficient amount of discretisation is applied, accuracy can be improved.

- *Computational load*: The simulation model should not be heavy on the computer, in terms of time as well as the processor capability. However, that also depends on the quality of algorithm written by the programmer. The global modes method can be simulated in numerical computing software, like MATLAB. However, the Envisat-chaser model consists of many elements with different mass and stiffness. All these elements will have to be modelled separately with different boundary conditions and shape functions, making the model mathematically and computationally demanding. Also, since the spacecraft is rotating about all three axes, the model can become very complex. Therefore, this model is not the preferred option for the study. Rayleigh Ritz is also not the most suited approach for this study, because the system has a number of flexible attachments, making it impossible to define admissible functions at substructure level due to dependency of boundary conditions. Even if all boundary conditions are defined individually, the computation becomes very expensive with no guarantee of good accuracy. Both LPM and FEM can be simulated on any commercial FEM software. The computational load can be controlled by reducing the amount of discretisation. However, there is a certain trade-off between computation load and accuracy in these formulations.

- *Compatibility with floating reference frame*: The model should be adaptable in the chosen frame of reference selected in Section 4.1. Since the floating reference frame was selected, this adds a constraint on the model that it should be reducible. The most suited models for this reference frame will be FEM and LPM, because they consist of finite mass and stiffness matrices as a result of the finite discretisation. It is also possible to reduce the Rayleigh Ritz formulation, however, it requires the additional step of numerically computing the important modes, unlike FEM and LPM. This can be easily reduced using most FEM software. Lastly, the global modes method is a more suited formulation for the inertial reference frame, since it is always defined with respect to an inertial frame. Moreover, as there is no discretisation and the model cannot be solved in a closed form (infinite series), this model cannot be reduced.

- *Ease of simulation*: The chosen model should be easy to program and simulate in the available software. Again, FEM and LPM models can be easily simulated using any commercial FEM software. This allows simulation of very complex multibody configurations with asymmetric mass and geometric distribution. The global modes and Rayleigh Ritz method can only be simulated numerically (coded in MATLAB, C++ and so on) and do not have dedicated software. Therefore, again the finite discretisation methods are preferred.

On summarising the properties of every model in Table 4.2, and weighing them against the parameters chosen for the trade off, two models selected for the research are the lumped parameter method

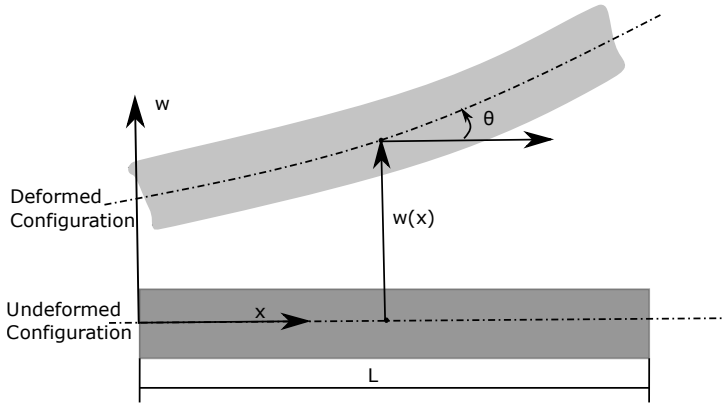

Figure 4.5: Beam in an undeformed and deformed configuration

and the finite element method. The FE model being the more accurate of the two will be used to model the flexible elements in this thesis. Further, FE models produce mass and stiffness matrices, which can be easily reduced using the modal reduction techniques that will be discussed in Section 4.3.3. Since most solar panels are axially stiff, they can be modelled as beam elements for simplicity. This also eliminates the need to consider complex inertial forces like Centrigual stiffening as it will be explained in Section 4.3.2. Therefore, in the next section, the generalised EOM for a beam will be derived using a FE model.

4.2.3. Generalised Equations of Motion using FEM for a beam

As stated before, the FE modelling is a numerical technique in which a continuous flexible structure, is divided into small but finite substructures known as elements, which are interconnected at nodes. In this way, an infinite DOF system can be modeled using a set of elements having a finite number of degrees of freedom. By choosing the size of the element to be small enough, the deformation within the finite element can be approximated using low-order polynomials (as compared to a continuous system).

Consider a beam element (single element of a discretised FE model) of length L, as shown in Figure 4.5. Let the beam element on deformation have a transverse displacement $w(x)$ and nodal rotation θ. For beams, the displacement field can be approximated using a cubic polynomial of the form:

$$w(x) = \alpha_1 + \alpha_2 x + \alpha_3 x^2 + \alpha_4 x^3, \qquad 0 \leq x \leq L \tag{4.11}$$

The cubic polynomial function should be chosen such that it is differentiable at least twice. This is to ensure that the chosen trial function is admissible. Now, Equation (4.11) can be written in the form:

$$w(x) = \begin{pmatrix} 1 & x & x^2 & x^3 \end{pmatrix} \begin{pmatrix} \alpha_1 \\ \alpha_2 \\ \alpha_3 \\ \alpha_4 \end{pmatrix} \tag{4.12}$$

The vector for nodal degrees of freedom of this element at the two end nodes i and j can be written as:

$$\boldsymbol{\delta_e} = \begin{pmatrix} w_i \\ \theta_i \\ w_j \\ \theta_j \end{pmatrix} \tag{4.13}$$

where the nodal rotations can be defined using the slope:

$$\theta = \frac{\partial w}{\partial x} \tag{4.14}$$

On differentiating and substituting Equation (4.12), the nodal DOF vector can be written as:

$$\boldsymbol{\delta_e} = \begin{pmatrix} w_i \\ \theta_i \\ w_j \\ \theta_j \end{pmatrix} = [\bar{\boldsymbol{A}}] \begin{pmatrix} \alpha_1 \\ \alpha_2 \\ \alpha_3 \\ \alpha_4 \end{pmatrix} \tag{4.15}$$

where $[\bar{\boldsymbol{A}}]$ is a function of x. On rearranging, the above equation can be written as:

$$\boldsymbol{w(x)} = \begin{pmatrix} 1 & x & x^2 & x^3 \end{pmatrix} [\bar{A}] \begin{pmatrix} w_i \\ \theta_i \\ w_j \\ \theta_j \end{pmatrix} \tag{4.16}$$

which can be written with a simplified notation:

$$\boldsymbol{w(x)} = \left\{\boldsymbol{N(x)}\right\} \boldsymbol{\delta_e} \tag{4.17}$$

Here, the vector $\left\{\boldsymbol{N(x)}\right\}$ is the vector of interpolation functions for beam elements, known as shape functions. This vector is used to express the displacement of any point in terms of the nodal DOF.

Using the Lagrange's principle to derive the generalised EOM, first the potential energy and the kinetic energy should be derived. The potential energy can be found using the expression for strain energy given by:

$$U = \frac{1}{2} EI \int_0^L \left(\frac{\partial^2 \boldsymbol{w}}{\partial \boldsymbol{x}^2}\right)^2 d\boldsymbol{x} \tag{4.18}$$

where E is the Modulus of Elasticity (which depends on the material), and I is the area moment of inertia (which depends on geometry). Substituting for shape function, the equation becomes,

$$U = \frac{1}{2} \delta_e^T EI \int_0^L \left\{\boldsymbol{N_{xx}}\right\}^T \left\{\boldsymbol{N_{xx}}\right\} d\boldsymbol{x}\, \boldsymbol{\delta_e} \tag{4.19}$$

where

$$\left\{\boldsymbol{N_{xx}}\right\} = \left\{\frac{\partial^2 \boldsymbol{N(x)}}{\partial \boldsymbol{x}^2}\right\} \tag{4.20}$$

The potential energy can be further simplified to:

$$U = \frac{1}{2} \boldsymbol{\delta_e^T K_e \delta_e} \tag{4.21}$$

where $\boldsymbol{K_e}$ is the element stiffness matrix given by:

$$\boldsymbol{K_e} = EI \int_0^L \left\{\boldsymbol{N_{xx}}\right\}^T \left\{\boldsymbol{N_{xx}}\right\} d\boldsymbol{x} \tag{4.22}$$

The kinetic energy of the beam with density, ρ and cross-sectional area, A is given by:

$$T = \frac{1}{2} \rho A \int_0^L \dot{\boldsymbol{w}}^2 d\boldsymbol{x} \tag{4.23}$$

Again, inserting the shape function gives,

$$T = \frac{1}{2}\dot{\boldsymbol{\delta}}_{\boldsymbol{e}}{}^{T}\rho A\int_0^L \left\{\boldsymbol{N_x}\right\}^T \left\{\boldsymbol{N_x}\right\} d\boldsymbol{x}\dot{\boldsymbol{\delta}}_{\boldsymbol{e}} \tag{4.24}$$

which can be simplified to:

$$T = \frac{1}{2}\dot{\boldsymbol{\delta}}_{\boldsymbol{e}}{}^{\boldsymbol{T}}\boldsymbol{M_e}\dot{\boldsymbol{\delta}}_{\boldsymbol{e}} \tag{4.25}$$

Here, $\boldsymbol{M_e}$ is the element mass matrix, given by:

$$\boldsymbol{M_e} = \rho A\int_0^L \left\{\boldsymbol{N_x}\right\}^T \left\{\boldsymbol{N_x}\right\} d\boldsymbol{x} \tag{4.26}$$

On completing the Lagrangian formulation given by Equation (4.10), the final element equation of motion for free vibration becomes:

$$\boldsymbol{M_e}\ddot{\boldsymbol{\delta}}_{\boldsymbol{e}} + \boldsymbol{K_e}\boldsymbol{\delta_e} = \boldsymbol{0} \tag{4.27}$$

Upon assembly of elemental equations, the generalised equation for the whole system can be written as:

$$\boldsymbol{M}\ddot{\boldsymbol{\delta}} + \boldsymbol{K}\boldsymbol{\delta} = \boldsymbol{0} \tag{4.28}$$

If the damping term is included, an additional velocity term is added to the equation ($\boldsymbol{C}\dot{\boldsymbol{\delta}}$). Also, external forces can be accounted for by adding a term on the right hand side ($\boldsymbol{F}$). Then, Equation (4.28) becomes:

$$\boldsymbol{M}\ddot{\boldsymbol{\delta}} + \boldsymbol{C}\dot{\boldsymbol{\delta}} + \boldsymbol{K}\boldsymbol{\delta} = \boldsymbol{F} \tag{4.29}$$

Equation (4.29) is the generalised form of equation of motion for a beam. However, any body discretised using the FE model can always be represented in the same form and thus, Equation (4.29) will be referred to throughout the thesis as the generalised equation of motion. Further, also the procedure for derivation of the EOM remains the same for any configuration, with only the change in shape functions, energy expressions of potential and kinetic energy, and the DOF vector.

4.3. Floating Frame Formulation

In the floating frame formulation, the rigid multibody problem is extended to a flexible one, such that a large rigid body motion is defined with respect to the inertial frame, and the elastic properties are defined using a local coordinate frame called the floating reference frame. This frame being non-inertial needs special modelling techniques to formulate the internal and inertial forces. Further, it is imperative to discuss the coordinate system that will be used to define the rigid body motion of the floating frame itself.

One of the main advantages of the floating frame formulation is the possibility of reducing the model order without loss of accuracy, thereby reducing the computation time. To achieve this, different modal reduction techniques will be studied in Section 4.3.3. Then, to ensure the kinematics are defined correctly, constraints need to be applied to the EOMs to capture the motion of the interface points. Different possible techniques to apply thesis kinematic constraints will be discussed in Section 4.3.4. Additionally, the new formulation given by Ellenbroek and Schilder (2017), which combines the convenient constraint modelling techniques of inertial frame and corotational frame formulations without the need to introduce extra constraint equations, will be compared with the traditional constraint modelling methods in the same section.

4.3.1. Absolute and Relative Coordinates

In floating reference frames, the rigid body motion can be formulated using two kinds of coordinates - absolute generalised coordinates and relative generalised coordinates as shown in Figure

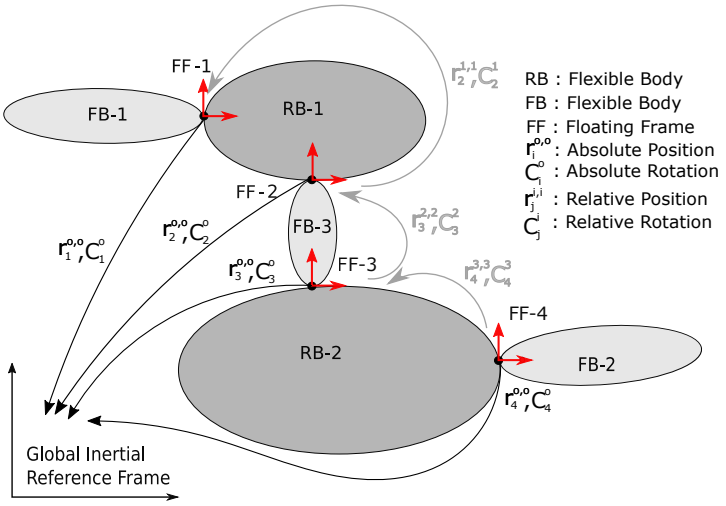

Figure 4.6: Relative and Absolute Coordinates

4.6. In *absolute coordinates*, the coordinates of each body are defined with respect to the global inertial frame. The dynamics of these bodies is coupled using constraints, which would link the rigid body dynamics with the flexible dynamics. However, by expressing the local elastic DOF at the interface of the bodies and defining the mean rigid body motion using the floating frame, these constraints can be simplified. According to Ellenbroek and Schilder (2017), this formulation gives the combined advantage of being able to enforce constraints without the use of Lagrange multipliers (as will be discussed in Section 4.3.4), and still have the possibility of modal reduction. Therefore, it is possible to define the motion of a flexible body in terms of motion of the interface points. In such a case, the body behaves like a superelement (Schilder et al., 2018), in which the displacement field of a finite element is described uniquely in terms of the displacement of its nodes. This will be discussed in further detail in the coming sections.

In the *relative coordinates* formulation, the coordinates of a body in a chain of bodies are expressed in terms of the coordinates of the previous body in the chain, and the DOFs of the joint connecting the two bodies. This proves to be advantageous for open loop systems for which the generalised coordinates are independent. Relative coordinates based techniques involve the additional step of computing each element in the chain. This can be inconvenient for variable structure FMS and the ones involving contact/impact, where the displacement of a node cannot be defined independently. The configuration of the system changes from a single rigid hub with an appendage to two rigid hubs with appendages connected by a flexible link in between. Therefore, it is not suitable in this research, where the structure/configuration changes with the phases, and constraint modelling becomes unavoidable and requires updates in every phase. In addition, for FMS involving closed loops, the solution depends on the choice of the location of the cut-joint constraint, which requires some skill and experience.

4.3.2. Nonlinear Inertia Effects

When the spacecraft or a component of the spacecraft is translating and/or rotating in a non-inertial frame, a number of nonlinear inertial forces, which couple the rigid and flexible elements like tangential, centrifugal and Coriolis force, are introduced. Another internal force associated with fast rotating objects caused by coupling of the axial and bending axis is the centrifugal stiffening. A brief description of all these nonlinear inertial coupling effects is given in this section.

Rigid-Flexible Coupling Terms

Since the floating frame is moving, flexible accelerations need to be introduced in addition to the linear mass terms. The nonlinear tangential, centrifugal and Coriolis terms couple the rigid body acceleration of the floating frame with the flexible accelerations defined relative to it. This accounts for the rigid body motion caused due to the vibration of the flexible appendages. A common technique and efficient way to model these terms with modal reduction, is by partitioning the generalised coordinates in the following way (Wasfy and Noor, 2003):

$$\boldsymbol{q} = \begin{pmatrix} q_T & q_\theta & q_f \end{pmatrix}^T \tag{4.30}$$

where subscripts T, θ, and f denote rigid body translation, rigid body rotation, and flexible coordinates, respectively. Because the time constant of translational motion is at least one order of magnitude larger than the one for rotational motion, for the duration of the analysis the position and velocity of the satellite can be assumed to be constant. This means that effectively translational and rotational motion are decoupled, and any perturbation dependent on orbital position is constant as well.

The corresponding mass matrix with coupling terms can be written as:

$$\boldsymbol{M} = \begin{bmatrix} \boldsymbol{M_{TT}} & \boldsymbol{M_{T\theta}} & \boldsymbol{M_{Tf}} \\ \boldsymbol{M_{\theta T}} & \boldsymbol{M_{\theta\theta}} & \boldsymbol{M_{\theta f}} \\ \boldsymbol{M_{fT}} & \boldsymbol{M_{f\theta}} & \boldsymbol{M_{ff}} \end{bmatrix} \tag{4.31}$$

Here, $\boldsymbol{M_{TT}}$ is a constant translational mass matrix representing the mass of entire body, $\boldsymbol{M_{ff}}$ represents the mass of the flexible elements, which is a constant finite element mass matrix, and $\boldsymbol{M_{\theta\theta}}$ represents the rotary inertia matrix, which can be assumed constant if the deformations are small, and time varying if the deformations are large. For this research, the deformations in the flexible panels can be considered small and the inertia tensor can be assumed to be constant. $\boldsymbol{M_{f\theta}}$, $\boldsymbol{M_{\theta T}}$ and $\boldsymbol{M_{Tf}}$ vary with time and represent the coupling between flexible body motion, rigid body translation and rigid body rotation. The matrix is symmetric and the off diagonal coupling terms are equal. Nonetheless, terms involving coupling between rigid and flexible motion can be either derived through inertia shape integrals, details of which can be found in Shabana (2013), or using dedicated reduction models (like Craig-Bampton), which have added advantages as will be discussed in Section 4.3.3.

The Coriolis and centrifugal inertial terms can be added as quadratic velocity terms in the equations of motion as a function of generalised coordinates, which is a typical formulation used in multibody systems (Shabana, 2013), using the equation:

$$\boldsymbol{F_c} = \dot{\boldsymbol{M}}\dot{\boldsymbol{q}} + \frac{\mathbf{1}}{\mathbf{2}}\frac{\partial(\dot{\boldsymbol{q}}^{\boldsymbol{T}}\boldsymbol{M}\dot{\boldsymbol{q}})}{\partial \boldsymbol{q}} \tag{4.32}$$

where $\dot{\boldsymbol{M}}\dot{\boldsymbol{q}}$ represents the Coriolis force vector and $\frac{\partial(\dot{\boldsymbol{q}}^{\boldsymbol{T}}\boldsymbol{M}\dot{\boldsymbol{q}})}{\partial \boldsymbol{q}}$ represents the centrifugal force vector. Being higher order velocity terms associated with generalised coordinates, these forces are a function of internal elastic deformation with respect to the interface points. Since elastic deformation is assumed to be small, these terms should not have a significant effect on the dynamics. Some benchmark problems simulated by Schilder et al. (2018) show that ignoring these fictitious forces for small deformations still lead to accurate results. Therefore, for this study, the effect of Coriolis and centrifugal terms will be ignored.

Centrifugal stiffening

Also known as dynamic stiffening, centrifugal stiffening is an inertial effect that acts along the axis of rotation of the body causing an axial stress that increases the bending stiffness. Hence, this effect is the result of coupling between the axial and bending deformations. When a rotating body

is connected to another body, this effect will also occur at the root of the joint, because of transfer of inter-body forces (Wasfy and Noor, 2003). However, this effect also depends on the way the flexible link is modelled. For instance, if a classical Euler-Bernoulli beam model is considered as the flexible appendage, the bending deformation will be decoupled from the axial deformation and the dynamic stiffening is neglected. This is because the axial deformation is neglected in an Euler-Bernoulli beam, which is a reasonable assumption for appendages with high axial stiffness. On the contrary, this is not true when the appendage is modelled as a plate or a Timoshenko beam. In the FE formulation, this effect is captured in the nonlinear part of the stiffness matrix, which accounts for the nonlinear inertial coupling between axial and bending stiffness. The system stiffness matrix appears to be of form:

$$\boldsymbol{K} = \begin{bmatrix} 0 & 0 & 0 \\ 0 & 0 & 0 \\ 0 & 0 & \boldsymbol{K_L} + \boldsymbol{K_{NL}} \end{bmatrix} \tag{4.33}$$

where $\boldsymbol{K_L}$ is the constant linear stiffness matrix and $\boldsymbol{K_{NL}}$ contains the nonlinear time varying terms, which include centrifugal stiffening term in addition to any other coupling terms linking axial and bending stiffness. For this research, the deformations are assumed to be small, but the angular velocity is large. The solar panels can be assumed to have a high axial stiffness, which is a common assumption for space structures (Wasfy and Noor, 2003). Therefore, the effect of centrifugal stiffening will be negligible, and the nonlinear terms from the stiffness matrix can be eliminated.

4.3.3. Modal Reduction

In most FMS applications, it is possible to truncate the modal expansion, such that only the significant modes are taken into account (Ellenbroek and Schilder, 2017). This is because, the high frequency modes carry little energy and have negligible contribution to the dynamics of the complete system. According to Wasfy and Noor (2003), by reducing the modes, the computation speed can be improved twofold. This reduces the number of EOM to be solved and therefore, facilitates the use of large integration steps. Modal reduction leads to effective reduction in computation time, only if the mass and stiffness matrices are constant and not a function of time and/or generalised coordinates. When these terms are constant, the reduction can be performed at once, in the beginning of the simulation. Otherwise, the modal reduction needs to be performed at every time step, which defeats the purpose of reducing computation time. Thus, structures with large deflections and high angular velocities are not suitable for modal reduction, because of the nonlinearity introduced in the stiffness matrix due to centrifugal stiffening. But as discussed in the previous section, this internal force can be ignored for the current research.

Before the modal reduction process is discussed, the term "*interface points*" should be understood in further detail. In general, the forces act on the entire body, however, the boundary conditions and constraints need to be applied at the interaction points between any two bodies, whether rigid or flexible, to ensure proper coupling. To perform reduction of an FE model and to account for the constraints, an interface point is introduced at physical boundaries, like joints and connections. The generalised coordinates for reduced modes are defined with respect to these interaction points, and the vibrations are represented as a sum of important modes.

The mode shapes can be reduced using two different techniques - a dedicated theoretical modal reduction technique or using experimental data. Since it is not possible to experimentally test the vibration modes for the e.deorbit mission, the theoretical techniques will be discussed in further detail. However, a number of questions need to be answered during the modal reduction process. How to decide which mode shapes are important? Which subsystem should be included while computing the natural frequency? Is it reasonable to model the appendage as a simple fixed free beam? To answer these questions, different modelling techniques will be explored. The model order reduc-

tion can be divided into three commonly used techniques: Static (Guyan), hybrid (Craig-Bampton) and manual modal reduction.

Static (Guyan) reduction

The static reduction, also known as Guyan reduction, works on a master-slave principle. For a system with N degrees of freedom, the m that are dominating, are called master DOF, and the s that are eliminated, are called slave DOF. The component modes are computed with the assumption that there are no inertial forces involved. This makes the method more suitable for stiffness reduction only, because of the inertial coupling terms involved in the mass matrix, which are not preserved. In other words, the reduction technique is suitable for static problems, but for dynamic problems, the approximations become extreme. Furthermore, the eigenvalues obtained for the reduced system are always higher than those of the original system. This results in a decrease of quality of eigenvalue approximation as the mode number increases. Therefore, this method will not be discussed in further detail.

Hybrid (Craig-Bampton) reduction

This hybrid reduction technique combines the static reduction with dynamic boundary conditions. Depending on how the boundary conditions are applied, they can be further classified into different methods. The most commonly used hybrid reduction method is the Craig-Bampton method, in which the system's dynamic behaviour is defined using two types of information (Geradin and Cardona, 2001):

- *Static Boundary Modes:* Obtained using Guyan or static reduction, by assuming a unit displacement at each boundary DOF.
- *Dynamic Boundary Modes:* A reduced set of eigenmodes for a clamped beam boundary condition (in this case), obtained from the FEM or lumped discretised model.

Let $\boldsymbol{x_b}$ represent the boundary DOF and $\boldsymbol{x_i}$ represent the internal DOF of the subsystem. Then, the system of equations defining the dynamics of the system can be written as:

$$\begin{bmatrix} \boldsymbol{M_{bb}} & \boldsymbol{M_{bi}} \\ \boldsymbol{M_{ib}} & \boldsymbol{M_{ii}} \end{bmatrix} \begin{pmatrix} \ddot{\boldsymbol{x}}_b \\ \ddot{\boldsymbol{x}}_i \end{pmatrix} + \begin{bmatrix} \boldsymbol{K_{bb}} & \boldsymbol{K_{bi}} \\ \boldsymbol{K_{ib}} & \boldsymbol{K_{ii}} \end{bmatrix} \begin{pmatrix} \boldsymbol{x_b} \\ \boldsymbol{x_i} \end{pmatrix} = \begin{pmatrix} \boldsymbol{f_b} \\ \boldsymbol{0} \end{pmatrix} + \begin{pmatrix} \boldsymbol{g_b} \\ \boldsymbol{0} \end{pmatrix} \tag{4.34}$$

where $\boldsymbol{g_b}$ represents the reaction force with other substructures and $\boldsymbol{f_b}$ represents the external forces. To obtain the dynamic boundary modes of vibration, the boundary degree of freedom should be constrained ($\boldsymbol{x_b} = \boldsymbol{0}$). This reduced Equation (4.34) to:

$$\boldsymbol{M_{ii}}\ddot{\boldsymbol{x}}_i + \boldsymbol{K_{ii}}\boldsymbol{x_i} = \boldsymbol{0} \tag{4.35}$$

Equation (4.35) becomes the eigenvalue problem, which can be solved using:

$$(\boldsymbol{K_{ii}} - \omega_i^2 \boldsymbol{M_{ii}})\boldsymbol{\phi_i} = 0 \tag{4.36}$$

where $\boldsymbol{\omega_i}$ is the angular velocity for the respective fixed interface mode shape in $\boldsymbol{\phi_i}$. Now the static boundary modes need to be computed. This constrained mode is obtained using the static deformation shape at one of the boundaries, when a unit displacement is applied and all but one DOF is constrained. This is done for every interface point (with appropriate boundary conditions) and DOF until a set of constraint modes is obtained. For instance, in a 3D situation, an interface point on a fixed-fixed beam will have three DOF as shown in Figure 4.7, which results in a total of six constraint modes for two interface points. Now, recalling the second equation from Equation (4.34):

$$\boldsymbol{M_{ib}}\ddot{\boldsymbol{x}}_b + \boldsymbol{M_{ii}}\ddot{\boldsymbol{x}}_i + \boldsymbol{K_{ib}}\boldsymbol{x_b} + \boldsymbol{K_{ii}}\boldsymbol{x_i} = \boldsymbol{0} \tag{4.37}$$

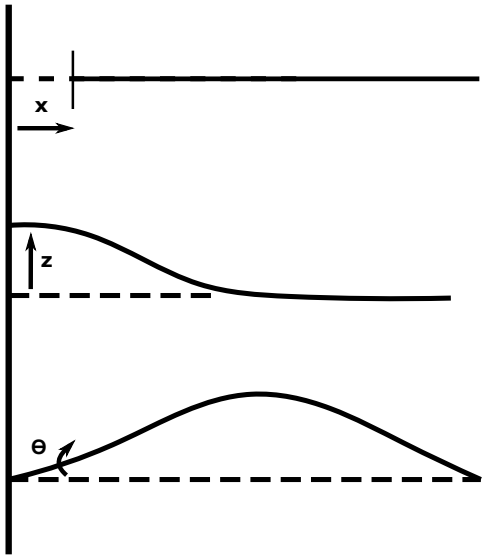

Figure 4.7: Interface point with 3 DOF on one end of a fixed-fixed beam

As stated in the previous section, the static part is obtained by neglecting the inertia forces. This condenses the equation to:

$$\boldsymbol{x_{i,stat}} = -\boldsymbol{K_{ii}^{-1}}\boldsymbol{K_{ib}}\boldsymbol{x_b} \tag{4.38}$$

The term $-\boldsymbol{K_{ii}^{-1}}\boldsymbol{K_{ib}}$ forms the static condensation matrix, which allows the static response of the internal degree of freedom $\boldsymbol{x_i}$ to be represented as a function of unit displacement of the boundary DOF ($\boldsymbol{x_b}$), as:

$$\begin{pmatrix} \boldsymbol{x_b} \\ \boldsymbol{x_i} \end{pmatrix} = \boldsymbol{\psi_c}\boldsymbol{x_b} = \begin{bmatrix} \boldsymbol{I} \\ -\boldsymbol{K_{ii}^{-1}}\boldsymbol{K_{ib}} \end{bmatrix} \boldsymbol{x_b} \tag{4.39}$$

Here, the matrix $\boldsymbol{\psi_c}$ denotes the constraint modes. Combining both constraint modes $\boldsymbol{\psi_c}$ and fixed-interface vibration modes $\boldsymbol{\phi_i}$, the internal DOF can be finally written as:

$$\boldsymbol{x_i} = \boldsymbol{\psi_c}\boldsymbol{x_b} + \boldsymbol{\phi_i}\boldsymbol{q_i} \tag{4.40}$$

where $\boldsymbol{q_i}$ denotes the generalised coordinate or DOF associated with the subsystem. Using this, the final reduction matrix $\boldsymbol{R_{CB}}$ can be written as:

$$\begin{pmatrix} \boldsymbol{x_b} \\ \boldsymbol{x_i} \end{pmatrix} = \begin{pmatrix} \boldsymbol{x_b} \\ \boldsymbol{\psi_c}\boldsymbol{x_b} + \boldsymbol{\phi_i}\boldsymbol{q_i} \end{pmatrix} = \begin{bmatrix} \boldsymbol{I} & \boldsymbol{0} \\ \boldsymbol{\psi_c} & \boldsymbol{\phi_i} \end{bmatrix} \begin{pmatrix} \boldsymbol{x_b} \\ \boldsymbol{q_i} \end{pmatrix} = \boldsymbol{R_{CB}} \begin{pmatrix} \boldsymbol{x_b} \\ \boldsymbol{q_i} \end{pmatrix} \tag{4.41}$$

The reduction matrix ($\boldsymbol{R_{CB}}$) can be used to obtain the reduced mass and stiffness matrices, given by:

$$\tilde{\boldsymbol{K}} = \boldsymbol{R_{CB}^T}\boldsymbol{K}\boldsymbol{R_{CB}} \qquad \tilde{\boldsymbol{M}} = \boldsymbol{R_{CB}^T}\boldsymbol{M}\boldsymbol{R_{CB}} \tag{4.42}$$

A detailed representation of these matrices is given by:

$$\tilde{\boldsymbol{K}} = \begin{bmatrix} \tilde{\boldsymbol{K}}_{bb} & \mathbf{0} \\ \mathbf{0} & \boldsymbol{\omega}_i^2 \end{bmatrix} \tag{4.43}$$

$$\tilde{\boldsymbol{K}}_{bb} = \boldsymbol{K}_{bb} - \boldsymbol{K}_{bi}\boldsymbol{K}_{ii}^{-1}\boldsymbol{K}_{ib} \tag{4.44}$$

$$\tilde{\boldsymbol{M}} = \begin{bmatrix} \tilde{\boldsymbol{M}}_{bb} & \tilde{\boldsymbol{M}}_{bq} \\ \tilde{\boldsymbol{M}}_{qb} & \boldsymbol{I} \end{bmatrix} \tag{4.45}$$

$$\tilde{\boldsymbol{M}}_{bb} = \boldsymbol{M}_{bb} - \boldsymbol{M}_{bi}\boldsymbol{K}_{ii}^{-1}\boldsymbol{K}_{ib} - \boldsymbol{K}_{bi}\boldsymbol{K}_{ii}^{-1}\boldsymbol{M}_{ib} + \boldsymbol{K}_{bi}\boldsymbol{K}_{ii}^{-1}\boldsymbol{M}_{ii}\boldsymbol{K}_{ii}^{-1}\boldsymbol{K}_{ib} \tag{4.46}$$

$$\tilde{\boldsymbol{M}}_{qb} = \boldsymbol{\phi}_m^T(\boldsymbol{M}_{ib} - \boldsymbol{M}_{ii}\boldsymbol{K}_{ii}^{-1}\boldsymbol{K}_{ib}) = \tilde{\boldsymbol{M}}_{bq}^T \tag{4.47}$$

There are a number of advantages of Craig-Bampton reduction. The formulation ensures that both mass and stiffness is taken into account (unlike Guyan reduction). It also takes into account the different boundary conditions at the interface, which confirms the coupling between the rigid and flexible bodies, and accountability of any external forces. For the floating frame formulation, this method is very compatible, because the local interface coordinates can be treated as generalised coordinates corresponding to Craig-Bampton reduction. Therefore, the static modes can be easily used to define the local elastic displacement (Schilder et al., 2018). A disadvantage of this method is that if the interface point is changed, the whole analysis needs to be performed again. However, the reduction is very flexible and the output can be easily assembled by the FE software. The fact that all DOF are captured in the formulation eliminates the need for added constraints, and the mass and stiffness matrices can be used directly in the EOM, which is an added advantage.

Manual reduction

It is also possible to manually filter out the important frequencies and condense the mass and stiffness matrices by simply eliminating the terms of lower importance. The effective modal mass provides a scale for judging the contribution of a vibration mode. Modes with relatively high effective masses can be readily excited by base excitation. In other words, they have a larger contribution to the total energy of the system. On the other hand, modes with low effective masses do not cause a significant change to the energy. Consider a multi-body system for which the mode shapes are being analysed used FEM. Now another question arises about how many modes should be included in the analysis? This number should be such that the total effective modal mass, which is the sum of all effective masses of the model, is at least 90% of the actual mass (Irvine, 2013). The EOM discretised through FEM (assuming no damping) will result in the form:

$$\boldsymbol{M}\ddot{\boldsymbol{x}} + \boldsymbol{K}\boldsymbol{x} = \boldsymbol{F} \tag{4.48}$$

where $\boldsymbol{M}$ is the mass matrix, $\boldsymbol{K}$ is the stiffness matrix, $\ddot{\boldsymbol{x}}$ is the acceleration vector, $\boldsymbol{x}$ is the displacement vector, and $\boldsymbol{F}$ is the forcing function or base excitation function. The solution to Equation (4.48) will be given by the eigenvalues and eigenvectors, which represent the natural frequency of the modes. The generalised mass matrix (or normalised mass matrix) is given by:

$$\hat{\boldsymbol{m}} = \boldsymbol{\phi}^T\boldsymbol{M}\boldsymbol{\phi} \tag{4.49}$$

where $\boldsymbol{\phi}$ is the eigenvector. Then, let us consider an influence vector $\bar{\boldsymbol{r}}$, which represents the displacements of the masses resulting from static application of a unit ground displacement. Then, the modal participation factor, which indicates the relative contribution of the system modes to the system states for every eigenmode, can be computed using:

$$\boldsymbol{\Gamma}_i = \frac{\bar{\boldsymbol{L}}}{\hat{\boldsymbol{m}}_{ii}} \tag{4.50}$$

where $\boldsymbol{\Gamma_i}$ is the modal participation factor, and, $\bar{\boldsymbol{L}}$ is a coefficient vector given by:

$$\bar{\boldsymbol{L}} = \boldsymbol{\phi}^T \boldsymbol{M} \bar{\boldsymbol{r}} \tag{4.51}$$

Finally, the effective modal mass matrix, $\boldsymbol{m_{eff,i}}$ for each mode i is given by:

$$\boldsymbol{m_{eff,i}} = \frac{\bar{\boldsymbol{L}}^2}{\hat{\boldsymbol{m}}_{ii}} \tag{4.52}$$

Thus, any mode that contributes strongly has a higher effective modal mass and has to be included in a reduced-order model, while a mode with low effective modal mass can be eliminated for a multibody system. Typically, the first two modes have the major contribution to the total effective mass.

It is also possible to compute the effective masses and modal participation factors of the modes using an FEM software. The simplicity of the technique makes it a viable option for this research. This method is independent of flexibility and inertia characteristics, which makes it applicable to a wide range of problems. The accuracy of the method improves with increased discretisation of the FEM model. However, there are a number of disadvantages, which cannot be overlooked. The model still requires constraints to account for kinematic and geometric conditions of the multibody system at the interface points. Further, the rigid flexible coupling and other inertial forces are not taken into account. This requires extra computation of these terms through shape integrals. Also, there is a large probability of error, because not all DOF may be captured in the formulation. In conclusion, this method is suitable for rigid body systems where there are no inertial forces involved, but for FMS, it can prove to be cumbersome and risky, because of the additional computations required.

Therefore, for this research, Craig-Bampton seems to be the ideal reduction model and will be consequently used to derive the EOM.

4.3.4. Constraints

Modelling of joints and interfaces is a crucial aspect in computational methodology for flexible multibody systems. Constraints define the kinematics of these joints by linking the motion between two participating bodies. It can be any condition that reduces the DOF of a mechanical system. In analytical dynamics, the basic classification of constraints include two types: holonomic and non-holonomic constraints. *Holonomic constraints* are implicit functions of generalised coordinates and time, and are represented by $\boldsymbol{\phi}(\boldsymbol{q}, t) = \boldsymbol{0}$. *Non-holonomic constraints* are implicit functions of generalised coordinates, velocities and time, and are represented by $\boldsymbol{\phi}(\boldsymbol{q}, \dot{\boldsymbol{q}}, t) = \boldsymbol{0}$. Some common methods used for incorporating these constraints in EOM are:

1. *Lagrange multiplier method*: In this method, the constraint reaction force can be added to the global EOM in the form:

$$\boldsymbol{F_R} = \frac{\partial \boldsymbol{\phi}^T}{\partial \boldsymbol{q}} \boldsymbol{\lambda} \tag{4.53}$$

   where $\frac{\partial \boldsymbol{\phi}^T}{\partial \boldsymbol{q}}$ is the Jacobian constraint matrix and $\boldsymbol{\lambda}$ is the vector of Lagrange multipliers. This method has proved to be of high accuracy in terms of satisfying constraints. Addtionally, both holonomic and non-holonomic constraints can be modelled systematically for arbitrary configurations of an FMS. The main disadvantage is that it adds to the number of unknowns in the set of coordinates to be solved, which results in an increase in computation time. Also, according to Wasfy and Noor (2003), zero terms are introduced on the diagonal of the equivalent nonlinear stiffness matrix, which considerably increase its stiffness and required solution effort. Therefore, some alternative methods, which do not have these shortcomings will be discussed.

2. *Penalty method:* To eliminate the drawback of the increased number of unknowns introduced by Lagrange multipliers, the penalty method can be used instead. In this method, the reaction forces are written in the form:

$$F_R = \frac{\partial \boldsymbol{\phi}^T}{\partial \boldsymbol{q}} \boldsymbol{\alpha} \frac{\partial \boldsymbol{\phi}}{\partial \boldsymbol{q}} \tag{4.54}$$

   where $\boldsymbol{\alpha}$ is a diagonal matrix that contains the penalty factors for each constraint equation. The method has the disadvantage that the constraint equations are not satisfied exactly (less accurate than Lagrange multipliers) and that large values of $\boldsymbol{\alpha}$ lead to stiff equations. The method is more suitable for a system with components connected by incompatible nodal interfaces. In such a case, penalty springs are introduced to represent the shape and stiffness of joints. However, this method is also not suitable due to its poor accuracy in satisfying constraints.

3. *Augmented Lagrangian method:* The augmented Lagrange method combines both the Lagrange multiplier and the penalty methods to diminish the shortcomings of both methods. By introducing a penalty spring whose stiffness is comparable to the stiffness of other components of the FMS, the number of iterations and effort required to solve the system of unknowns can be reduced. This is because the constraints are appropriately scaled to generate system matrices of the same order of magnitude. The constraint is satisfied with the good accuracy of Lagrange multipliers at the end of each solution time step. However, it is difficult to derive a convenient formulation for the choice of penalty parameter. It can also lead to some inaccuracies due to approximation of second derivatives of the constraint in the formulation (Gill et al., 1986).

4. *Absolute coordinate formulation:* Ellenbroek and Schilder (2017) proposed a new technique to directly enforce constraints without the use of Lagrange multipliers. This is achieved by expressing the floating frame coordinates and the local elastic deformation in the flexible body directly in terms of the interface coordinates, which is defined with respect to the inertial frame. By demanding that the elastic body has no deformation at the location of the floating frame, the reduced modes can be used to eliminate the floating frame coordinates and then, the local elastic deformation is defined directly in terms of the motion of the interface points. This couples the bodies directly without the need to enforce constraints because now the nodes of the two connecting bodies can be defined as equal (as it is done in the inertial frame formulation). This new method eliminates the shortcomings of constraint handling, which is a great advantage when it comes to modelling of multiple interface points (as in the stacked configuration). In combination with the Craig-Bampton modes, the EOM can be significantly condensed without loss in accuracy. Therefore, this method will be adapted for the research and will be discussed in further detail for the derivation of kinematic equations.

4.4. Equations of Motion

Having discussed the different aspects involved in the floating frame formulation, the kinematic and dynamic EOM will be formulated. The EOM will be formulated in absolute coordinates, with the dynamic equations reduced using Craig-Bampton reduction. The equations will also include inertial coupling terms between rigid-flexible systems, but the quadratic velocity terms including Coriolis and centrifugal forces will not be accounted for in the formulation (for simplicity). The constraints will be directly incorporated in the formulation without the use of Lagrange multipliers or penalty function, as a result of the new formulation approach using absolute coordinates (Ellenbroek and Schilder, 2017).

To derive the complete equations of motion, first some fundamental properties need to be derived. Therefore, the kinematics of a material point on a flexible body with respect to a floating

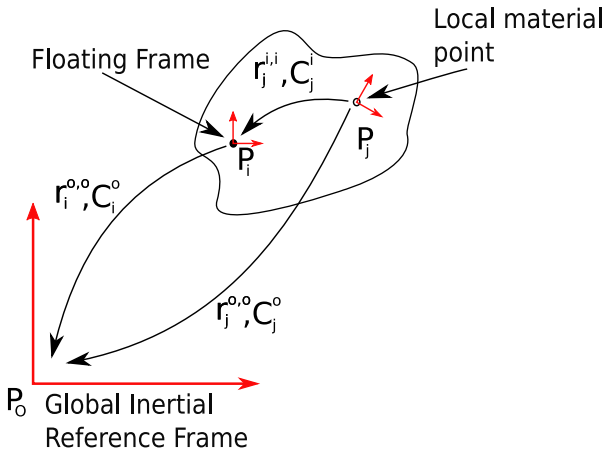

Figure 4.8: Position of material point P_j with respect to inertial frame at point P_o using floating frame at point P_i

frame will be derived in Section 4.4.1. This will result in an expression for relative velocity of elastic deformation of a material point in the floating frame, in terms of absolute velocity difference between the floating frame and the material point. Then, a relation is established between the local elastic velocities and the absolute velocities at the interface points in Section 4.4.2. Here, the placement of the interface points and floating frame for the system configuration of this research is also discussed. The floating frame is then removed from the kinematic description through relevant transformation matrices, which are derived in Section 4.4.3. The final EOM in terms of absolute coordinates are derived in Section 4.4.4, followed by a discussion on the method used to solve it in Section 4.4.5. It should be noted that the following derivation has been adapted for the current configuration from Ellenbroek and Schilder (2017).

4.4.1. Kinematics of a Material Point on a Flexible Body using the Floating Frame Formulation

Before defining the kinematics of a multi-body system consisting of both rigid and flexible elements, it is foremost to understand how the kinematics of a flexible body in which the position of one point with respect to the other changes with time.

Figure 4.8 shows a flexible body with two material points P_i and P_j. A floating frame is placed with P_i at the origin and the absolute position is defined with respect to the inertial frame (with origin at P_o) using the position vector $\boldsymbol{r_i^{o,o}}$ and the rotation (or transformation) matrix $\boldsymbol{C_i^o}$. Note that the notation superscript "A,B" on the position or velocity vectors (*e.g.*, $\boldsymbol{r_i^{A,B}}$) indicates the position of point "P_i" defined in frame A, relative to the frame at B. Also, for the rotation matrix, the subscript A and superscript B indicates a transformation from frame A to frame B. Similarly, the position of material point P_j is defined with respect to the floating frame P_i using the position vector, $\boldsymbol{r_j^{i,i}}$ and the rotation matrix, $\boldsymbol{C_j^i}$. Therefore, the rotation matrix from the local frame at P_j to the inertial frame at P_o can be given using:

$$\boldsymbol{C_j^o} = \boldsymbol{C_i^o C_j^i} \tag{4.55}$$

Also, the position vector of P_j can be transformed into absolute coordinates using:

$$\boldsymbol{r_j^{o,o}} = \boldsymbol{r_i^{o,o}} + \boldsymbol{C_i^o r_j^{i,i}} \tag{4.56}$$

By taking the time derivative, the absolute linear velocity for material point P_j can be obtained as:

$$\boldsymbol{\dot{r}_j^{o,o}} = \boldsymbol{\dot{r}_i^{o,o}} + \boldsymbol{\dot{C}_i^o r_j^{i,i}} + \boldsymbol{C_i^o \dot{r}_j^{i,i}} \tag{4.57}$$

But previously, in Equation (3.30), it was derived that the time derivative of the rotation matrix is the product of a skew symmetric matrix and the rotation matrix itself. Therefore, using $\dot{\boldsymbol{C}}_{\boldsymbol{i}}^{\boldsymbol{o}} = \tilde{\boldsymbol{\omega}}_{\boldsymbol{i}}^{\boldsymbol{o,o}} \boldsymbol{C}_{\boldsymbol{i}}^{\boldsymbol{o}}$, the equation can be written as:

$$\dot{\boldsymbol{r}}_{\boldsymbol{j}}^{\boldsymbol{o,o}} = \dot{\boldsymbol{r}}_{\boldsymbol{i}}^{\boldsymbol{o,o}} + \tilde{\boldsymbol{\omega}}_{\boldsymbol{i}}^{\boldsymbol{o,o}} \boldsymbol{C}_{\boldsymbol{i}}^{\boldsymbol{o}} \boldsymbol{r}_{\boldsymbol{j}}^{\boldsymbol{i,i}} + \boldsymbol{C}_{\boldsymbol{i}}^{\boldsymbol{o}} \dot{\boldsymbol{r}}_{\boldsymbol{j}}^{\boldsymbol{i,i}} \tag{4.58}$$

Using the properties of skew-symmetric matrix, transformation and orthogonal matrices (see Appendix A), the equation can be simplified to:

$$\begin{aligned}
\dot{\boldsymbol{r}}_{\boldsymbol{j}}^{\boldsymbol{o,o}} =& \dot{\boldsymbol{r}}_{\boldsymbol{i}}^{\boldsymbol{o,o}} + \tilde{\boldsymbol{\omega}}_{\boldsymbol{i}}^{\boldsymbol{o,o}} \boldsymbol{r}_{\boldsymbol{j}}^{\boldsymbol{o,i}} + \boldsymbol{C}_{\boldsymbol{i}}^{\boldsymbol{o}} \dot{\boldsymbol{r}}_{\boldsymbol{j}}^{\boldsymbol{i,i}} \\
=& \dot{\boldsymbol{r}}_{\boldsymbol{i}}^{\boldsymbol{o,o}} - \tilde{\boldsymbol{r}}_{\boldsymbol{j}}^{\boldsymbol{o,i}} \boldsymbol{\omega}_{\boldsymbol{i}}^{\boldsymbol{o,o}} + \boldsymbol{C}_{\boldsymbol{i}}^{\boldsymbol{o}} \dot{\boldsymbol{r}}_{\boldsymbol{j}}^{\boldsymbol{i,i}} \\
=& \dot{\boldsymbol{r}}_{\boldsymbol{i}}^{\boldsymbol{o,o}} - \boldsymbol{C}_{\boldsymbol{i}}^{\boldsymbol{o}} \boldsymbol{C}_{\boldsymbol{o}}^{\boldsymbol{i}} (\boldsymbol{r}_{\boldsymbol{j}}^{\boldsymbol{o,i}} \times \boldsymbol{\omega}_{\boldsymbol{i}}^{\boldsymbol{o,o}}) + \boldsymbol{C}_{\boldsymbol{i}}^{\boldsymbol{o}} \dot{\boldsymbol{r}}_{\boldsymbol{j}}^{\boldsymbol{i,i}} \\
=& \dot{\boldsymbol{r}}_{\boldsymbol{i}}^{\boldsymbol{o,o}} - \boldsymbol{C}_{\boldsymbol{i}}^{\boldsymbol{o}} \det(\boldsymbol{C}_{\boldsymbol{o}}^{\boldsymbol{i}}) (\boldsymbol{C}_{\boldsymbol{o}}^{\boldsymbol{i}} \boldsymbol{r}_{\boldsymbol{j}}^{\boldsymbol{o,i}} \times \boldsymbol{C}_{\boldsymbol{o}}^{\boldsymbol{i}} \boldsymbol{\omega}_{\boldsymbol{i}}^{\boldsymbol{o,o}}) + \boldsymbol{C}_{\boldsymbol{i}}^{\boldsymbol{o}} \dot{\boldsymbol{r}}_{\boldsymbol{j}}^{\boldsymbol{i,i}} \\
=& \dot{\boldsymbol{r}}_{\boldsymbol{i}}^{\boldsymbol{o,o}} - \boldsymbol{C}_{\boldsymbol{i}}^{\boldsymbol{o}} \det(\boldsymbol{C}_{\boldsymbol{o}}^{\boldsymbol{i}}) \boldsymbol{C}_{\boldsymbol{o}}^{\boldsymbol{i}} (\boldsymbol{r}_{\boldsymbol{j}}^{\boldsymbol{i,i}} \times \boldsymbol{\omega}_{\boldsymbol{i}}^{\boldsymbol{i,o}}) + \boldsymbol{C}_{\boldsymbol{i}}^{\boldsymbol{o}} \dot{\boldsymbol{r}}_{\boldsymbol{j}}^{\boldsymbol{i,i}} \\
=& \dot{\boldsymbol{r}}_{\boldsymbol{i}}^{\boldsymbol{o,o}} - \boldsymbol{C}_{\boldsymbol{i}}^{\boldsymbol{o}} \det(\boldsymbol{C}_{\boldsymbol{o}}^{\boldsymbol{i}}) \tilde{\boldsymbol{r}}_{\boldsymbol{j}}^{\boldsymbol{i,i}} \boldsymbol{C}_{\boldsymbol{o}}^{\boldsymbol{i}} \boldsymbol{\omega}_{\boldsymbol{i}}^{\boldsymbol{i,o}} + \boldsymbol{C}_{\boldsymbol{i}}^{\boldsymbol{o}} \dot{\boldsymbol{r}}_{\boldsymbol{j}}^{\boldsymbol{i,i}}
\end{aligned} \tag{4.59}$$

Since a right-handed coordinate frame is used and the point P_i is a floating frame fixed to the body, the mirroring effect on rotation (a negative determinant) need not be considered. The mirroring effect can be explained by a simple example. Consider a 90° rotation around axis in a right-handed coordinate frame (1,1,1). This axis, when mirrored in the XY-plane, would give a -90° rotation around the left-handed coordinate frame (1,1,-1). Also, since the attitude representation by quaternions is used, the mirroring effect is naturally overlooked. Therefore, the determinant of the rotation matrix ($\det(\boldsymbol{C}_{\boldsymbol{o}}^{\boldsymbol{i}})$) always remains positive unity. The final equation can be written in the form:

$$\dot{\boldsymbol{r}}_{\boldsymbol{j}}^{\boldsymbol{o,o}} = \dot{\boldsymbol{r}}_{\boldsymbol{i}}^{\boldsymbol{o,o}} - \boldsymbol{C}_{\boldsymbol{i}}^{\boldsymbol{o}} \tilde{\boldsymbol{r}}_{\boldsymbol{j}}^{\boldsymbol{i,i}} \boldsymbol{C}_{\boldsymbol{o}}^{\boldsymbol{i}} \boldsymbol{\omega}_{\boldsymbol{i}}^{\boldsymbol{o,o}} + \boldsymbol{C}_{\boldsymbol{i}}^{\boldsymbol{o}} \dot{\boldsymbol{r}}_{\boldsymbol{j}}^{\boldsymbol{i,i}} \tag{4.60}$$

Now, the absolute angular velocity for the material point, P_j can be written similar to Equation (4.56), given by:

$$\boldsymbol{\omega}_{\boldsymbol{j}}^{\boldsymbol{o,o}} = \boldsymbol{\omega}_{\boldsymbol{i}}^{\boldsymbol{o,o}} + \boldsymbol{C}_{\boldsymbol{i}}^{\boldsymbol{o}} \boldsymbol{\omega}_{\boldsymbol{j}}^{\boldsymbol{i,i}} \tag{4.61}$$

Combining Equation (4.60) and (4.61), the velocity of a material can be defined using:

$$\begin{pmatrix} \dot{\boldsymbol{r}}_{\boldsymbol{j}}^{\boldsymbol{o,o}} \\ \boldsymbol{\omega}_{\boldsymbol{j}}^{\boldsymbol{o,o}} \end{pmatrix} = \begin{bmatrix} \boldsymbol{C}_{\boldsymbol{i}}^{\boldsymbol{o}} & \boldsymbol{0} \\ \boldsymbol{0} & \boldsymbol{C}_{\boldsymbol{i}}^{\boldsymbol{o}} \end{bmatrix} \begin{bmatrix} \boldsymbol{I} & -\tilde{\boldsymbol{r}}_{\boldsymbol{j}}^{\boldsymbol{i,i}} \\ \boldsymbol{0} & \boldsymbol{I} \end{bmatrix} \begin{bmatrix} \boldsymbol{C}_{\boldsymbol{o}}^{\boldsymbol{i}} & \boldsymbol{0} \\ \boldsymbol{0} & \boldsymbol{C}_{\boldsymbol{o}}^{\boldsymbol{i}} \end{bmatrix} \begin{pmatrix} \dot{\boldsymbol{r}}_{\boldsymbol{i}}^{\boldsymbol{o,o}} \\ \boldsymbol{\omega}_{\boldsymbol{i}}^{\boldsymbol{o,o}} \end{pmatrix} + \begin{bmatrix} \boldsymbol{C}_{\boldsymbol{i}}^{\boldsymbol{o}} & \boldsymbol{0} \\ \boldsymbol{0} & \boldsymbol{C}_{\boldsymbol{i}}^{\boldsymbol{o}} \end{bmatrix} \begin{pmatrix} \dot{\boldsymbol{r}}_{\boldsymbol{j}}^{\boldsymbol{i,i}} \\ \boldsymbol{\omega}_{\boldsymbol{j}}^{\boldsymbol{i,i}} \end{pmatrix} \tag{4.62}$$

A more condensed and convenient representation can be written as:

$$\boldsymbol{v}_{\boldsymbol{j}}^{\boldsymbol{o,o}} = [\boldsymbol{C}_{\boldsymbol{i}}^{\boldsymbol{o}}][-\tilde{\boldsymbol{r}}_{\boldsymbol{j}}^{\boldsymbol{i,i}}][\boldsymbol{C}_{\boldsymbol{o}}^{\boldsymbol{i}}] \boldsymbol{v}_{\boldsymbol{i}}^{\boldsymbol{o,o}} + [\boldsymbol{C}_{\boldsymbol{i}}^{\boldsymbol{o}}] \boldsymbol{v}_{\boldsymbol{j}}^{\boldsymbol{i,i}} \tag{4.63}$$

Here, the "[ ]" will be used as a simplified notation for the compound matrices. $\boldsymbol{v}_{\boldsymbol{j}}^{\boldsymbol{o,o}}$ and $\boldsymbol{v}_{\boldsymbol{j}}^{\boldsymbol{i,i}}$ are $(6N \times 1)$ vectors containing all variations of the absolute and local interface coordinates with time, respectively. $[\boldsymbol{C}_{\boldsymbol{o}}^{\boldsymbol{i}}]$ is a $(6N \times 6N)$ block diagonal matrix consisting of all rotation matrices associated with the respective interface points. Lastly, $[-\tilde{\boldsymbol{r}}_{\boldsymbol{j}}^{\boldsymbol{i,i}}]$ is the column-assembly of all (6×6) skew-symmetric matrices representing displacement and rotation of all interface points, when the system experiences rigid body motion in a certain direction with respect to the floating frame. Therefore, the local velocity of point P_j with respect to the floating frame can be reformulated to be:

$$\boldsymbol{v}_{\boldsymbol{j}}^{\boldsymbol{i,i}} = [\boldsymbol{C}_{\boldsymbol{o}}^{\boldsymbol{i}}] \boldsymbol{v}_{\boldsymbol{j}}^{\boldsymbol{o,o}} - [-\tilde{\boldsymbol{r}}_{\boldsymbol{j}}^{\boldsymbol{i,i}}][\boldsymbol{C}_{\boldsymbol{o}}^{\boldsymbol{i}}] \boldsymbol{v}_{\boldsymbol{i}}^{\boldsymbol{o,o}} \tag{4.64}$$

From the above equation, it can be concluded that the relative velocity of elastic deformation in a floating frame can be defined by the absolute velocity difference between the floating point and the material point. This principle will be used to define the local elastic velocities due to vibration of the flexible appendages with respect to the floating frame, which can be located at an interaction point or the rigid hub.

4.4.2. Relation between Local Elastic and Absolute Velocities at the Interface Point

Now that the kinematics of a material point is defined in absolute coordinates, a relationship should be established for transformation of local elastic velocities to the absolute formulation. Assuming that the elastic deformation of the flexible elements are small, the flexible body can be discretised into many linear finite elements called superelements, which can be used to define dynamics with respect to a floating frame at P_i with a constant mass matrix $\boldsymbol{M_i}$ and stiffness matrix $\boldsymbol{K_i}$. This can be achieved by establishing generalised coordinates $\boldsymbol{q^{j,j}}$ to represent the deformation using the modes obtained after Craig-Bampton reduction. This is applicable with an assumption that the deformation can be represented by a linear combination of selected modes (Ellenbroek and Schilder, 2017). The deformation will include the small elastic displacements, $\boldsymbol{u_j^{i,i}}$, and rotation of the interface points, $\boldsymbol{\theta_j^{i,i}}$. Therefore, the generalised coordinates can be written as:

$$\boldsymbol{q_j^{i,i}} = \begin{pmatrix} \boldsymbol{u_j^{i,i}} \\ \boldsymbol{\theta_j^{i,i}} \end{pmatrix} \tag{4.65}$$

The relative position of the interface point P_j with respect to floating reference frame at P_i fixed to the body will change due to the flexible parts. The local position vector $\boldsymbol{r_j^{i,i}}$ can be written as the sum of a fixed undeformed position and local elastic deformation:

$$\boldsymbol{r_j^{i,i}} = \boldsymbol{x_j^{i,i}} + \boldsymbol{u_j^{i,i}} \tag{4.66}$$

where $\boldsymbol{x_j^{i,i}}$ is the position vector of point P_j with respect to the floating frame on the undeformed body. Using the rotation matrix to write the position of points P_i and P_j in absolute coordinates, the elastic displacement is given by:

$$\boldsymbol{u_j^{i,i}} = \boldsymbol{r_j^{i,i}} - \boldsymbol{x_j^{i,i}} = \boldsymbol{C_o^i}(\boldsymbol{r_j^{o,o}} - \boldsymbol{r_i^{o,o}}) - \boldsymbol{x_j^{i,i}} \tag{4.67}$$

Since rotations cannot be expressed as proper vectors, the orientation after deformation cannot be simply expressed as the sum of the undeformed orientation and elastic rotation. Therefore, it is assumed that the undeformed orientation of a material point with respect to the local frame is always zero, *i.e.* the undeformed local rotation matrix becomes an identity matrix. So, the final local orientation of a material point after deformation can be described as a change in the rotation of the interface point $\boldsymbol{\theta_j^{i,i}}$. The validity of this assumption is derived in a detailed manner in Appendix B. This can be used to define a relation between the relative velocity of a material point and the generalised coordinates corresponding to the reduced modes:

$$\dot{\boldsymbol{q}}_{\boldsymbol{j}}^{\boldsymbol{i,i}} = \begin{pmatrix} \dot{\boldsymbol{\theta}}_{\boldsymbol{j}}^{\boldsymbol{i,i}} \\ \dot{\boldsymbol{u}}_{\boldsymbol{j}}^{\boldsymbol{i,i}} \end{pmatrix} \approx \begin{pmatrix} \boldsymbol{\omega_j^{i,i}} \\ \dot{\boldsymbol{u}}_{\boldsymbol{j}}^{\boldsymbol{i,i}} \end{pmatrix} = \boldsymbol{v_j^{i,i}} \tag{4.68}$$

Relating the above equation with Equation (4.64), gives the relation between relative velocity of material point with absolute velocities of the floating frame and the material point:

$$\dot{\boldsymbol{q}}_{\boldsymbol{j}}^{\boldsymbol{i,i}} = [\boldsymbol{C_o^i}]\boldsymbol{v_j^{o,o}} - [-\tilde{\boldsymbol{r}}_{\boldsymbol{j}}^{\boldsymbol{i,i}}][\boldsymbol{C_o^i}]\boldsymbol{v_i^{o,o}} \tag{4.69}$$

In general, the dynamic equations in floating frame formulation include absolute coordinates of floating frame and the relative coordinates of interface points with respect to the floating frame. However, by using Equation (4.69), the local elastic velocities or the need for relative coordinates can be eliminated by expressing both floating frame and interface points in absolute coordinates. This ensures coupling of the bodies without the need of constraints through Lagrange multipliers as discussed in Section 4.3.4.

Placement of interface and floating points

In this research, there are a number of multibody configurations. In the synchronisation phase, both Envisat and chaser consist of a rigid body and a flexible appendage. In the semi-connected phase, the two multibody systems are connected by a flexible link. Finally, in the stacked phase, the connection is considered rigid and the configuration can be considered to be one single rigid hub with two appendages located asymmetrically. The single satellites contain one interface point between the rigid hub and the solar panel. However, the semi-connected and stacked configuration will have multiple interaction points. In such a scenario, the floating frame should be able to represent the dynamics due to the elastic deformation at multiple interface points.

A smart choice of location is also important, because when using the Craig-Bampton modes with the floating frame formulation, the total degrees of freedom will consist of $6N$ DOF for N-interface points, and an additional 6 DOF for the rigid modes obtained from absolute floating frame coordinates. This creates an overlap, because the rigid body modes are counted twice. This can be avoided by ensuring that there is no deformation at the location of the floating frame and then evaluating the Craig Bampton modes at the location of the floating frame. This constraint can be numerically represented as:

$$[\boldsymbol{\phi}_{CB}^{i}]\,\dot{\boldsymbol{q}}_{i}^{i,i} = \mathbf{0} \tag{4.70}$$

where $[\boldsymbol{\phi}_{CB}^{i}]$ is the $(6\times 6N)$ matrix of Craig-Bampton modes evaluated at the local frame. Physically, this constraint indicates that the floating frame remains attached to the same material point in both deformed and undeformed configurations. This ensures that the rigid body modes are represented by the floating frame and only the elastic modes are taken into account from the Craig-Bampton reduction, thereby eliminating the non-unique modes. The CoM can be considered to be a point, which does not suffer from deformation, because the elastic deformation in the system is assumed to be very small. Additionally, by placing the floating frame at the CoM of the system, its coordinates can be easily represented in terms of absolute interface coordinates, eliminating it from the EOM and establishing constraints without the need for Lagrange multipliers. This also provides the EOM some consistency for all three phases. Therefore, for the rest of the research, the location of the floating frame will be assumed to be at the CoM of the system.

4.4.3. Elimination of the Floating Frame from the Kinematic Description

As stated in the previous section, the floating frame will be located at the CoM of the system and not at any interface point. To ensure uniqueness in the modes chosen, it is required to place the floating frame at a location with no deformation. This allows simplification of the complete multibody formulation to absolute coordinates of interface points.

Figure 4.9 shows a body with the floating frame located at P_i on the rigid hub, connected to two flexible appendages. The interface points P_j and P_k are placed at the connection points of these bodies, with their position defined with respect to the floating frame using generalised coordinates (with reduced degree of freedom), $\boldsymbol{q}_{j}^{i,i}$ and $\boldsymbol{q}_{k}^{i,i}$. The floating frame itself is defined with respect to the inertial frame with $\{\boldsymbol{r}_{i}^{o,o}, \boldsymbol{C}_{i}^{o}\}$. By eliminating the floating frame, the position of the interface coordinates is given by $\{\boldsymbol{r}_{j}^{o,o}, \boldsymbol{C}_{j}^{o}\}$ and $\{\boldsymbol{r}_{k}^{o,o}, \boldsymbol{C}_{k}^{o}\}$.

In a more general case containing N interface points, with P_i still representing a non-inertial point, where the floating frame is placed. The deformation ($\boldsymbol{q}_{i}^{i,i}$) of this point due to an arbitrary interface point, P_j can be represented by reduced modes related to the interface point, $\boldsymbol{\phi}_{j}^{i}$. The total elastic deformation of P_i due to all the interface points can then be given using superposition of all modes ($\boldsymbol{\phi}_{j}^{i}$) and the generalised coordinates ($\boldsymbol{q}_{i}^{i,i}$), given by:

$$\boldsymbol{q}_{i}^{i,i} = \sum_{j=1}^{N} \boldsymbol{\phi}_{j}^{i}\,\boldsymbol{q}_{j}^{i,i} \tag{4.71}$$

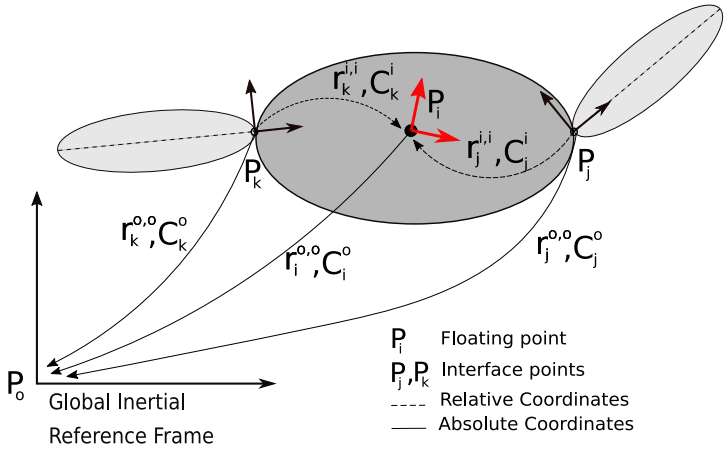

Figure 4.9: Relative and Absolute representation of interface points P_j and P_k

Due to the nonlinear relation between the relative and absolute position of the interface points, as well as floating frame (because the system changes with time), these constraints cannot be solved at position level (Ellenbroek and Schilder, 2017). Solving this at velocity level, however, is an option. Therefore, differentiating Equation (4.71), with $\dot{\boldsymbol{\phi}}_j^i = \mathbf{0}$, gives:

$$\dot{\boldsymbol{q}}_i^{i,i} = \sum_{j=1}^{N} \boldsymbol{\phi}_j^i \dot{\boldsymbol{q}}_j^{i,i} = \mathbf{0} \tag{4.72}$$

Substituting Equation (4.69), the equation becomes:

$$\dot{\boldsymbol{q}}_i^{i,i} = \sum_{j=1}^{N} \boldsymbol{\phi}_j^i ([\boldsymbol{C}_o^i]\boldsymbol{v}_j^{o,o} - [-\tilde{\boldsymbol{r}}_j^{i,i}][\boldsymbol{C}_o^i]\boldsymbol{v}_i^{o,o}) = \mathbf{0} \tag{4.73}$$

Rewriting this to give the relation between the velocity of floating frame and the absolute velocities of the interface points gives:

$$[\boldsymbol{Q}^i][\boldsymbol{C}_o^i]\boldsymbol{v}_i^{o,o} = \sum_{j=1}^{N} [\boldsymbol{\phi}_j^i][\boldsymbol{C}_o^i]\boldsymbol{v}_j^{o,o} \quad \text{where } [\boldsymbol{Q}^i] = \sum_{j=1}^{N} \boldsymbol{\phi}_j^i[-\tilde{\boldsymbol{r}}_j^{i,i}] = [\boldsymbol{\phi}_{CB}^i][\boldsymbol{\phi}_{rig}^i] \tag{4.74}$$

Here, $[\boldsymbol{Q}^i]$ is a (6×6) matrix representing the elastic deformation (due to the reduced modes) of the interface points. The matrix $[-\tilde{\boldsymbol{r}}_j^{i,i}]$ represents the 6 rigid body modes of the deformed body at the interface points relative to the floating frame at P_i. The summation can be represented as the linear combination of all Craig-Bampton modes. When the body is undeformed, the position vectors $\boldsymbol{r}_j^{i,i}$ will be equal to position vectors $\boldsymbol{x}_j^{i,i}$. As a result, $[\boldsymbol{Q}^i]$ becomes an identity matrix, and is therefore always invertible. Hence, the absolute velocity of the floating frame can be written as:

$$\boldsymbol{v}_i^{o,o} = [\boldsymbol{C}_i^o][\boldsymbol{Q}^i]^{-1} \sum_{k=1}^{N} \boldsymbol{\phi}_j^i [\boldsymbol{C}_o^i]\boldsymbol{v}_j^{o,o} \tag{4.75}$$

Writing Equation (4.75) with a more simplified notation:

$$\dot{\boldsymbol{q}}_i^{o,o} = \boldsymbol{v}_i^{o,o} = [\boldsymbol{C}_i^o][\boldsymbol{Z}_i][\bar{\boldsymbol{C}}_o^i]\boldsymbol{v}_j^{o,o} \tag{4.76}$$

where, $\boldsymbol{v}^{o,o}$ is a $(6N \times 1)$ vector containing the absolute velocities of all interface points, $[\bar{\boldsymbol{C}}_o^i]$ is a $(6N \times 6N)$ matrix containing an assembly of (6×6) rotation matrices, and lastly, $[\boldsymbol{Z}^i]$ is a $(6 \times 6N)$

transformation matrix, which defines the relation between the absolute motion of the interface coordinates and the absolute motion of the floating frame. These can be mathematically represented by:

$$\boldsymbol{v}^{o,o} = \begin{pmatrix} \boldsymbol{v}_1^{o,o} \\ \vdots \\ \boldsymbol{v}_N^{o,o} \end{pmatrix} \qquad [\bar{\boldsymbol{C}}_o^i] = \begin{bmatrix} [\boldsymbol{C}_o^i] & & \\ & \ddots & \\ & & [\boldsymbol{C}_o^i] \end{bmatrix} \tag{4.77}$$

$$[\boldsymbol{Z}^i] = [\boldsymbol{Q}^i]^{-1}[\boldsymbol{\phi}_{CB}^i] = [\boldsymbol{Q}^i]^{-1}\begin{pmatrix} \phi^1 & \cdots & \phi^N \end{pmatrix} \tag{4.78}$$

where the subscript "CB" in $\boldsymbol{\phi}_{CB}^i$ represents the reduced modes. Here, $[\boldsymbol{Z}^i]$ denotes the rigid body motion due to the motion of an interface point in floating frame at P_i. Recalling Equation (4.69) and adapting it for multiple interface points, the local velocity of the deformed body becomes:

$$\dot{\boldsymbol{q}}^{i,i} = \left[\bar{\boldsymbol{C}}_o^i\right]\boldsymbol{v}^{o,o} - \left[-\tilde{\boldsymbol{r}}^{i,i}\right]\left[\bar{\boldsymbol{C}}_o^i\right]\boldsymbol{v}_i^{o,o} \tag{4.79}$$

where the terms without a subscript represent the compound matrices containing the position and velocity of all interface points. Substituting $\boldsymbol{v}_i^{o,o}$ from Equation (4.76), the local velocity of the deformed body can be written in terms of absolute velocities of interface points, and is given by:

$$\dot{\boldsymbol{q}}^{i,i} = \left[\bar{\boldsymbol{C}}_o^i\right]\boldsymbol{v}^{o,o} - [\boldsymbol{\phi}_{rig}^i]\left[\boldsymbol{C}_o^i\right][\boldsymbol{C}_i^o][\boldsymbol{Z}^i][\bar{\boldsymbol{C}}_o^i]\boldsymbol{v}^{o,o} \tag{4.80}$$

Simplifying and writing in matrix form,

$$\dot{\boldsymbol{q}}^{i,i} = \begin{bmatrix} [\boldsymbol{\phi}_{rig}^i] & \boldsymbol{I} \end{bmatrix}\begin{bmatrix} -[\boldsymbol{Z}^i] \\ \boldsymbol{I} \end{bmatrix}[\bar{\boldsymbol{C}}_o^i]\boldsymbol{v}^{o,o} = [\boldsymbol{T}^i][\bar{\boldsymbol{C}}_o^i]\boldsymbol{v}^{o,o} \tag{4.81}$$

Here, $\dot{\boldsymbol{q}}^{i,i}$ represents a $6N \times 1$ column matrix containing the local velocities relative to the floating frame due to elastic deformation in the body, $[\boldsymbol{\phi}_{rig}^i]$ is a $6N \times 6N$ compound matrix containing the rigid body modes for all interface points given by:

$$\dot{\boldsymbol{q}}^{i,i} = \begin{pmatrix} \dot{\boldsymbol{q}}_1^{i,i} \\ \vdots \\ \dot{\boldsymbol{q}}_N^{i,i} \end{pmatrix}, \qquad [\boldsymbol{\phi}_{rig}^i] = \begin{pmatrix} -\tilde{\boldsymbol{r}}_1^{i,i} \\ \vdots \\ -\tilde{\boldsymbol{r}}_N^{i,i} \end{pmatrix} \tag{4.82}$$

Lastly, $[\boldsymbol{T}^i]$ is a $(6N \times 6N)$ transformation matrix which defines the relation between the absolute and local motion of the interface coordinates.

$$[\boldsymbol{T}^i] = \boldsymbol{I} - [\boldsymbol{\phi}_{rig}^i][\boldsymbol{Z}^i] \tag{4.83}$$

Here, $[\boldsymbol{T}^i]$ can be physically interpreted to remove the rigid body motion from the motion of an interface point, such that only the velocity of the elastic part remains (Dwarshuis, 2017). The two matrices $[\boldsymbol{Z}^i]$ and $[\boldsymbol{T}^i]$ are called the transformation matrices and the final velocity equation in terms of the transformation matrices is given by:

$$\begin{bmatrix} \dot{\boldsymbol{q}}_i^{o,o} \\ \dot{\boldsymbol{q}}^{i,i} \end{bmatrix} = \boldsymbol{A}\dot{\boldsymbol{q}}^{o,o}, \quad \text{where} \quad \boldsymbol{A} = \begin{bmatrix} [\boldsymbol{C}_i^o][\boldsymbol{Z}^i][\bar{\boldsymbol{C}}_o^i] \\ [\boldsymbol{T}^i][\bar{\boldsymbol{C}}_o^i] \end{bmatrix} \tag{4.84}$$

Therefore, Equation (4.84) allows the successful formulation of the dynamic equations of floating frame completely in terms of inertial coordinates. Together, Equations (4.76) and (4.84) define all degrees of freedom for the floating frame formulation in absolute interface coordinates.

4.4.4. Final Equations of Motion in Absolute Coordinates

The equations of motion can be derived using the principle of virtual work, as stated in Section 4.2. The equations can be divided into two parts, based on the standard floating frame formulation, wherein the DOF of the system are represented using the absolute floating frame coordinates ($\boldsymbol{q}_i^{o,o}$) and the local interface coordinates with respect to the floating frame ($\boldsymbol{q}_j^{i,i}$). The modes and respective mass and stiffness matrices for the local coordinates are chosen based on Craig-Bampton reduction. Therefore, the generalised equation of motion for a FMS can be written in the form:

$$\boldsymbol{M}\ddot{\boldsymbol{q}} + \boldsymbol{C}\dot{\boldsymbol{q}} + \boldsymbol{K}\boldsymbol{q} = \boldsymbol{Q} \tag{4.85}$$

Here, the $\boldsymbol{M}$ and $\boldsymbol{K}$ denote the global mass and stiffness matrices, $\boldsymbol{q}$ are the generalised coordinates of the floating frame and local frames of the system, $\boldsymbol{C}\dot{\boldsymbol{q}}$ includes the quadratic velocity inertia forces due to terms like damping, centrifugal and Coriolis forces, and lastly, $\boldsymbol{Q}$ includes the externally applied forces and moments like gravity gradient, control torques and so on. In a more elaborated floating frame formulation, the equation can be written as:

$$\begin{bmatrix} \boldsymbol{M}_{rr}^i & \boldsymbol{M}_{rf}^i \\ \boldsymbol{M}_{f,r}^i & \boldsymbol{M}_{ff}^i \end{bmatrix} \begin{pmatrix} \ddot{\boldsymbol{q}}_i^{o,o} \\ \ddot{\boldsymbol{q}}_j^{i,i} \end{pmatrix} + \begin{bmatrix} \boldsymbol{C}_{rr}^i & \boldsymbol{C}_{rf}^i \\ \boldsymbol{C}_{f,r}^i & \boldsymbol{C}_{ff}^i \end{bmatrix} \begin{pmatrix} \dot{\boldsymbol{q}}_i^{o,o} \\ \dot{\boldsymbol{q}}_j^{i,i} \end{pmatrix} + \begin{bmatrix} \boldsymbol{0} & \boldsymbol{0} \\ \boldsymbol{0} & \boldsymbol{K}_{ff}^i \end{bmatrix} \begin{pmatrix} \boldsymbol{0} \\ \boldsymbol{q}_j^{i,i} \end{pmatrix} = \begin{pmatrix} \sum \boldsymbol{F}_i^o \\ \boldsymbol{L}_j^i \end{pmatrix} \tag{4.86}$$

In the above equation, the subscript f indicates the flexible part and r indicates the rigid part. A coupling between rigid and flexible DOF is indicated by rf or fr. Also, it can be noted that the stiffness matrix only has a flexible part, because the rigid body does not induce any elastic forces. Vector $\sum \boldsymbol{F}_i^o$ is the sum of all external forces and moments in the floating frame with respect to the inertial frame. $\boldsymbol{L}_j^i$ gives the effect of an external force or moment on the mode shapes.

To transform the system from floating frame formulation to an absolute formulation, Equation (4.84) can be used. Rewriting:

$$\begin{bmatrix} \dot{\boldsymbol{q}}_i^{o,o} \\ \dot{\boldsymbol{q}}^{i,i} \end{bmatrix} = \boldsymbol{A}\dot{\boldsymbol{q}}^{o,o}, \quad \text{where} \quad \boldsymbol{A} = \begin{bmatrix} [\boldsymbol{C}_i^o][\boldsymbol{Z}^i][\bar{\boldsymbol{C}}_o^i] \\ [\boldsymbol{T}^i][\bar{\boldsymbol{C}}_o^i] \end{bmatrix} \tag{4.87}$$

To get the acceleration, these terms can be differentiated. This gives:

$$\begin{bmatrix} \ddot{\boldsymbol{q}}_i^{o,o} \\ \ddot{\boldsymbol{q}}^{i,i} \end{bmatrix} = \boldsymbol{A}\ddot{\boldsymbol{q}}^{o,o} + \dot{\boldsymbol{A}}\dot{\boldsymbol{q}}^{o,o} \tag{4.88}$$

Performing the transformation in Equation (4.85) by pre multiplying by $\boldsymbol{A}^T$ and post multiplying by $\boldsymbol{A}$, the equations of motion become:

$$\boldsymbol{A}^T\boldsymbol{M}\boldsymbol{A}\ddot{\boldsymbol{q}}^{o,o} + \boldsymbol{A}^T(\boldsymbol{M}\dot{\boldsymbol{A}} + \boldsymbol{C}\boldsymbol{A})\dot{\boldsymbol{q}}^{o,o} + \boldsymbol{A}^T\boldsymbol{K}\boldsymbol{q}^{i,i} = \boldsymbol{A}^T\boldsymbol{Q} \tag{4.89}$$

By making some simplifying assumptions (that will be listed below), the equations can be reduced to (Schilder et al., 2018):

$$[\bar{\boldsymbol{R}}_j^o][\boldsymbol{M}_{CB}][\bar{\boldsymbol{R}}_o^j]\ddot{\boldsymbol{q}}^{o,o} + [\bar{\boldsymbol{R}}_j^o][\boldsymbol{T}_i]^T[\boldsymbol{C}_{loc}]\dot{\boldsymbol{q}}^{o,o} + [\bar{\boldsymbol{R}}_j^o][\boldsymbol{T}_i]^T[\boldsymbol{K}_{CB}]\boldsymbol{q}^{i,i} = \boldsymbol{Q}^o \tag{4.90}$$

where $[\boldsymbol{M}_{CB}]$ and $[\boldsymbol{K}_{CB}]$ represent the local mass and stiffness matrices obtained from the FE model after performing Craig-Bampton reduction. While $[\boldsymbol{C}_{loc}]$ is the generalised velocity matrix (detailed description by van de Wetering (2018)). It can be noticed that the elastic forces are still expressed in terms of floating frames and not with respect to inertial frame. This is because the transformation to absolute coordinates cannot occur at position level. Comparing the terms of Equations (4.90) and (4.89), it can be seen that the stiffness matrix in both the equations are the same. To match the acceleration and velocity terms, it is assumed that (Dwarshuis, 2017),

1. The mass matrices are expressed in the undeformed configuration of the component (for the acceleration term).

2. The mass matrix is lumped (for the velocity term).

3. Each body is defined by one element at the interface points, which guarantees that the interface points chosen for this formulation and the floating frame formulation are the same (for velocity term).

A more detailed derivation of these assumptions can be found in Dwarshuis (2017). Therefore, Equation (4.90) represents the final EOM of a superelement, suitable for the simulation of flexible multibody dynamics.

4.4.5. Solving the Equations of Motion

Now that the EOM for the FMS have been formulated in absolute interface coordinates, the attention can be shifted to solving the problem. The mass and stiffness matrices can be obtained from the CB-reduction. As stated before, for this research all quadratic velocity inertia terms (like Coriolis and centrifugal stiffening forces) except damping will be ignored. Damping becomes an important source of energy dissipation to ensure stability of large space structures in the presence of unwanted vibrations. This is discussed in further detail in Section 6.3

As discussed before, this formulation is sensitive to the location of the floating frame. But because no relationship can be developed between the absolute interface coordinates at position level, the transformation is performed at velocity level. Therefore, numerical integration is required to solve the EOM for the position. An inherent problem associated with this numerical solution is a drift in the position of the floating frame due to numerical error. To check and correct this drift, Newton Raphson iterations are performed. The EOM are therefore not solved for large absolute positions of the interface points, but instead for small increments or changes in the coordinates within the time increment. The current floating frame coordinates are taken as an initial estimate for the next iteration. According to Schilder et al. (2018), only a few Newton Raphson iterations are required. Once sufficient accuracy is obtained for both absolute interface coordinates and absolute floating frame coordinates, the local interface coordinates and local elastic deformation can be determined consistently. Finally, the EOM can be solved again. Figure 4.10 summarises the important steps to derive the complete EOM for the multibody system in terms of absolute interface coordinates.

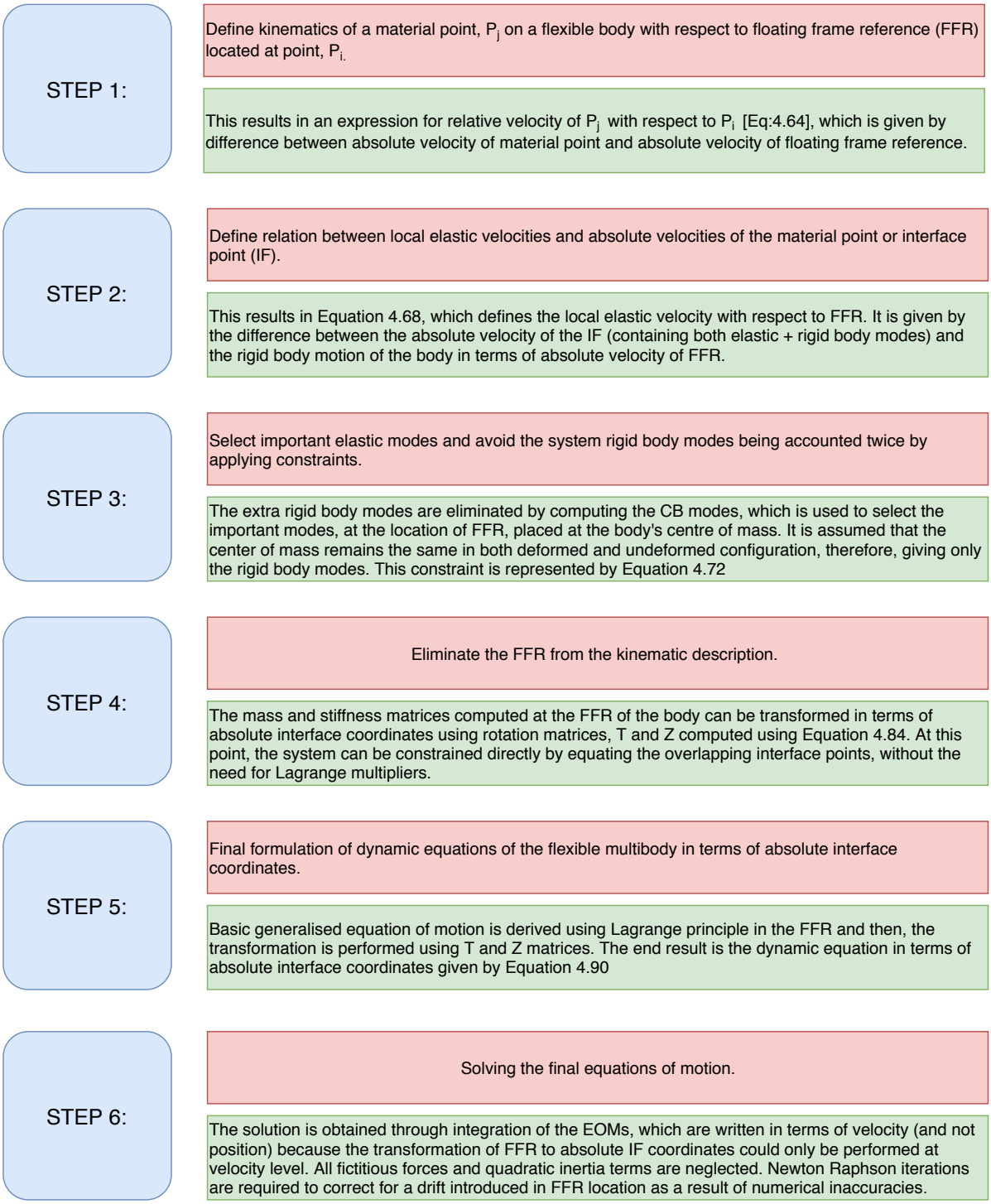

Figure 4.10: Summary of deriving FMD in terms of absolute interface coordinates

5

Simulator

In the previous chapters, the theory behind different aspects of the research has been introduced. In Chapter 3, the flight dynamics associated with rigid body motion was discussed. Further, the guidance and control design required for simulation were also set up in the same chapter. Based on the basic architecture of a GNC system, as shown in Figure 5.1, some benchmark simulations were made using the PD and INDI controllers. It was assumed that the plant behaves like a rigid body, and the sensors and actuators are ideal. In Chapter 4, the dynamics associated with a FMS were derived. Having established all this, it is now possible to build a simulator and replace the plant dynamics with the equations derived for the FMS. The final simulator would enable the analysis of dynamics and controllability characteristics of the system, when the flexible vibrations are treated as unpredictable disturbances.

In this chapter, the control simulator will be assembled with the dynamics from the new multi-body modelling technique based on absolute interface coordinates. First, the basic architecture of the complete system will be set up and the individual subsystems will be addressed in detail in Section 5.1. Second, in Section 5.2, the subsystem (plant) based on the new FMD methodology will be verified and validated to ensure proper working of the simulator.

5.1. Simulator Architecture

Figure 5.2 shows the architectural design for the simulator developed in this research (using the software MATLAB® as programming environment). In the figure, the basic architectural design of a

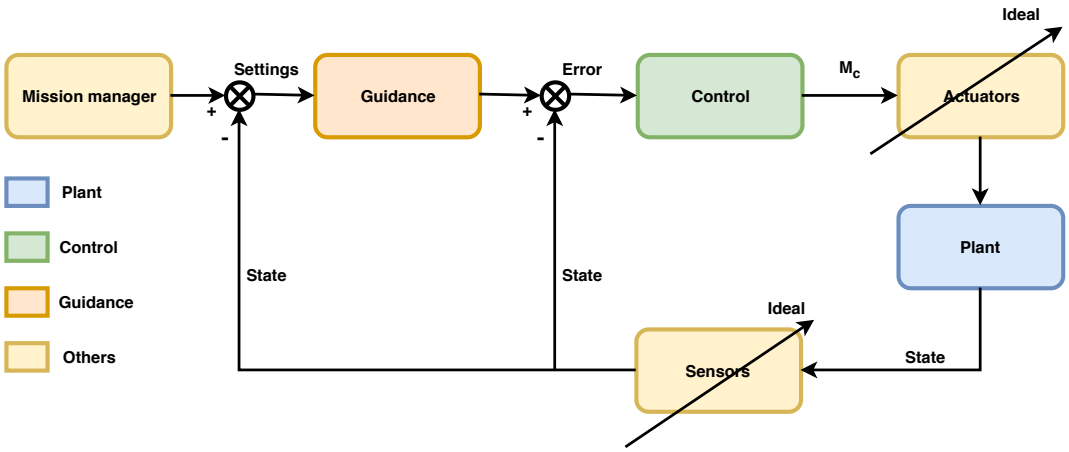

Figure 5.1: Basic GNC architecture

typical GNC system (refer Figure 5.1) has been maintained. The simulator shown in Figure 5.2, can be divided into four subsystems - *Mission manager, Guidance, Controller* and lastly, *Plant* or FMD. The *mission manager* first sends the settings to the *plant, guidance* and *controller* subsystems to initialise the simulation. Then, *guidance* outputs the commanded state, which is compared against the current state from the *plant*. The error between the states is then fed into the *controller*, which computes the required control moment for the *plant*. The *plant* uses the control input to propagate to a new state and feeds it back for error computation. The loop continues until the error between the commanded and current state is very small and the system has been stabilised. In the coming section, the subsystems will be discussed in further detail.

5.1.1. Mission Manager

The *mission manager* is responsible for initialisation of the other subsystems, as shown in Figure 5.2 in the yellow block. The *plant*, being configuration specific, needs to be initialised based on the phase of the mission. For instance, the synchronisation phase will include one solar panel and one lumped mass to balance the inertia. The connected phase will include two asymmetric solar panels with two lumped masses to account for inertia. The plant's initial state is also defined here. Further, the plant requires information about material properties, location of interface points and boundary conditions. Other settings indicating information about damping, simulation time, time step for integration and so on, is also included here. Similarly, the *guidance* is dependent on the mission phase as stated in Section 3.5, which is initialised by the *mission manager*. The controller selection between PD or INDI is also made in this subsystem, which passes on the respective gains to the controller. Lastly, the controller sampling frequency is set.

5.1.2. Guidance

Based on the current phase of the mission, the *guidance* subsystem first sets up the state vector containing angular velocity, quaternions and pseudo Euler angles. Note that three extra states of pseudo Euler angles were added due to the anomaly in the controller. Therefore, the state for the target during synchronisation phase, now becomes:

$$\boldsymbol{x_0} = (3.5,\ 3.5,\ 3.5,\ 0,\ 0,\ 0,\ 1,\ 0,\ 0,\ 0)^T \tag{5.1}$$

Similarly, the different operations in the connected phase, including detumbling only, detumbling and reorientation, and reorientation only, have ten states each in the vector, depending on the angular velocity case selected from Table 2.2. The subsystem also includes the rigid body EOM, which use the initial state vector to derive the commanded state at every time step at the controller sampling frequency. This commanded state is then used to compute the error in the plant state.

5.1.3. Controller

The *controller* block uses the error in state to compute the control moment using the control laws stated in Section 3.6. The controller output saturation is initially set to ± 50 Nm as proposed by Habets (2015). However, a sensitivity study will be performed for the selection of a better control limit. Because the main goal from the control perspective is to control the rotational motion of the satellite, a simple filter is applied in the block to check if the error in angular rates is above a certain threshold. If the condition is met, rate control is applied first to bring the error below the threshold after which the full state control is applied using a PD or INDI controller.

The subsystem contains a *Zero-Order Hold (ZOH)*, which is used to hold the same value of control moment for the chosen sampling time and mimics the working of an on-board digital controller. The ZOH discretises the control signal, as shown in Figure 5.3. By doing this, uninterrupted control is applied to the plant even when the time steps used in the plant are smaller. The accuracy of ZOH depends on the sampling frequency. The larger the frequency, the closer the signal gets to a continuous one.

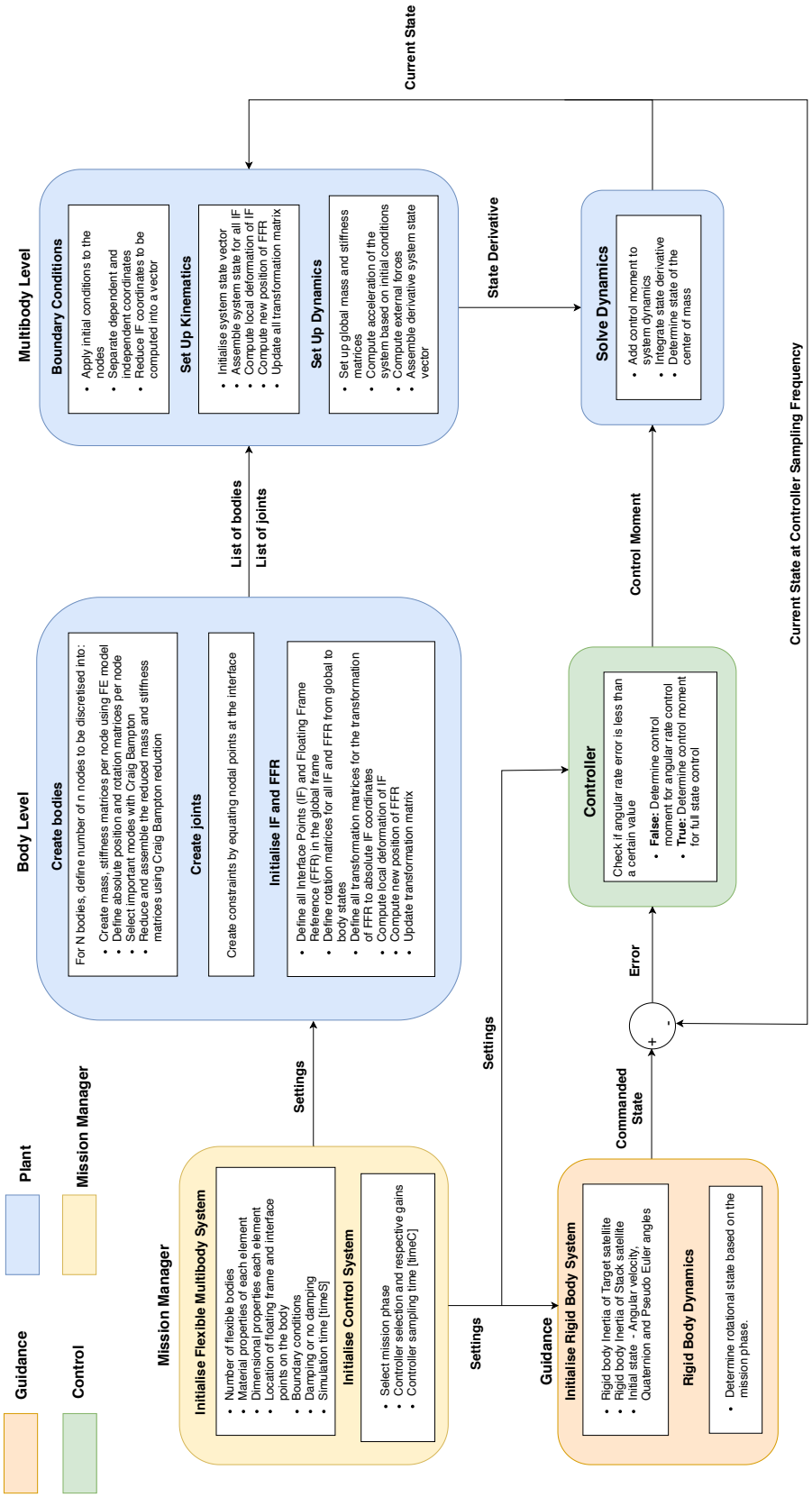

Figure 5.2: Simulator Architecture

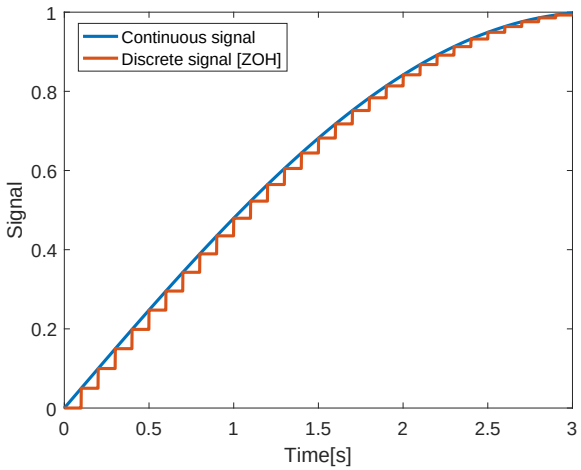

Figure 5.3: Discretised control using ZOH

5.1.4. Plant

The *plant* subsystem contains the FMD defined in Chapter 4, which is the main focus of the thesis. It is further divided into 3 levels - *Body, Multibody* and *Solve Dynamics*. Each block will be discussed in further detail.

Body Level

The information and settings about the multibody system configuration, which comes from the *mission manager*, are inputs to the *body* level. The initialisation of each flexible body (or element) in the multibody system occurs at this level. First, the mass and stiffness matrices are set up using principles of FEM. Then, the position and rotation matrices for each node are defined, based on the system geometry. Further, the Craig-Bampton (CB) reduction is applied to obtain the important modes of vibration, and also to reduce the mass and stiffness matrices per element.

Next, the constraints are set up at the end nodes of each element, which serve as the interface points for the multibody system. Then, the positions of interface points and Floating Frame Reference (FFR) are specified on each body. Several transformation matrices are defined to translate between interface points and global states, between interface points and FFR, and between global states and FFR. Lastly, the initial local deformation is computed based on the mode shapes and, subsequently, the position vectors for FFR and the transformation matrices are updated. The final output of the *body* level is a structure containing a list of bodies with mass, stiffness, modes, position and transformation matrices defined individually. Another output is a list of constraints on the joints between two adjacent bodies. In other words, it contains information about the overlapping nodes at the interface points. The *body* level block is called only once at the beginning of the simulation to initialise the *plant*.

Multibody Level

The *multibody* level uses the list of bodies and joints to assemble the structure into global mass and stiffness matrices. At this point, the boundary conditions are applied to the system to constrain any DOF identified in the original configuration. These constrained DOF will remain fixed throughout the simulation and can be excluded from the state vector for reducing computation time. Since there are a number of overlapping interface points at the joints, the states can be further reduced by considering only one set of dependent (overlapping) states. Note that the state vector initialisation for the *plant* only occurs once during the simulation. Once the complete state vector is set up, the kinematics and dynamics can be updated.

First, to update the kinematics, all the position vectors and transformation matrices are updated. With the new global mass and stiffness matrices, the acceleration is computed with the influence of external forces like control moments. If the settings specify addition of damping, it is also accounted for in this step. Second, the state derivative is assembled and sent to the *solve dynamics* level for integration.

Solve Dynamics Level

The *solve dynamics* level contains an integrator for the solution of state derivatives from the *multibody* level. The control moment from the *controller* is also an input to this block. At this level, the specifications for integration, including relative tolerance, absolute tolerance and step-size are specified. For this research, both relative and absolute tolerances for integration are set to 10^{-7} and an integration step-size of 10^{-3} s is used. The in-built MATLAB® ordinary differential equation (ODE) solvers like ode45, ode113 and ode15s did not perform well in terms of accuracy and computation time. Therefore, a high-order, variable-coefficient Ordinary Differential Equation solver called VODE is used. With fixed-leading-coefficient implementation, the integrator shows better performance both in terms of accuracy and computation time. It is suitable for solving both stiff and non-stiff differential equations. Originally part of the NetLib mathematical library (Brown et al., 1989), it is adapted to MATLAB® for the simulation.

After every integration step, the new state along with the control moments is fed back to the *multibody* block for computation of the derivative for the next time step. Since the controller sampling frequency (25 Hz) is an order smaller than the frequency used for integration of dynamics (1000 Hz), the same control moment is applied until the integration time step matches the control time step. This is achieved using the ZOH from the *controller* subsystem. The new state is fed back to the control loop for error computation at the control sampling frequency. Once the plant has been initialised, only the *multibody* and *solve dynamics* levels remain in the control loop. Hence, the integration continues till the final simulation time is reached.

Since the analysis of FMD is pivotal for this research, the *plant* must be verified and validated to ensure that the model is correct and fulfils its intended purpose. Therefore, in the coming section, the part of software defining the *plant* will be checked.

5.2. Verification and Validation

In Figure 5.2, the blocks highlighted in blue represent the structural dynamics of a flexible system, which acts as a plant for the control system. In this section, the working of the plant model will be validated using test cases given by Ellenbroek and Schilder (2017), originally adapted from Jonker (1988) (slider crank) and Cardona (2000) (spherical jointed beam). Additionally, the kinetic energy, elastic energy, total energy and internal/external work of the system will be examined to understand the dynamics better and to ensure that the total energy is balanced.

By law of conservation of energy, the total energy, E_{tot}, of the system (assuming no dissipation) should be conserved at every time step. This should account for elastic energy (or potential energy), E_{elas}, kinetic energy, E_{kin}, and external work of the system, W_{ext}. Therefore, the total energy of the system is calculated using

$$E_{tot}(t) = E_{elas}(t) + E_{kin}(t) + W_{ext}(t) \tag{5.2}$$

Further, the elastic energy should be calculated for each element at the body level (van de Wetering, 2018) at each time step. It is given by:

$$E^{b}_{elas}(t) = \frac{1}{2}\left(\boldsymbol{u^{i,i}}(t)\right)^{T} \boldsymbol{K_{CB}} \left(\boldsymbol{u^{i,i}}(t)\right) \tag{5.3}$$

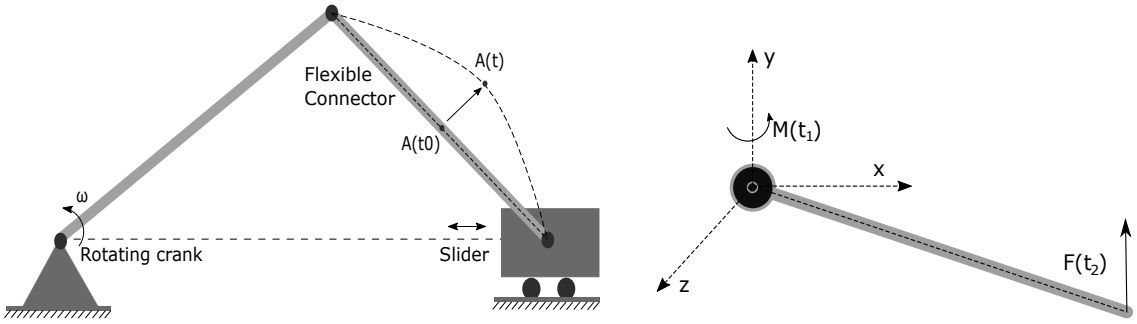

(a) Slider Crank (b) Beam with spherical joint

Figure 5.4: Test case for verification

where, $\boldsymbol{u^{i,i}(t)}$ is the elastic deformation of each element with respect to the floating frame at time t. Then, the total elastic energy is calculated at the multibody level (for N bodies) given by:

$$E_{elas}(t) = \sum_{b=1}^{N} E^{b}_{elas}(t) \tag{5.4}$$

The kinetic energy is also calculated at multibody level and is given by:

$$E_{kin}(t) = \frac{1}{2}\left(\boldsymbol{v^{o,o}}(t)\right)^{T} \boldsymbol{M_{sys}}\left(\boldsymbol{v^{o,o}}(t)\right) \tag{5.5}$$

where $\boldsymbol{v^{o,o}}(t)$ is the velocity of each element with respect to the inertial frame at time t. $\boldsymbol{M_{sys}}$ represents the system mass matrix. The total work is calculated as the sum of initial energy of the system and the work done by external forces $W(t)$, integrated over the total time, T, as shown below:

$$W(t) = \int_{t=0}^{T} \mathrm{d}W(t)\,\mathrm{d}t + E_{init} = \int_{t=0}^{T} (\boldsymbol{F^{o}}(t))^{T}\, \boldsymbol{v^{o,o}}(t)\,\mathrm{d}t + E_{init} \tag{5.6}$$

where $\boldsymbol{v^{o,o}}(t)$ is the velocity vector of the interface point with respect to inertial frame and $F^{o}(t)$ represents the external forces acting at the interface. Lastly, E_{init} represents the initial energy of the system, which comes from the prescribed motion to the system. For the validation, the first test cases is that of a 2D slider crank mechanism (Jonker, 1988). The configuration of the system is shown in Fig. 5.4(a). The system consists of a rigid crank, which is rotating with a constant prescribed angular velocity of 150 rad/s. The crank is then attached to a flexible connector of length 0.3 mm and a circular cross-sectional radius of 0.006 m. The connector is assumed to have material properties of steel, i.e., a Young's modulus of $2{\cdot}10^{11}$ N/m^2 and mass density of 7800 kg/m^3. The other end of the connector is then linked to a slider, which is allowed to move without friction. The mass of the slider is half of that of the connector. The constant angular velocity prescribed to the crank should induce a linear motion in the slider in the absence of flexibility. However, due to the elastic deformation of the connector, some perturbations can be observed in the slider motion. To model the dynamics of flexible connecter, it is divided into three nodes. The Point A in Fig. 5.4(a), which is halfway between the two end points serves as the location for the floating frame. The other two end points act as interface points. Figure 6.3 shows the displacement or mean motion of the midpoint throughout the simulation. On comparing with the reference dynamics obtained from the multibody software "Spacar" [1], the results from the new method show an exact match. Figure 5.5(b) shows the total energy of the system. It can be seen that the work done by the system is translated into kinetic energy and the total energy of the system remains zero and hence, conserved.

The second test case is that of a 3D beam constrained by a spherical joint at one end (Car-

[1] Private communication, Marcel Ellenbroek, 2018

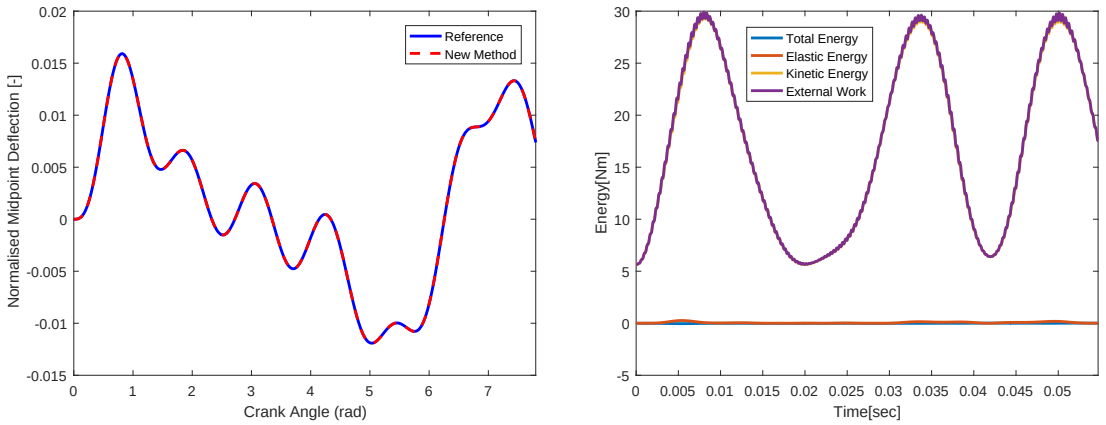

(a) System response (b) Energy balance

Figure 5.5: Slider Crank

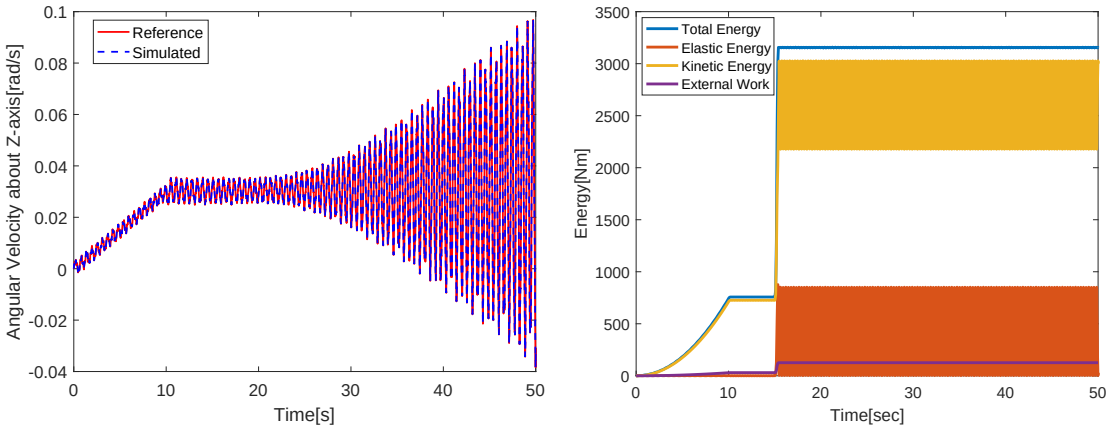

(a) System response (b) Energy balance

Figure 5.6: Beam with Spherical Joint

dona, 2000), as shown in Fig. 5.4(b). The beam is 141.42 mm long with a cross-section area of 9 mm^2 and an area moment of inertia of 6.75 mm^4. The mass density is $7.8{\cdot}10^{-3}$ kg/mm^{-3} and a Young's Modulus of $2.1{\cdot}10^6$ N/mm^2. The beam is given a torque of 200 Nmm about the vertical axis for the first 10.2 s and then, an impulsive force of 100 N is applied at the tip in vertical direction. The beam is modelled using two beam elements, and the resulting motion is completely in response to the external force and moment. The absolute angular velocity about the vertical axis is plotted against time. From Fig. 5.6(a), it can be seen that the new method matches the reference very closely. Further, in Fig. 5.6(b), a clear rise in the system's energy can be seen when the impulse is added to the system. The energy remains conserved at all time as the sum of the system's kinetic energy, elastic energy and external work. Both cases follow the Law of Energy Conservation, thus verifying the software based on the new formulation. The structural model of the satellite can now be modelled to fit the software design.

6

Structural Modelling of the Satellite

A typical multibody structure can be divided into flexible and rigid bodies. The displacement field consists of the flexible elastic deformation superimposed on the rigid body motion. To analyse the dynamics, the satellite configuration must be structurally modelled in a way, which is compatible with the new FMD methodology described in Chapter 4. The number of structural elements, material properties and mass properties also play a crucial role in defining the flexible dynamics accurately. A sensitivity study will be performed for the selection of these parameters for both e.deorbit and stacked configuration in Section 6.1.

Since the elastic vibrations are perturbations to the rigid body motion, the control moment is applied to the centre of mass of the configuration, which lies on the rigid hub due to its large mass. Therefore, it is crucial to also incorporate the rigid body dynamics in the flexible multibody system. In other words, the controller design for the flexible multibody system (minus the elastic perturbations) should be based on the same (satellite) properties as the rigid body. This also facilitates the comparative study of control-structure interaction of the flexible model as compared to the rigid model. The adaptation of rigid inertia properties to the flexible system will be discussed in Section 6.2.

Lastly, vibration of flexible appendages involve continuous exchange of kinetic and potential energy. In the absence of dissipative forces, the elastic energy of the system keeps increasing, and the system can become too dynamic for the controller to stabilise. Therefore, most flexible space structures have a small amount of active (controlled) or passive (structural) damping in the system, to improve the closed loop stability. Therefore, in Section 6.3, a simple yet effective way of including damping in weakly damped systems is explained.

6.1. Modelling of flexible elements

To define the position of the floating frame in the deformed configuration with respect to the interface points, it is advantageous to select a beam or plate configuration. This is because the deformation of any material point on these elements can be easily defined with respect to the local frame using established shape functions. Further, in the stacked configuration, the geometry becomes asymmetric. Choosing simple beam elements allows superposition of the oscillations caused by the dominant natural frequencies of the two asymmetric panels, and verification that the response of the system is as expected. Therefore, in this research, the flexible appendages will be represented using beam elements.

To model the dynamics of the solar panels as closely as possible using beams, a number of parameters must be carefully selected. These are:

- *Young's Modulus (E)*: This is a property of a material to resist deformation along an axis in

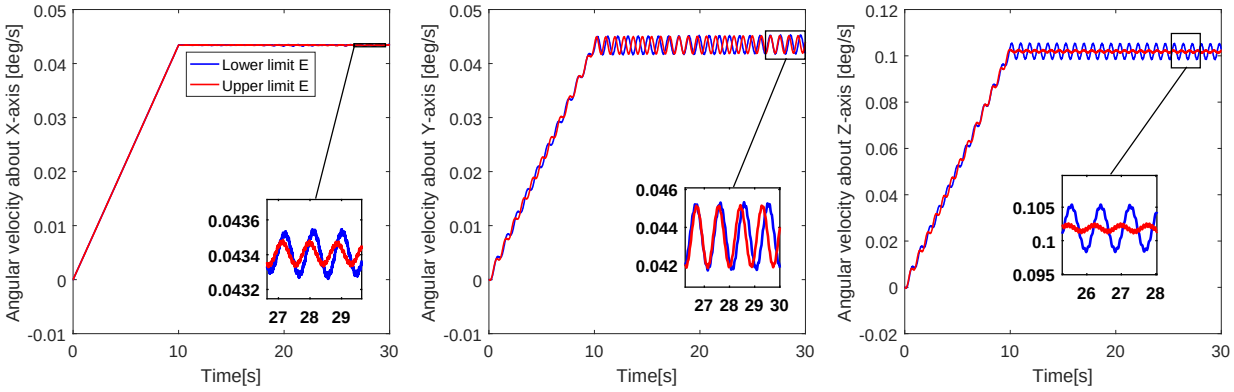

Figure 6.1: Angular velocity response for lower limit and upper limit of the solar panel

the presence of forces. A high value of Young's modulus corresponds to a material with high stiffness. According to Hassmann and Fenili (2007) and Fufa et al. (2010), for a 1 m long solar panel, the Young's modulus ranges between 4.8×10^{10} N/m^2 to 5.8×10^{10} N/m^2. To analyse the dynamics associated with these lower and upper limits, test simulations are made for a 2.9 m long beam constrained with a spherical joint on one end, initially in a stationary state (defining the configuration of the chaser). Figure 6.1 shows the response of the system to a 0.1 N force applied at the tip in X, Y and Z-directions for the first 10 s. The simulation time is 30 s with a timestep of 10^{-3} s. From the figure, it can be observed that the lower limit of E = 4.8×10^{10} N/m^2 suffers from larger amplitude vibrations compared to the upper limit of E = 5.8×10^{10} N/m^2 about all three axes. However, the mean value about which the oscillations occur, remains very similar. Since the test case for the research has a relatively high angular velocity and the modelling technique is new, a stiffer system (with smaller vibrations) is preferable for the preliminary analysis. Therefore, it will be assumed that a 1 m long beam element representing a solar panel has a Young's modulus of 5.8×10^{10} N/m^2.

- *Poisson's ratio*: It is assumed that the elastic deformations are small and there is no strain (or yield) in the system. For such a system, typically a Poisson's ratio of 0.3 is taken.

- *Length*: The length of a beam element also has an effect on the stiffness. The smaller the beam element, the higher will be its stiffness (for the same cross-sectional area and Young's modulus). However, the total length of the beam (or sum of beam elements) is taken equal to the length of the solar panel.

- *Cross-section area*: Modelling of beams demand that the cross-sectional area of the beam is negligible compared to the length. Therefore, a square cross-sectional area of dimensions 0.03×0.03 m is assumed. Here, the solar panel, which is a plate like structure, is modelled as a beam element, because its main load carrying direction is along the central longitudinal axis of the panel. The solar panel is connected to the rigid hub through a boom, which transfers the flexible motion of the panel to the rigid hub. Since the boom acts like a slender beam, the whole flexible appendage is modelled as a beam for simplicity. This model can be further developed to a boom with flexible plate in future work.

- *Discretisation of beam elements*: The term discretisation refers to the number of beam elements used to divide the flexible body. For the same Young's modulus and cross-sectional area, the larger the discretisation, the smaller will be the length of the beam element, which results in a stiffer system. For very long flexible bodies, discretisation becomes necessary, because the Young's modulus cannot be made too high to attain the required stiffness. However,

Table 6.1: Material properties of chaser solar panel (sensitivity analysis)

	No. of beam elements [-]	Young's Modulus [Nm^{-2}]	Length per element [m]	Mean computation time [s] (10 runs)
Case 1	1	1.71×10^{11}	2.90	993
Case 2	3	5.64×10^{10}	0.97	6,717
Case 3	5	3.50×10^{10}	0.58	11,131

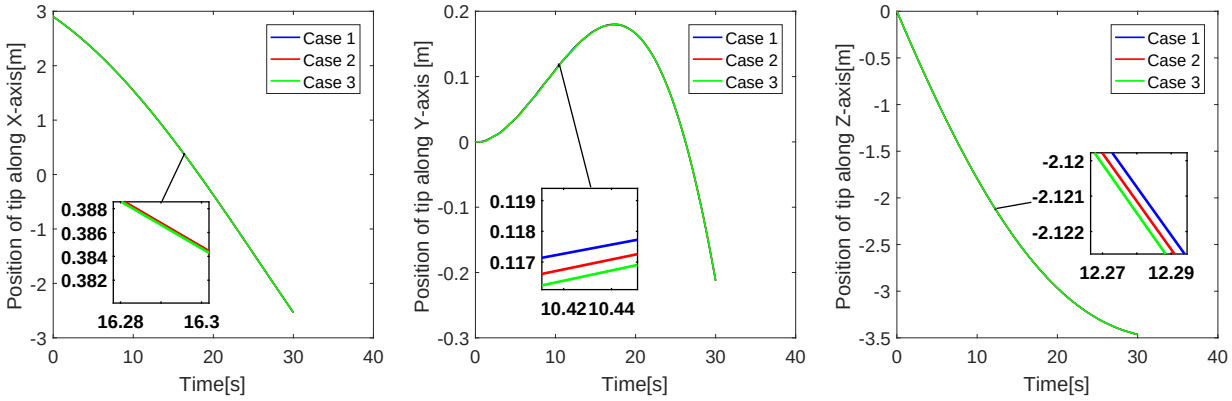

Figure 6.2: Position of tip of solar panel about X, Y and Z axis for 3 cases given in Table 6.1

for dynamic analysis, the number of interface points increase with larger number of beam elements and the state vector becomes very large. This results in large computation time. Therefore, it is imperative to find a balance between length, Young's modulus and discretisation to model the flexible elements as accurately as possible, without much increase in the computation time.

To find the correct balance between length (L), Young's modulus (E) and discretisation (number of beam elements), a sensitivity study is performed to get the best performance in terms of accuracy and computation time. Theoretically, by maintaining the same E/L ratio, it should be possible to have the same elemental stiffness. For the chaser solar panel length of 2.9 m, this analysis will be performed for three test cases as shown in Table 6.1. For different number of beam elements, the same E/L ratio is maintained. The absolute position of the tip node is studied to analyse the effect on accuracy, for a constant angular velocity of 2 °/s about all axes for a 30 s simulation with a timestep of 10^{-3} s. The computation time is averaged over 10 runs for each of the three cases[1]. Figure 6.2 shows that the effect of discretisation on the accuracy is not large for the selected test cases, since all three axes show comparable results. However, the simulation time tabulated in Table 6.1 shows that Case 1 requires the least computation time. Therefore, for the rest of the research, flexible elements will be modelled using the material properties stated for Case 1. For consistency, the same length of beam elements will be used to define the solar panels of the stacked configuration as well. This will require the target solar panel, which is 14.2 m long, to be divided into five beam elements. So, the stacked configuration in the connected phase would require a total of 6 beam elements to model the flexible bodies.

- *Density*: The density of the flexible elements is computed by simply dividing the mass of the solar panel by the volume of the beam. This is done to capture the mass properties of the solar

[1]Processor: Intel (R) Core (TM) i5 - 7200U CPU @ 2.50 GHz 2.70, Memory: 8.00GB, Graphics: NVIDIA GeForce Experience Version 3.16.0.140

panel, which has a crucial role in the flexible dynamics.

- *Boundary Conditions*: In this research, it is assumed that the chaser is already at the location of Envisat and needs to synchronise with its attitude at a fixed location. In other words, it is assumed that there is no translational motion and the satellite must spin about its centre of mass at the same location. Therefore, assuming the rigid body as a point mass, the solar panel is constrained on one end with a spherical joint. This allows the solar panel to have an angular velocity in any direction, but constrains the position of the end attached to the rigid body. In the stacked configuration, a similar assumption is made. The rigid body is assumed to be a point acting like a rigid hinge between the two panels, allowing rotation about this fixed point, but constraining the position of the ends attached to the rigid body.

While the rigid bodies can be modelled as stiffer flexible bodies (as it is done in typical FEM formulations), such an assumption proves to be computationally very heavy and induces high frequency vibrations due to numerical sensitivities as a result of the stiff system of differential equations. Alternatively, it is possible to account for the rigid body properties, without physically modelling it in the FMS. One possible way of achieving that will be discussed in the coming section.

6.2. Modelling of rigid elements

An important property of a rigid body that plays a major role in the dynamics of a system is the mass moment of inertia (also called rotational inertia). It is a measure of the body's resistance to change its direction of rotation and/or magnitude. Since it depends on the mass and dimensions of the body, the stacked configuration has an inherently larger rotational resistance. However, according to Shabana (1997), rotary inertia can be added to a flexible system using lumped masses. But, lumped masses are point masses, which do not have a geometry and, therefore, cannot have an inertia about their own axis. This eliminates the possibility to place the lumped mass at the spherical joint in the flexible model (where the control moment is also applied). Therefore, to add rotational inertia to the rigid body the lumped masses are placed at the adjacent node (or the next interface point). This way, the inertia can be translated to the constrained node using Steiner's parallel axis theorem, which gives a relation between the inertia tensor of a body with mass $\boldsymbol{M}$ relative to the centre of mass ($\boldsymbol{I_{COM}}$), and the inertia tensor relative to another point O ($\boldsymbol{I_O}$) at a distance $\boldsymbol{d}$ from the centre of mass of the body. This gives:

$$\boldsymbol{I_O} = \boldsymbol{I_{COM}} + \boldsymbol{M d^2} \tag{6.1}$$

For a point mass, the inertia simply becomes $\boldsymbol{Md^2}$. The mass matrix used here is a diagonal matrix. It should also be noted that the flexible body itself has some rotational inertia. For a slender beam, the moment of inertia can be computed about an axis at an end point using $I = mL^2/3$, where m is the mass and L is the length of the beam. For a slender beam, the inertia about the axis along the length is negligible, while the other two axes can be computed using mL^2. The sum of the inertia from the lumped masses, $\boldsymbol{I_m}$, and, that from the slender beam, $\boldsymbol{I_s}$ should account for the total inertia of the system, $\boldsymbol{I_T}$, which is given in Table 2.3 for the chaser and Table 2.5 for the stacked configuration. Therefore, the lumped mass can be calculated about each axis using:

$$\boldsymbol{I_T} = \boldsymbol{I_s} + \boldsymbol{M d^2} \tag{6.2}$$

$$\boldsymbol{M} = (\boldsymbol{I_T} - \boldsymbol{I_s})/\boldsymbol{d^2} \tag{6.3}$$

It must be stated that the computation of the mass moment of inertia for flexible body is not the perfect representation of the body's inertia. This may lead to a small mismatch between the inertia of the flexible multibody system and the rigid body inertia stated in Section 2.6. Therefore, the chosen nonlinear controller must be robust and not very sensitive to these model mismatches. Any large

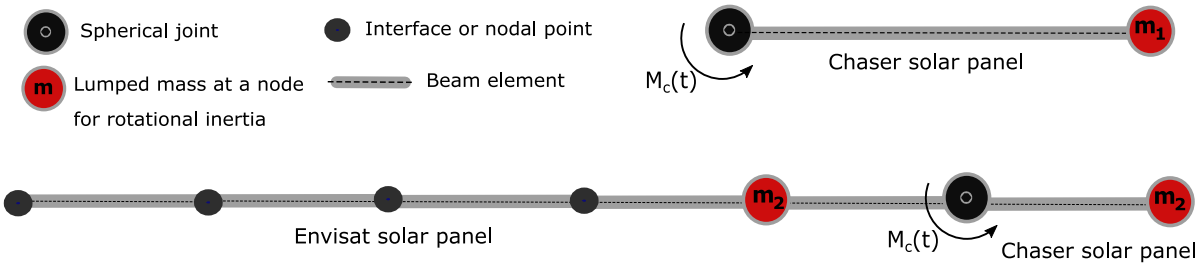

Figure 6.3: Simplified representation of the structural model for synchronisation (top) and connected (bottom) phases.

difference in inertia will still result in destabilisation of the system. It is possible to model the inertia better using shape integrals defined with respect to the global frame (Shabana, 1997). However, for this research, since the elastic deformation is defined with respect to the floating frame, the inertia shape integrals are defined locally. Therefore, this method cannot be implemented currently, but will be included in the future work.

Figure 6.3 shows the simple representation of the final configuration of the system of the chaser and the stacked model for synchronisation (top) and connected phase (bottom), respectively. Note that the lumped masses (shown in red) are added to the fixed mass matrices of the interface point (or node) only after the CB reduction has been performed. This ensures that the natural modes are not affected by the "pseudo" modelling of the rigid body inertia. Both systems are constrained at the spherical joint, which acts as the CoM of the system. The control moment for both the phases are applied at this location.

To understand the sensitivity of the system to the lumped mass inertia, the dynamics of the chaser model is simulated with an external force of 0.1 N at the tip about all axes starting with zero angular velocity. From Figure 6.4(a), it can be confirmed that as a beam element, the flexible body has negligible inertia compared to the one with the lumped mass. Without the added inertia, the angular velocity about X-axis jumps to 150 °/s within 1 s, while the one with inertia remains very small. Figures 6.4(b) and 6.4(c) show that the beam element contributes to some inertia in the Y and Z-directions. However, the inertia still remains smaller than the one with lumped mass. Another interesting observation that can be made from the figures is that the models without lumped inertia also suffer from larger vibrations under the force, despite having the same stiffness. Lastly, Figure 6.4(d) shows the angular velocity evolution with time (10 s) about all axes with lumped inertia included. Interestingly, the Z-axis with the smallest inertia (≈560 kgm^2) shows larger vibrations compared to the other two axes. Also, the system has a much smoother response compared to the model without the lumped inertia. This is because the rigid body motion now dominates in the multibody system, as anticipated.

To perform a preliminary analysis of the expected dynamics based on the different phases of the mission, it can be stated that:

- *Synchronisation:* The chaser configuration needs to start from zero angular velocity and match the target attitude, including angular velocity and orientation (which is also constantly changing with time). Sudden control moments applied at the spherical joint shown in Figure 6.3 will cause vibration in the solar panel, which will further cause a disturbance in angular velocity. Since the inertia of the chaser and also the size (and mass) of the flexible element is smaller, it must be relatively easier to control the satellite in the presence of elastic perturbations.

- *Connected:* From the figure it can also be observed that the stacked configuration has large asymmetry in geometry, as well as large inertia. Since it is tumbling at a rate of 3.5 °/s about all axes, the system becomes very dynamic (with possibly very large vibrations) and may be difficult to control.

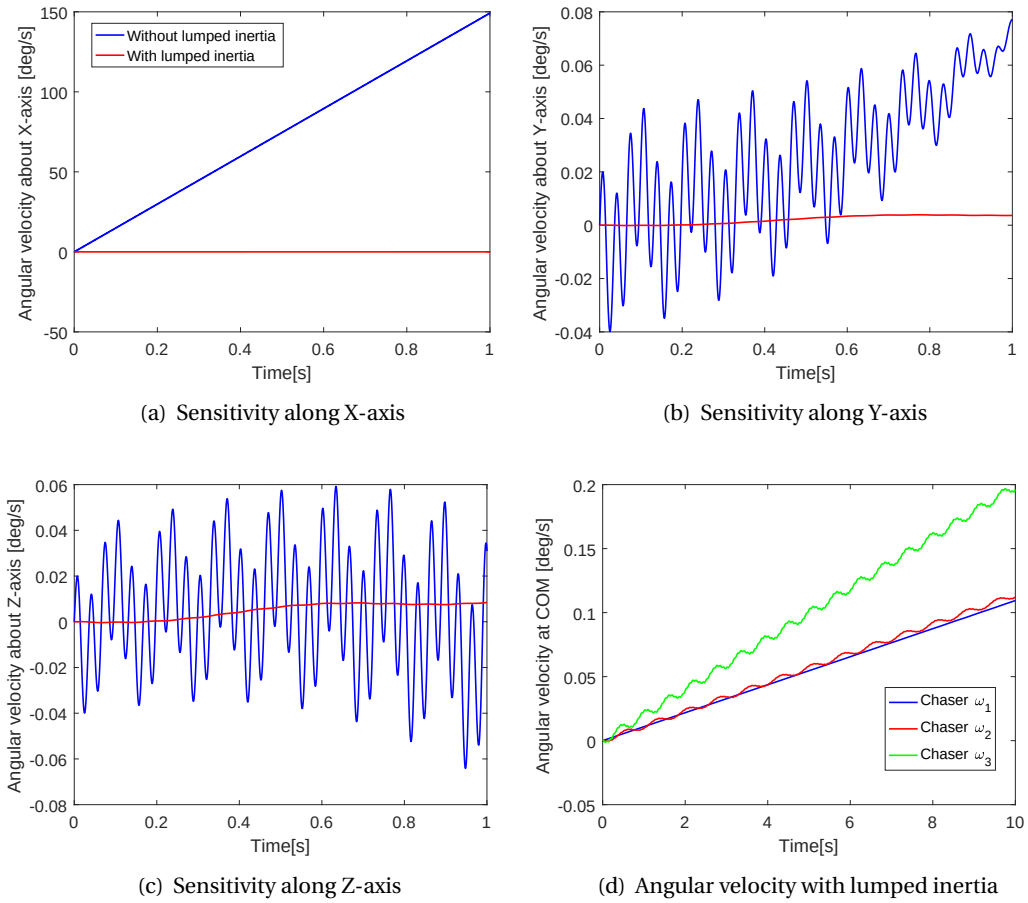

(a) Sensitivity along X-axis

(b) Sensitivity along Y-axis

(c) Sensitivity along Z-axis

(d) Angular velocity with lumped inertia

Figure 6.4: Sensitivity to lumped mass inertia

Since the vibrations will not be accounted for in the controller, the system might continue to vibrate forever without any structural damping. Therefore, it is worthwhile to include structural damping in the simulations to improve the stability and controllability characteristics of the system.

6.3. Damping

According to Santini et al. (1979), undamped flexible structures in space can have responses which can increase without limits due to exchange between kinetic and potential energy. At this point, addition of damping removes or dissipates energy from the system, preventing it from reaching an uncontrollable state. Therefore, structural damping becomes very important for stability and control of flexible space structures. Structural damping in space structures is introduced in two ways - passive and active damping. Passive damping, the most common way, is achieved through introducing energy dissipaters in structural joints (like torsional springs) and truss structures. However, it is often supported by active damping through pressure controlled joints, piezo-electric elements or damping in attitude control (through predicted behaviour or measurements with sensors). It can be said that passive damping alleviates the vibrations to a level such that active damping can be applied. According to Fujimori et al. (1986), Foist et al. (2004) and Rutkovsky et al. (1970), a typical space structure has an effective damping ranging between 0.5% to 3%. However, in combination with active damping, this value can be increased to 5% (Santini et al., 1979).

When a system is weakly damped and its eigenfrequencies are well-separated, the effect of cross-damping can be neglected (Géradin and Rixen, 2014). This assumption, proposed by Lord

Rayleigh, simplifies a complex multiple degree of freedom (MDOF) system to a collection of single degree of freedom (SDOF) oscillations. Recalling the first statement, for the current configuration and dynamic modelling, both conditions are true. Damping in space structures is very small, and the dynamic modelling is such that the mass and stiffness matrices used in the EOM can be written in the form, $\boldsymbol{\phi}_{\boldsymbol{CB}}^{\boldsymbol{T}}\boldsymbol{M}\boldsymbol{\phi}_{\boldsymbol{CB}}$ and $\boldsymbol{\phi}_{\boldsymbol{CB}}^{\boldsymbol{T}}\boldsymbol{K}\boldsymbol{\phi}_{\boldsymbol{CB}}$, where $\boldsymbol{\phi}_{\boldsymbol{CB}}$ denotes the modal mass matrix after CB reduction. This diagonalises the system and decouples the undamped modes. It is now possible to apply proportional damping or Rayleigh damping, which is widely used to model dissipative behaviour in complex structures. Here, the damping matrix, $\boldsymbol{C}$, can be expressed as a linear combination of mass and stiffness matrices (Géradin and Rixen, 2014):

$$\boldsymbol{C} = \alpha\boldsymbol{M} + \beta\boldsymbol{K} \tag{6.4}$$

where α is the mass proportional damping coefficient, and β is the stiffness proportional damping coefficient. These terms can then be related to the damping ratio using:

$$\xi_n = \frac{1}{2\omega_n}\alpha + \frac{\omega_n}{2}\beta \tag{6.5}$$

where ξ_n is the damping factor, and ω_n is the associated natural frequency. For two natural frequencies, the expression can be written as:

$$\begin{pmatrix}\xi_i\\ \xi_j\end{pmatrix} = \frac{1}{2}\begin{bmatrix}\frac{1}{\omega_i} & \omega_i\\ \frac{1}{\omega_j} & \omega_j\end{bmatrix}\begin{pmatrix}\alpha\\ \beta\end{pmatrix} \tag{6.6}$$

where subscripts i and j are associated with the first two important natural frequencies. Usually, each natural frequency has a different contribution or critical damping ratio. However, assuming both modes have the same critical damping factor, the values of α and β are tabulated in Table 6.2 for both chaser and Envisat solar panels. Since the chaser solar panel is smaller and susceptible to lesser vibrations, a smaller value of damping factor can be selected. Envisat solar panel would require larger damping but within the range of structural damping in space structures, since no active damping is involved. Therefore, a damping ratio of 0.005 (0.5%) and 0.02 (2%) is selected for the chaser and Envisat solar panel respectively. Note that the first two natural frequencies are computed using the natural frequency of a cantilever beam given by :

$$f_n = \frac{K_n}{2\pi}\sqrt{\frac{EI}{\rho AL^4}} \tag{6.7}$$

Here, $K_n = 3.52$ for the first mode of vibration and $K_n = 22.0$ for the second mode, E is the Young's modulus in $\mathrm{N/m^2}$, ρ is the density in $\mathrm{kg/m^3}$, A is the cross-sectional area in $\mathrm{m^2}$, I is the area moment of inertia in $\mathrm{m^4}$ for a rectangular cross-section. A disadvantage of Rayleigh damping is that it proves to be ineffective when a wide range of frequencies is considered (Géradin and Rixen, 2014). However, the new dynamic multibody modelling method used in this research considers only reduced modes or important modes. Therefore, Rayleigh damping still performs well for this method. The assumption of proportional damping also reduces the computation time, making it well suited for control applications with longer simulation times.

To understand the effect of damping on the dynamics and stability of the system, the previously simulated case of the chaser with 0.1 N tip force for the first 10 s is now done with the damping included. Figure 6.5 shows the response of the system with and without damping. From the figure, it can be observed that addition of damping smoothens out the small oscillations seen in the system without damping, without affecting the mean motion or rigid body motion of the system. Therefore, damping can promote the controllability characteristics of a structure by reducing such perturbations.

Table 6.2: Damping coefficients for flexible elements

	ξ_n	f_{n1} [Hz]	f_{n2} [Hz]	α	β
Envisat	0.02	0.0563	0.3523	0.0156	0.0122
Chaser	0.005	2.4374	15.2344	0.00014	0.0825

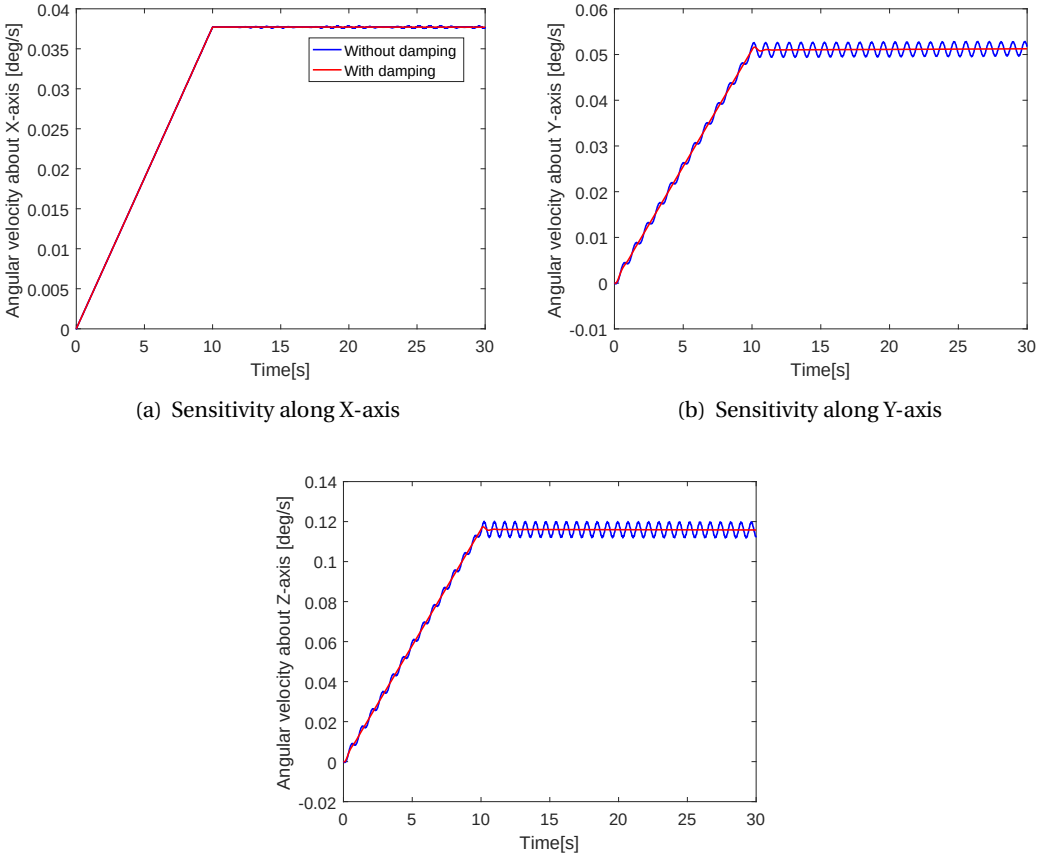

(a) Sensitivity along X-axis

(b) Sensitivity along Y-axis

(c) Sensitivity along Z-axis

Figure 6.5: Response to 0.1 N tip force with and without damping

Now that the modelling has been established, the simulations can be performed using the multibody model for the two phases of the mission, and the performance of the chosen controllers can be analysed.

7

Results

In this chapter, the results from the simulation are presented. The simulations are made in an iterative manner. Initially, they are made without structural damping in the flexible model. Only if convergence is not achieved due to large oscillations, the damping is included. Also, the worst case scenario of Envisat tumbling at 3.5°/s is analysed first. If convergence is achieved in this case, the other two attitude scenarios stated in Table 2.2 are not simulated. The rigid body simulations presented in Chapter 4, are used as benchmark to analyse the performance of the controllers. All simulations are made with a integrator relative and absolute tolerance of 10^{-7}. The dynamics is simulated with a step size of 10^{-3} s and the controller is sampled at 25 Hz. The control moment saturation is initially set to ±50 Nm, as proposed by Habets (2015). As mentioned before, both sensors and actuators are assumed to be ideal. The gains used for the flexible simulations are the same as that used in the benchmark simulations, stated in Table 3.3.

In Section 7.1, the results from the synchronisation phase are presented.

7.1. Synchronisation

In the synchronisation phase, the configuration to be controlled only consists of the chaser spacecraft, which has a 2.9 m long solar panel. The system is expected to be relatively easier to control compared to the stacked configuration due to lower flexibility and inertia. The chaser state starts with an initial angular velocity of 0°/s. Therefore, the initial chaser state vector, in the sequence, angular velocity, quaternions, pseudo Euler angles, is given by:

$$\boldsymbol{x_{0,cha}} = (0,\ 0,\ 0,\ 0,\ 0,\ 0,\ 0,\ 1,\ 0,\ 0,\ 0)^T \tag{7.1}$$

and the Envisat initial state is given by:

$$\boldsymbol{x_{0,tar}} = (3.5,\ 3.5,\ 3.5,\ 0,\ 0,\ 0,\ 1,\ 0,\ 0,\ 0)^T \tag{7.2}$$

However, the Envisat attitude, which acts like the commanded state for the controller, is continuously changing. This can create a large error in attitude (as explained in Section 3.5), which makes it difficult for the controllers to stabilise the complete state (angular rate and orientation). Therefore, first rate control is applied until a threshold is reached, after which the controller switches to full state control. For the current simulation, this threshold was set to a norm of 0.5°/s for the angular velocity. Note that the worst case scenario is analysed first.

Figure 7.1 shows the performance of both PD and INDI controllers in the synchronisation phase with the flexible multibody plant (without damping). Both the controllers successfully synchronise the chaser (solid line) with the target attitude (dashed line). From Figures 7.1(a) and 7.1(b), it can

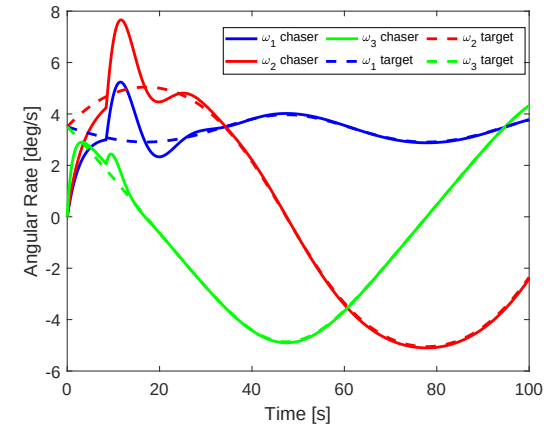

(a) PD angular rates

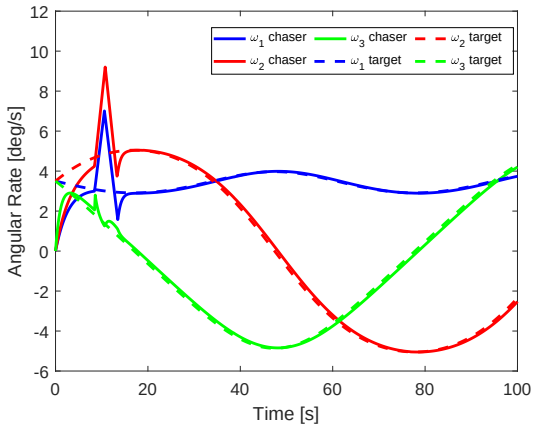

(b) INDI angular rates

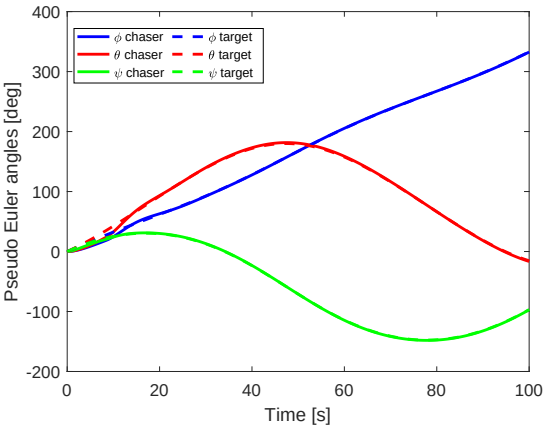

(c) PD pseudo Euler angles

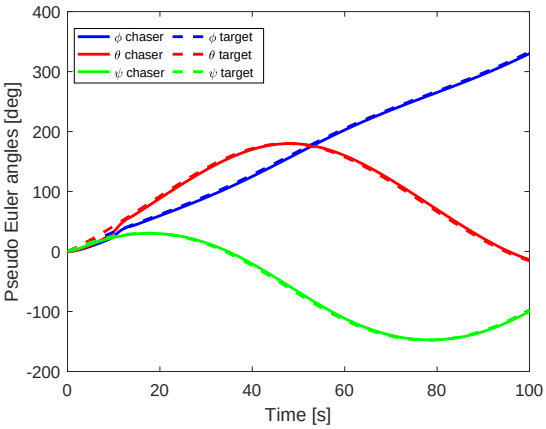

(d) INDI pseudo Euler angles

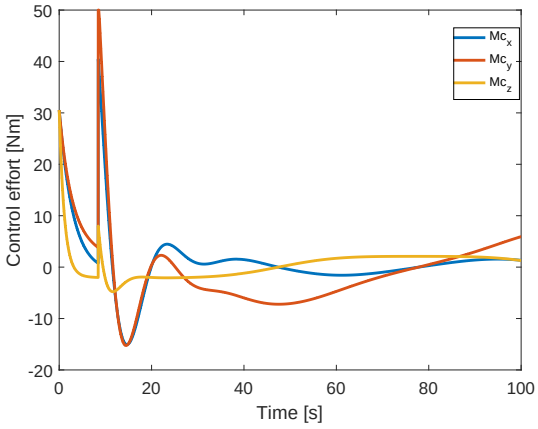

(e) PD control effort

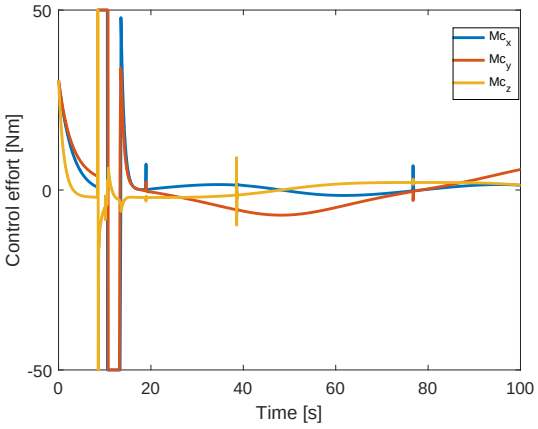

(f) INDI control effort

Figure 7.1: Flexible multibody control (without damping)- Synchronisation

be observed that INDI achieves steady state faster than the PD controller. This is unlike the observation made in the benchmark rigid body simulations from Figure 3.8, wherein both controllers showed similar convergence time. This is possibly because INDI being a nonlinear controller, is more sensitive to the small vibrations that were induced during the switch from the rate control to

full control. Therefore, it attempts to correct the error quickly, which can be observed from Figure 7.1(f), where small spikes in the control moment is observed. These spikes were not observed in the rigid body simulations and so, they are possibly caused by due to the flexibility in the system.

From the figures, it can also be observed that the INDI controller suffers from a steady state error on convergence. The same observation was also made in the benchmark simulations (see Figure 3.8(b)). It was established before that the steady state error occurred because of the high overshoot during the switch from rate control due to which the controller suffers from a slight phase lag. Nonetheless, for synchronisation case, the nonlinear controller did not give superior performance in terms of accuracy but showed slightly faster convergence. Since the response of the FMS was similar to the benchmark simulations even without structural damping, it can be concluded that the rigid body motion dominates in the synchronisation phase, and the flexible perturbations did not cause a significant effect on attitude. Since the controllers successfully achieved steady state for the worst case attitude scenario of 3.5°/s about all axes without structural damping, the other (easier) attitude scenarios will not be simulated.

7.2. Connected

The connected phase deals with the stacked configuration, which consists of one large rigid hub with two asymmetrical panels, one 14.2 m long and one 2.9 m long. The stacked configuration also has an asymmetric inertia distribution, with the rotational inertia about X and Z-axis almost an order larger than the one about Y-axis (refer Table 2.5). The asymmetry in the properties (both flexible and rigid) makes it a challenging control problem. In this state, the stacked configuration is assumed to start from an initial angular velocity (depending on the attitude case from Table 2.2). Therefore, for the worst case scenario, the initial state vector becomes:

$$\boldsymbol{x_{0,stack}} = (3.5,\ 3.5,\ 3.5,\ 0,\ 0,\ 0,\ 0,\ 1,\ 0,\ 0,\ 0)^T \tag{7.3}$$

As stated before, the connected phase is analysed for a number of operations associated with deorbitation, which are repeated here for convenience:

- Detumbling only, where the angular velocity is reduced from the initial value to zero.
- Detumbling and reorientation, where the goal is to achieve zero angular velocity and defined orientation. For simulations, pseudo Euler angles of $(0°,\ 0°,\ 0°)^T$ are commanded.
- Reorientation only, where the defined orientation must be achieved starting from zero angular velocity. For simulations, pseudo Euler angles of $(50°,\ -60°,\ 30°)^T$ are commanded.

The simulations will be first made without damping. In case of failure, an analysis will be performed to study the possible causes, which can be used to improve the controllability characteristics of the system with damping.

7.2.1. Without Damping

Since the stacked configuration is characterised by relatively larger flexibility and much larger inertia compared to the chaser configuration, it is more difficult to predict the behaviour of the system. Larger control moments can improve the controllability due to the large rigid body inertia, but can cause large amplitude vibrations in the solar panels. Similarly, smaller control moments will induce smaller vibrations in the flexible elements but might prove to be insufficient to stabilise the system. Therefore, to understand these characteristics better, simulations are made for all operations of detumbling and/or reorientation for three attitude cases stated in Table 2.2 using three different control saturation limits of ±25 Nm, ±50 Nm and ±100 Nm. The results from the simulations are recorded in Table 7.1. It was found that the flexible vibrations induced were too vigorous for the chosen controllers. Even with ±25 Nm control moment, the vibrations induced were considerable. Additionally, in the absence of structural damping, these vibrations grew with time and completely

Table 7.1: Summary of different detumbling and reorientation simulations.

Intial angular rate $\lvert M_{c,max} \rvert$	ω = 3.5 °/s [all axes]			ω = 1.5 °/s [all axes]			ω = 3.5 °/s [Z-axis only]		
	±25	±50	±100	±25	±50	±100	±25	±50	±100
	[Nm]			[Nm]			[Nm]		
Detumbling only[P controller]	FAIL	FAIL	FAIL	FAIL	FAIL	FAIL	FAIL	FAIL	FAIL
Detumbling + Reorientation [PD controller]	FAIL	FAIL	FAIL	FAIL	FAIL	FAIL	FAIL	FAIL	FAIL
Detumbling + Reorientation [INDI controller]	FAIL	FAIL	FAIL	FAIL	FAIL	FAIL	FAIL	FAIL	FAIL
Reorientation [PD controller]	FAIL	FAIL	FAIL	FAIL	FAIL	FAIL	FAIL	FAIL	FAIL
Reorientation [INDI controller]	FAIL	FAIL	FAIL	FAIL	FAIL	FAIL	FAIL	FAIL	FAIL

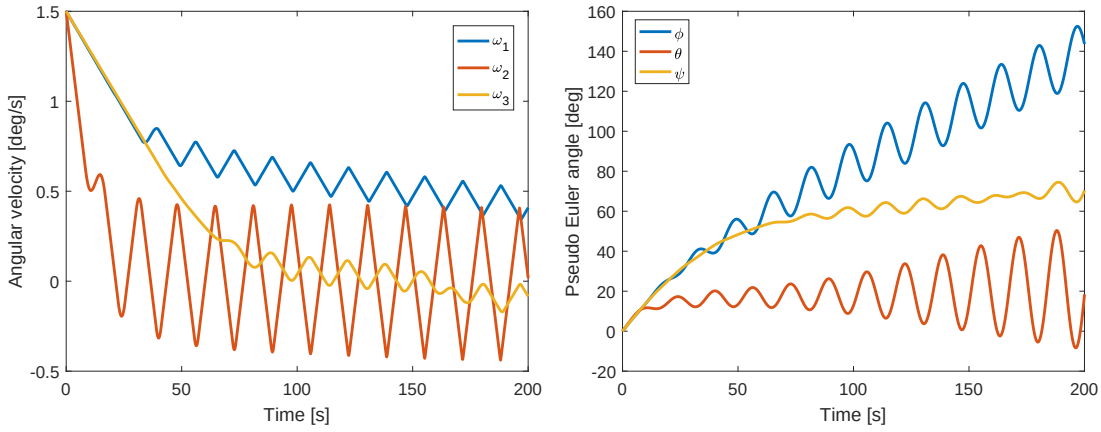

(a) Angular rates (b) Pseudo Euler angles

Figure 7.2: Flexible multibody control (without damping)- Detumbling only
($M_{c,lim}$ = ±50, ω= 1.5 °/s [all axes])

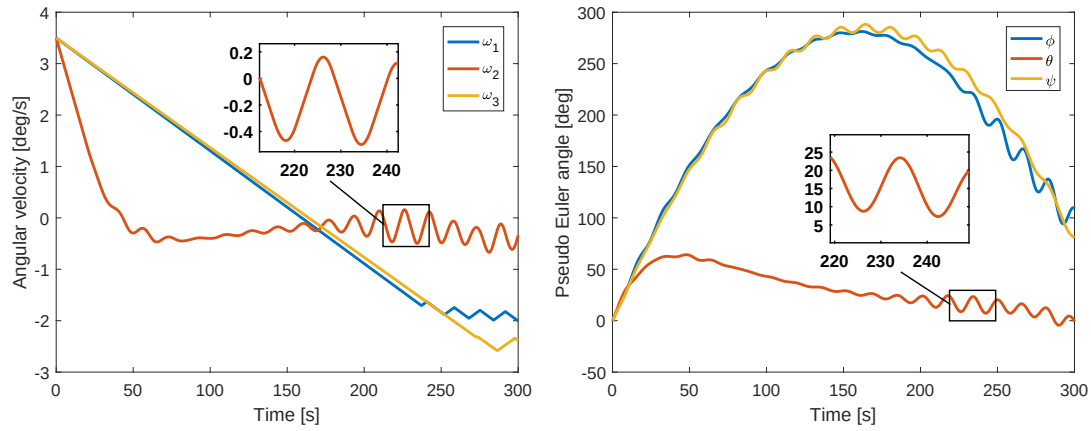

(a) INDI angular rates (b) INDI pseudo Euler angles

Figure 7.3: Flexible multibody control (without damping)- Deorbitation + Reorientation
($M_{c,lim}$ = ±50 Nm, ω= 3.5 °/s [all axes])

destabilised the system.

Figures 7.2 through 7.4 show the response for three of the failed cases, one each from detumbling only, detumbling and reorientation, and reorientation only, respectively. In the detumbling

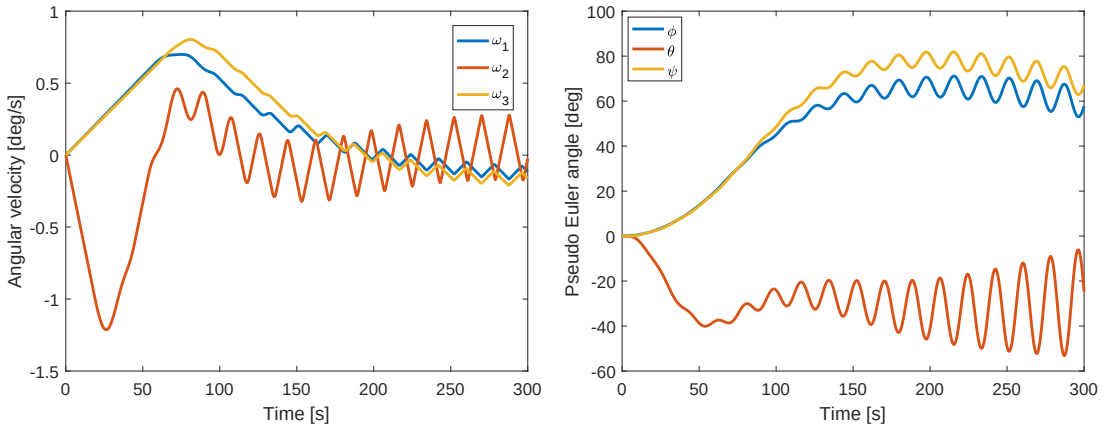

(a) PD angular rates

(b) PD pseudo Euler angles

Figure 7.4: Flexible multibody control (without damping)- Reorientation only
$M_{c,lim} = \pm 25$, $\boldsymbol{\Theta} = (50°, -30°, 60°)^T$

phase, wherein only the rate control is performed, very large amplitude vibrations (upto ±0.5°/s in angular velocity and ±50° in pseudo Euler angles) are observed within the first 200 s with a control limit of ±50 Nm, as it can be seen from Figure 7.2. Y-axis being the one with the lowest inertia, suffers the largest deflections. A certain level of coupling between the axes can also be observed since the braking in the X and Z directions seems to aggravate the vibrations about Y-axis. This can be attributed to the inertial coupling in the rigid body EOM seen in the term $\boldsymbol{\omega} \times \boldsymbol{I\omega}$. As stated before, the flexible body itself has rigid body properties, which is coupled with the flexible dynamics. This coupling between the axes, also known as the gyroscopic coupling, translates into the flexible vibrations and further, excites the eigenmodes. Additionally, in all the phases, the vibrations only appear when the control moments are unsaturated. This indicates that when the control moment is applied, the work is translated into elastic or strain energy. When the control moment is reduced, the solar panel acts similar to a spring that is released from its compressed state. This continues till a new equilibrium is reached in energy.

Next, from Figure 7.3, it can be observed that smallest vibrations are induced when INDI controller is used. It can also be seen that the Y-axis converges a lot faster than the other two axes. By the time the angular velocity about the other two axes start braking, the vibrations about Y-axis has already amplified with time due to the large difference in inertia. A possible solution to correct this problem is by scaling the control moment limits to the inertia ratio between the three axes, so that convergence of the response for all the axes happen closely. Lastly, an important observation that can be made from Figure 7.3 is the frequency of vibrations. The oscillation completes one cycle in approximately 16 s, which gives a frequency of 0.06 Hz. According to Biesbroek (2017), one of Envisat's principal solar array mode is 0.06 Hz, with an uncertainty of 20%. This validates that the flexible multibody model closely represents the experimental values obtained from the vibration testing of Envisat solar panel. The control moment therefore, excites the natural frequency of the Envisat panel.

Lastly, the reorientation phase is shown in Figure 7.4, using the PD controller and a lower control limit of ±25 Nm. The PD controller, even with the lower control limit, induces larger vibrations than the INDI controller within 300 s, as it can be seen from Figures 7.4 and 7.3. Additionally, the amplitude of vibration can be observed to be increasing a lot faster when using PD controller compared to INDI controller. From this preliminary analysis, INDI seems to be the more stable controller compared to PD.

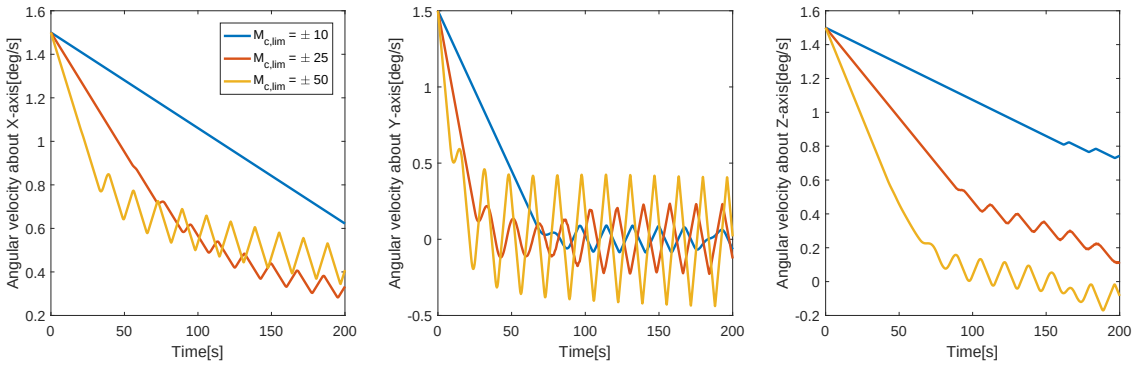

Figure 7.5: Flexible multibody control - Detumbling
(sensitivity to control moments)

To check if the induced vibrations can be reduced using lower control moments, a sensitivity analysis is performed on the control moments for the detumbling phase for the attitude case of 1.5 °/s about all axes. Figure 7.5 shows that the smallest control moment limit of ±10 Nm shows the least amplitude of vibrations. This confirms that by choosing a smaller control moment limit, the induced vibrations can be minimised. However, choosing smaller control moments would require long simulation times, which may prove to be computation intensive. Based on the observations made from these failed simulations, some conclusions can be drawn to improve the subsequent simulations:

- The system cannot be controlled without any structural damping, since the amplitude of vibrations increase with time and the system continuously gains elastic energy, which eventually results in destabilisation of the satellite. Therefore, a dissipative force like damping can improve the controllability of the system.
- The control moments excite the dominating natural frequency of Envisat solar panel, which has a frequency of 0.06 Hz. This is confirmed by Biesbroek (2017) (official Envisat document) and the accuracy of the model is validated.
- The angular velocity about Y-axis converges quickly and suffers from larger vibrations due to the relatively smaller inertia. For a better performance, the control moments can be scaled according to the inertia about each axis. This will prevent the vibrations amplifying with time, when the other axes has not achieved convergence.
- Smaller control moments result in smaller vibrations, but increase the time required for convergence by a considerable amount. Additionally, damping being energy dissipative, can add to the computation time as the system is not conservative anymore. This makes the system more dynamic and requires larger iterations during integration. Therefore, the simulations with lower convergence time should be performed first to ensure that the analysis can be done within the computation power available.

7.2.2. With damping

The simulations for the connected phase are now performed with 1.5% damping. The control moments are scaled down to ±(10, 5, 10) Nm to account for the inertia difference and to minimise the vibrations induced due to control moments. An angular velocity of 3.5°/s about all axes required large computation time of greater than 2000 s with the reduced moments. And, in the presence of damping, higher computation effort is required. So, this attitude scenario could not be completed with the available computational resources in an acceptable time. Therefore, simulations are made

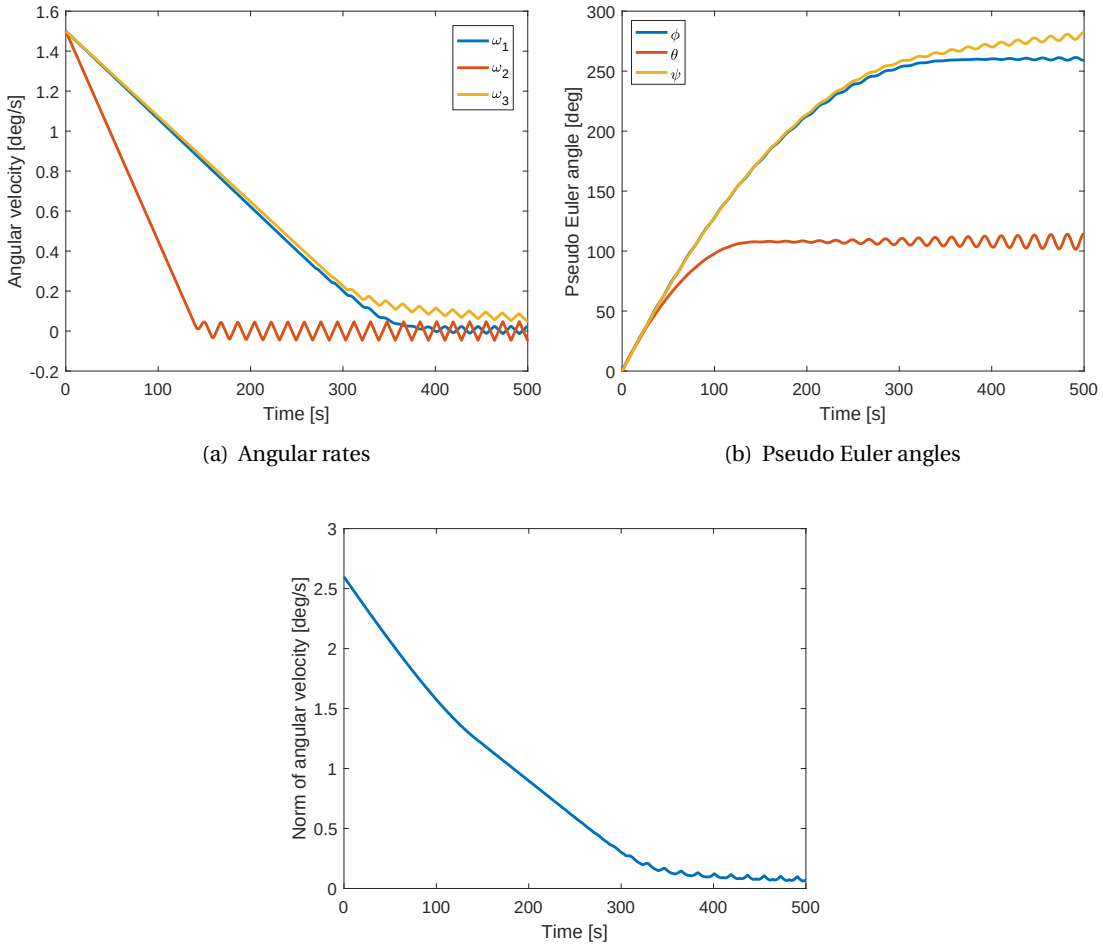

(a) Angular rates

(b) Pseudo Euler angles

(c) Norm of angular velocity

Figure 7.6: Flexible multibody control (with damping)- Detumbling only
$M_{c,lim} = \pm(10, 5, 10)$ Nm

with an initial angular velocity of 1.5°/s about all axes, and the results will be presented for all operations in the connected phase.

Detumbling only

Figure 7.6 shows the detumbling of the stacked configuration with structural damping included. Compared to Figure 7.2, the performance has improved considerably, since the vibrations in angular velocity, which was previously upto ±0.5°/s has reduced to ±0.1°/s. The norm of the angular velocity also indicates good convergence. Further, the rather rapid growth in vibration that was observed in the absence of damping has reduced considerably. However, the small vibrations in the system could not be damped out with the current value of damping ratio. Recalling Figure 2.1 from mission heritage, which showed that the Rosetta attitude still experienced small amplitude vibrations of ±0.05°/s, this result is expected, since the controllers are used in their fundamental form. Also, the deorbitation manoeuvre being a finite time burn, can last several tens of minutes as suggested by Linskens and Mooij (2016) (may be even lasting more than an orbit). During this time, the closed-loop feedback guidance would have sufficient opportunity to correct for any thrust orientation mismatch that may result from the flexible perturbations. Therefore, the vibrations are within the acceptable range for deorbitation manoeuvre.

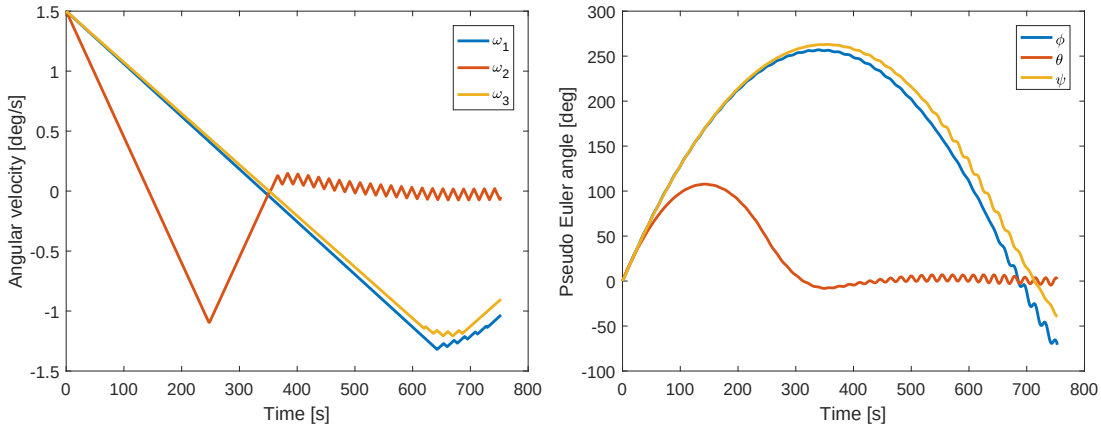

(a) Angular rates

(b) Pseudo Euler angles

Figure 7.7: Flexible multibody control (with damping)- Detumbling + Reorientation with INDI
$M_{c,lim} = \pm(10, 5, 10)$ Nm

Detumbling and Reorientation

Figure 7.7 shows the detumbling and reorientation manoeuvre using the INDI controller. It can be seen that the Y-axis has achieved rigid body convergence, but experiences small perturbations due to the flexibility. The X- and Z-axes require more time for convergence, but are expected to behave similarly[1].

Reorientation only

Figure 7.8 shows the response of the system while performing reorientation manoeuvre for both PD and INDI controllers. INDI controller converges sooner compared to the PD controller. Again, compared to the undamped case, the performance of both the controllers have improved considerably with the vibrations in angular velocity reduced to $\pm 0.1°/s$. The oscillations induced during the braking manoeuvre are comparable for both PD and INDI controllers (as they increase with time). However, INDI shows a much faster convergence of rigid body motion (within 250 s) compared to PD controller (about 600 s). An interesting observation that can be made from Figures 7.8(e) and 7.8(f), is that the control moments after achieving sufficient convergence in rigid body motion, start correcting for the flexible perturbations. This results in a bang-bang control, which ends up exciting the eigenmodes further. Therefore, for control of flexible perturbations, the selected controllers are insufficient. The performance can be improved by adding active damping to the system. One common way of achieving this, is by introducing bending filters meant for controlling flexible modes. According to Orr (2013), simple low-pass filters commonly used in aircraft feedback systems, do not provide sufficient performance to ensure robust stabilisation of the structural modes. This happens because the filter introduces a penalty in open-loop phase that prevents stable control of the rigid body dynamics. Without any compensatory filter, similar behaviour was observed (Figure 7.8), *i.e.*, a strong coupling between rigid body dynamics, flexible modes, and control actions.

[1] Due to the long computation time, the simulation could not be finished before thesis submission.

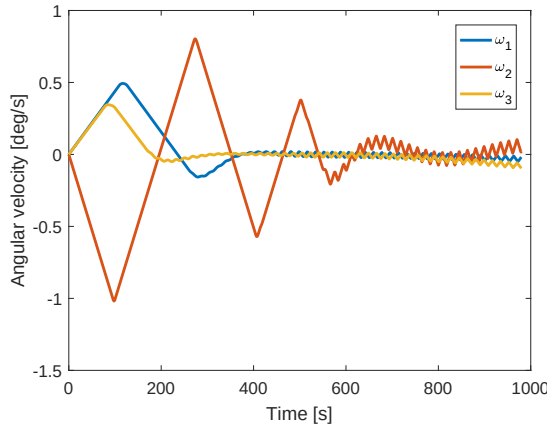

(a) PD angular rates

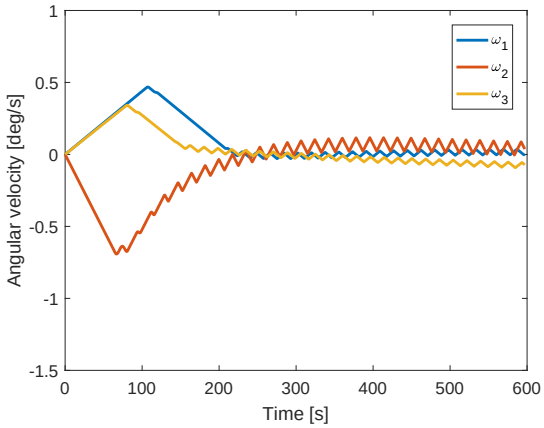

(b) INDI angular rates

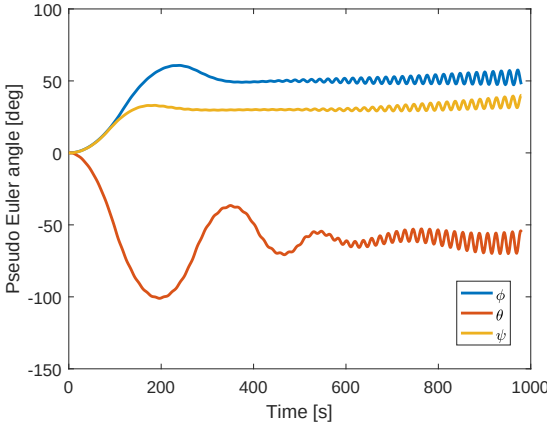

(c) PD pseudo Euler angles

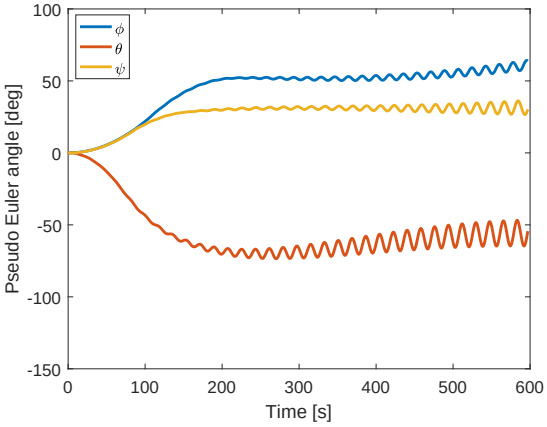

(d) INDI pseudo Euler angles

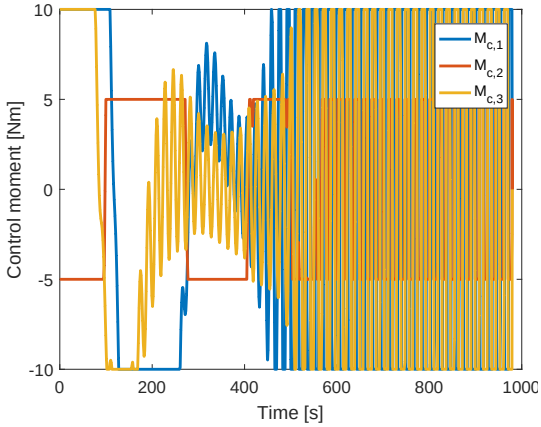

(e) PD control moments

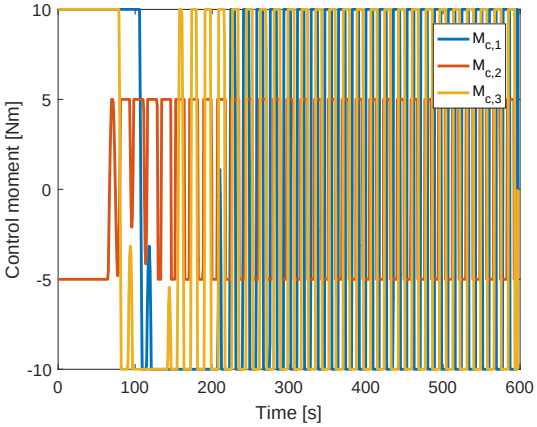

(f) INDI control moments

Figure 7.8: Flexible multibody control (with damping)- Reorientation only
($M_{c,lim}$ = ±(10, 5, 10) Nm, $\boldsymbol{\Theta}$ = (50°, -30°, 60°)^T

8

Conclusion and Recommendations

The thesis aimed to investigate the dynamics and controllability characteristics associated with a chaser spacecraft before, and after docking with large inactive space debris. The test case developed in this research is in line with European Space Agency's (ESA's) e.deorbit mission, which aims to perform Active Debris Removal (ADR) of Envisat, a massive tumbling debris with a large appendage. The work also demonstrates the capabilities of a novel multibody approach based on floating reference frames, which provides a good balance between accuracy and computation time, while enabling easy constraint modelling. In this chapter, some conclusions drawn from the study will be presented along with some recommendations for future work.

8.1. Conclusions

In this study, two phases of the mission, namely, synchronisation and connected phase were modelled and evaluated. A study was performed to understand the interaction between rigid body and flexible body dynamics, and its effect on controller performance of a linear PD controller and an Incremental Nonlinear Dynamic Inversion (INDI) controller. With this the research question was formulated to be:

> *What are the dynamics and controllability characteristics of a flexible chaser spacecraft before and after docking with a large, flexible and uncooperative space debris?*

To analyse the research question in detail, it was further subdivided into many smaller questions as stated below:

- Does the new multibody technique demonstrate good compatibility with the modelling and control of the flexible multibody system in both synchronisation and connected phases?
- What are the complications introduced in the control of the system due to coupling of rigid and flexible body dynamics?
- Can simple controllers designed for rigid bodies stabilise the system in the presence of flexible perturbations?
- What are the structural aspects that affect the vibrations in the flexible elements?
- How does the controllability of a flexible system differ from that of a rigid system?
- How does a linear controller perform for such a nonlinear dynamic system?
- Will the application of a nonlinear controller show improved response characteristics?

The conclusions, which include the answers to all the above stated questions, are presented in two parts in the sequence of the mission phases. Then, a brief discussion is included for the performance of the multibody method.

8.1.1. Synchronisation

In the synchronisation phase, the chaser with a 2.9 m long solar panel was commanded to match the tumbling attitude of the target starting from zero angular velocity. The simulations were first made for the worst case scenario, wherein no structural damping was included and the target was assumed to be tumbling about all three axes with an angular velocity of 3.5°/s. Since the initial error in angular rate was relatively large, a rate controller was used upto a certain threshold (0.5°/s) after which a switch was made to the PD or INDI controller. The control limit was set to ±50 Nm for this phase. The chaser was successfully stabilised using both PD and INDI controllers, even in the absence of damping. The effect of flexibility did not appear to be evident during the synchronisation phase. The INDI controller showed faster convergence when compared to the PD controller for the flexible model. However, INDI suffered from a large overshoot during the switch from rate control and kept a small steady state error throughout synchronisation. No further simulations were made with damping, as the system was stabilised for the worst case scenario.

8.1.2. Connected

In the connected phase, the stacked system (docked configuration) with two asymmetric solar panels (14.2 m and 2.9 m) was commanded to perform three operations associated with deorbitation manoeuvres, *i.e.*, detumbling only, detumbling and reorientation, and reorientation only.

Without damping

An attempt was made to first stabilise the system in the worst case scenario with an angular velocity of 3.5°/s. Due to the unpredictable behaviour of the complex dynamics, different control limits of ±25, ±50 and ±100 Nm were used. Both the controllers failed to achieve convergence in the absence of damping, as large amplitude vibrations (±0.5°/s) were induced. Even for easier attitude control cases, assuming 1.5°/s about all axes, and 3.5°/s about Z-axis, convergence could not be achieved. Vibrations were induced due to the excitation of the eigenfrequency of the larger panel (from Envisat) on interaction with the control moments. Without damping, the vibrations grew without limit and destabilised the system. The frequency of vibration matched the dominating natural frequency observed from the vibration tests of Envisat's solar panel. This shows that the flexibility characteristics of the solar panel were captured correctly using the new multibody model. Further, it was observed that the vibrations appeared only when controls were unsaturated. This suggests that the control moment was translated into elastic energy, which was stored in the solar panel. When the control moment reduced, the solar panel acted like a released spring causing large vibrations in the system. Nonetheless, it was observed that smaller vibrations were induced in the system when INDI controller was used.

Sensitivity analysis

To analyse the possible ways of improving the controllability characteristics of the system, a sensitivity analysis was performed. From this, it was concluded that the vibrations induced due to control could be reduced by using smaller control limits. Further, it was observed that the Y-axis had the largest vibrations, because of the lowest inertia. The vibrations aggravated due to the coupling with X- and Z-axes, as the Y-axis had converged a lot faster and already contained vibrations that increased with time. Therefore, to solve this problem, the control limit about Y-axis was taken to be smaller than about X and Z-axes. It was also found that addition of dissipative forces like damping, improved the convergence characteristics of the system and contained the growth of vibrations. However, inclusion of damping increased the computation time considerably and the worst case scenario of 3.5°/s about all axes could not be completed with the currently available resources within a reasonable time.

With damping

The three operations were simulated again with the attitude case of 1.5°/s about all axes. A structural damping of 1.5% and control limit of ±(10, 5, 10) Nm was used. The results showed considerable improvement over the previously simulated case, and the observed vibrations were reduced to 0.1°/s. Even though the vibrations could not be damped out completely, it was concluded that any errors caused during the deorbitation manoeuvre by such small vibrations, can be corrected by the closed loop guidance system within a finite time. It was again observed that the INDI controller showed faster convergence in the presence of flexible perturbations. Further, after sufficient convergence was achieved in the rigid body motion, the controller attempted to correct the flexible perturbations. This resulted in bang-bang control, which excited the primary eigenfrequency instead of correcting the motion. Therefore, it was concluded that a simple rigid body controller could not be used to control the flexible modes in the system and dedicated bending filters would be required for such corrections. To summarise, a strong coupling was observed in the rigid body dynamics, flexible vibrations and control actions.

8.1.3. New Multibody approach

The new multibody approach allowed inclusion of the nonlinear Flexible Multibody Dynamics (FMD) in the control loop. This facilitated the study of flexible dynamics and control interaction. Further, the ease of contraint handling allowed quick modelling of changing configurations for the different phases of the mission. Very large angle rotations (greater than 360°) could be simulated, which was achieved without any singularity with the use of Pseudo Euler angles in the controller. As stated before, the flexible behaviour observed in the system was confirmed by the data obtained from ground tests, proving the accuracy of the method. It also proved to be computationally efficient, because complex dynamics could be simulated in combination with control in finite time, despite a large state vector of 159 elements during the connected phase.

8.2. Recommendations

The recommendations for further development of the research can be divided into five parts. The first aspect deals with the application of ADR itself. The second aspect deals with an improved modelling of the FMD. The third one is based on better structural adaptation of the satellite for the new FMD model. The fourth part deals with improving the control system design. Lastly, some smarter choices can be made to enhance the performance of the simulator numerically. These suggestions will be discussed in detail in the coming sections.

8.2.1. Active Debris Removal

To complete the mission profile of ADR using a chaser satellite, the *semi-connected* phase of the mission can be modelled. In this phase, the chaser and target are connected with one or more flexible links (tentacles), while the complete system is tumbling. It is possible to model the phase as a multibody system with alternating flexible and rigid bodies in a chain like configuration consisting of Envisat panel (flexible) - Envisat hub (rigid) - flexible connection (flexible) - chaser hub (rigid) - chaser panel (flexible).

Alternatively, the connection can be modelled using evolving systems approach as shown by Habets (2015). In this model, the connection is modelled using a rotational spring and damper, which evolve from an unconnected state to a connected state in a finite time. The dynamics and controllability characteristics of this mission phase in combination with the FMD will be very interesting to study. Additionally, possible disturbances in the flexible connection due to attitude mismatch between chaser and Envisat can be analysed.

8.2.2. Flexible Multibody Dynamics

The FMD of the system can be modelled more accurately by including the effect of quadratic velocity terms, like centrifugal stiffening, Coriolis forces and other rigid-flexible coupling terms (discussed in Section 4.3.2) in the FMD. The modelling technique can be extended to incorporate a actual rigid body in combination with the flexible bodies. Further, the effect of environmental torques like gravity gradient, atmospheric drag, *etc.* can also be taken into account. The model can be extended with inclusion of the orbital (translation) motion of the system. Other dynamic scenarios associated with the space environment like deorbitation manoeuvre (associated with a large external propulsive force, which can excite the eigenfrequencies) and impact with space debris (impulsive force) can also be analysed with the model. Since it was observed that the braking manoeuvre about one axis induced and amplified the vibrations about other two axes, another interesting aspect to study in detail would be the flexible coupling between the three axes. Lastly, in this research it was assumed that the solar panel rotates at the same rate as the rigid body and only bending modes were analysed. Therefore, the effect of torsional modes of vibrations can also be considered in future work.

8.2.3. Structural Model of the Satellite

To model the satellite more accurately using the new FMD formulation, a number of improvements can be made. First, the solar panel can be modelled using a more realistic configuration, like a plate attached to a boom. Second, the rigid body inertia can be modelled better, using elemental shape functions as proposed by Shabana (1997). Since these shape functions can define large rigid body motion accurately, an exact formulation of the rigid body inertia can be obtained by using an intermediate element coordinate system. The concept of the intermediate element coordinate system is similar to the parallel axis theorem currently used in the research, and its orientation with respect to the body frame can be simply defined with a constant transformation matrix. Third, it was assumed in that the rotational inertia about all three axes are decoupled. In other words, the system is assumed to be rotating about its principle axis. However, on examination of Envisat's attitude, it was declared that Envisat is not tumbling about its principle axes (Virgili, 2014) and there is coupling between all three axes of rotation. Therefore, for a more realistic analysis, the coupling between these axes should be modelled and analysed. Fourth, more efficient ways of adding structural and active damping to the system can be examined. Lastly, for a better understanding of the dynamics, the different components of energy in the system, including elastic and dissipative energies, can be studied in further detail.

8.2.4. Control System

In this research, the controllers were used in elementary forms and no optimisation was performed to improve their performance. Therefore, there is a big scope of improvement in the control system design. The performance of more advanced linear and nonlinear controllers like Linear Quadratic Regulator (LQR), Simple Adaptive Controller, and so on, can also be analysed for this test case. Additionally, other control strategies associated with control of tumbling bodies can be explored. For instance, sequential axis control, *i.e*, control of each single axis in a sequence can be attempted. Further, the effect of sensor measurement errors can be added. Since in the stacked system, the actuators are present only on the chaser body, control allocation of the actuators in the presence of flexible perturbations is another interesting extension for the research. Also, a sensitivity can be performed to study the effect of using impulsive actuators, like thrusters compared to the momentum control devices like Control Moment Gyros (CMGs) and reaction wheels. Then, options for adding active damping to control the flexible vibrations can be explored. Lastly, the controllability characteristics of the system when the FMD is included in the control system design can be studied. This can be done in many ways, for instance, using sensors to measure the vibrations in the

panel. Another option is to use the predicted values of flexible vibrations from the ground tests in the controller, by adding dedicated bending filters.

8.2.5. Numerical aspects

The simulator used for this research was developed in MATLAB®, which proves to be computationally more demanding than other computing languages like C++ and Python. Translating the simulator to such faster languages can improve the performance considerably. The integration algorithm (VODE) can be better understood to fine tune the algorithm. This can be achieved by performing a sensitivity study on the effect of absolute and relative tolerances, and integration stepsize. Lastly, an additional option of including the Jacobian matrix in the integrator must be considered. According to Brown et al. (1989), this option decreases the computation time by 12% by saving and reusing the matrix (under specific conditions), instead of recomputing it every timestep.

Bibliography

[1] Likins, P. W. Analytical dynamics and nonrigid spacecraft simulation. 1974.

[2] Meirovitch, L. *Computational Model of Structural Dynamics*. Sijthoff and Noordhoff, The Nederlands, 1980.

[3] Meirovitch, L. *Elements of Vibration Analysis*. McGraw-Hill, New York, 1986.

[4] Jonker, J. *Dynamics of Spatial Mechanisms with Flexible Links*. Delft University of Technology, Netherlands, 1988.

[5] Cardona, A. An integrated approach to mechanism analysis. 1990.

[6] Shuster, M. D. A survey of attitude representations. *Navigation*, 8(9):439–517, 1993.

[7] Grewal, A. K. S. *A study of flexible space structures: dynamics and control*. PhD thesis, University of British Columbia, 1994.

[8] Ghosh, T. International space station thermally induced solar array base loads, 1997.

[9] Shabana, A. A. Flexible multibody dynamics: review of past and recent developments. *Multibody system dynamics*, 1(2):189–222, 1997.

[10] Wie, B. *Space vehicle dynamics and control*. AIAA, 1998.

[11] Levine, W. S. *Control system applications*. CRC press, 1999.

[12] Cardona, A. Superelements modelling in flexible multibody dynamics. *Multibody System Dynamics*, 4(2-3):245–266, 2000.

[13] Johnson, N. L. The new jettison policy for the international space station. *Advances in Space Research*, 38(9):2077–2083, 2006.

[14] NASA. Handbook for limiting orbital debris. 2008.

[15] IADC. Space debris: Iadc assessment report for 2011. 2011.

[16] ESA. Concurrent design facility study report, 2012.

[17] Irvine, T. Effective modal mass & modal participation factors revision d. 2013.

[18] Orr, J. S. Optimal recursive digital filters for active bending stabilization. 2013.

[19] Preumont, A. *Twelve lectures on structural dynamics*, volume 198. Springer, 2013.

[20] Shabana, A. A. *Dynamics of multibody systems*. Cambridge university press, 2013.

[21] Virgili, S. L. H. K., B. Bastida. Investigation on envisat attitude motion, 2014.

[22] ESTEC, N., ESA. e.deorbit mission requirements document, 2014.

[23] ESTEC, N., ESA. e.deorbit implementation plan, 2015.

[24] Habets, J. *Evolving Systems Approach to the Attitude Control of a Large-Space-Debris Removal Spacecraft*. Delft University of Technology, 2015.

[25] Deloo, J. *Analysis of the rendezvous phase of e. Deorbit: guidance, communication and illumination*. Delft University of Technology, 2015.

[26] Biesbroek, R. Envisat information document, 2017.

[27] Dwarshuis, K. *Geometric Stiffness Formulation for a Superelement*. University of Twente, 2017.

[28] ESTEC, N., ESA. The rosetta mission: Flight operations, 2017.

[29] ESA. *Active Debris Removal*, 2017. URL `https://www.esa.int/Our_Activities/Operations/Space_Debris/Active_debris_removal`.

[30] Stramaccioni, E. N., D. The rosetta propulsion system, 2017.

[31] Sola, J. Quaternion kinematics for the error-state kalman filter. *arXiv preprint arXiv:1711.02508*, 2017.

[32] van de Wetering, B. *Velocity forces and mass terms in new floating frame formulation*. University of Twente, 2018.

[33] Kessler, D. J. and Cour-Palais, B. G. Collision frequency of artificial satellites: The creation of a debris belt. *Journal of Geophysical Research: Space Physics*, 83(A6):2637–2646, 1978.

[34] Junkins, J. L. and Kim, Y. *Introduction to Dynamics and Control of Flexible Structures*. AIAA Education Series, American Institute of Aeronautics and Astronautics, Inc., Washington, DC, 1993. ISBN 1563470543. ISBN-1-56347-054-3.

[35] Geradin, M. and Cardona, A. *Flexible multibody dynamics: a finite element approach*, volume 2. Wiley New York, 2001.

[36] Wasfy, T. M. and Noor, A. K. Computational strategies for flexible multibody systems. *Applied Mechanics Reviews*, 56(6):553–613, 2003.

[37] Memi, E. and Deason-Sharp, T. Motion control subsystem, 2006.

[38] Hassmann, C. H. G. and Fenili, A. Attitude and vibration control of a satellite with a flexible solar panel using lqr tracking with infinite time. In *Proceedings of the ASME International Congress of Mechanical Engineering*, 2007.

[39] Liu, X. and Tavakoli, M. Inverse dynamics-based adaptive control of nonlinear bilateral teleoperation systems. In *Robotics and Automation (ICRA), 2011 IEEE International Conference on*, pages 1323–1328. IEEE, 2011.

[40] Géradin, M. and Rixen, D. J. *Mechanical vibrations: theory and application to structural dynamics*. John Wiley & Sons, 2014.

[41] Linskens, H. and Mooij, E. Tether dynamics analysis and guidance and control design for active space-debris removal. *Journal of Guidance, Control, and Dynamics*, pages 1232–1243, 2016.

[42] Deng, M. and Yue, B. Nonlinear model and attitude dynamics of flexible spacecraft with large amplitude slosh. *Acta Astronautica*, 133:111–120, 2017.

[43] Ellenbroek, M. and Schilder, J. On the use of absolute interface coordinates in the floating frame of reference formulation for flexible multibody dynamics. *Multibody system dynamics*, pages 1–16, 2017.

[44] Mooij, E. and Gransden, D. I. The effect of sloshing on the controllability of a conventional aeroelastic launch vehicle. In *AIAA SciTech Forum, Guidance, Navigation, and Control Conference, San Diego*. AIAA, 2019.

[45] Rutkovsky, V., Sukhanov, V., and Dodds, S. Definition and dynamic portrait of large space structures for control system synthesis. *WIT Transactions on The Built Environment*, 22, 1970.

[46] Rutkovsky, V., Sukhanov, V., and Dodds, S. Definition and dynamic portrait of large space structures for control system synthesis. *WIT Transactions on The Built Environment*, 22, 1970.

[47] Santini, P., Ottens, H., Mead, D. J., Baldacci, R. F., Phillips, E., Degener, M., and Wada, B. Damping effects in aerospace structures. Technical report, ADVISORY GROUP FOR AEROSPACE RESEARCH AND DEVELOPMENT NEUILLY-SUR-SEINE (FRANCE), 1979.

[48] Gill, P. E., Murray, W., Saunders, M. A., and Wright, M. H. Some theoretical properties of an augmented lagrangian merit function. Technical report, STANFORD UNIV CA SYSTEMS OPTIMIZATION LAB, 1986.

[49] Fujimori, Y., Kato, J., Motohashi, S., Kuwao, F., and Sekimoto, S. Modal damping measurement of mos-1 solar array paddle. In *Automatic Control in Space 1985*, pages 121–125. Elsevier, 1986.

[50] Brown, P. N., Byrne, G. D., and Hindmarsh, A. C. Vode: A variable-coefficient ode solver. *SIAM journal on scientific and statistical computing*, 10(5):1038–1051, 1989.

[51] Foist, B., Grau, E., and Nejad, B. Launch loads development using sine vibration methodology. In *45th AIAA/ASME/ASCE/AHS/ASC Structures, Structural Dynamics & Materials Conference*, page 1800, 2004.

[52] Singla, P., Mortari, D., and Junkins, J. L. How to avoid singularity for euler angle set? In *2004 Space Flight Mechanics Meeting Conference*, pages 04–190, 2005.

[53] Schlee, K., Gangadharan, S., Ristow, J., Sudermann, J., Walker, C., and Hubert, C. Advanced method to estimate fuel slosh simulation parameters. In *41st AIAA/ASME/SAE/ASEE Joint Propulsion Conference & Exhibit*, page 3596, 2005.

[54] Meguro, A., Ishikawa, H., and Tsujihata, A. Study on ground verification for large deployable modular structures. *Journal of spacecraft and rockets*, 43(4):780–787, 2006.

[55] Sieberling, S., Chu, Q., and Mulder, J. Robust flight control using incremental nonlinear dynamic inversion and angular acceleration prediction. *Journal of guidance, control, and dynamics*, 33(6):1732–1742, 2010.

[56] Fufa, B., Zhao-Bo, C., and Wensheng, M. Modeling and simulation of satellite solar panel deployment and locking. *Information Technology Journal*, 9(3):600–604, 2010.

[57] Oda, M., Hagiwara, Y., Suzuki, S., Nakamura, T., Inaba, N., Sawada, H., Yoshii, M., and Goto, N. Measurement of satellite solar array panel vibrations caused by thermal snap and gas jet thruster firing. In *Recent Advances in Vibrations Analysis*. InTech, 2011.

[58] Elliott, K. B., Horta, L. G., Templeton, J. D., Knight, N., and Song, K. Model calibration efforts for the internationalspace station's solar array mast. In *53ra AIAA/ASME/ASCE/AHS/ASC Structures, Structural Dynamics and Materials Conference, Honolulu*, 2012.

[59] Virgili, B. B., Lemmens, S., and Krag, H. Investigation on envisat attitude motion. In *e. Deorbit Workshop*, 2014.

[60] Teoh, V. C., Shahriman, A. B., Norhizam, H., Sazali, Y., Ruslizam, D., and Rakhmad Arief, S. Comparison on the rigid and flexible model of attitude maneuvering of a simple multi-body satellite. 2014.

[61] Kucharski, D., Kirchner, G., Koidl, F., Fan, C., Carman, R., Moore, C., Dmytrotsa, A., Ploner, M., Bianco, G., Medvedskij, M., et al. Attitude and spin period of space debris envisat measured by satellite laser ranging. *IEEE Transactions on Geoscience and Remote Sensing*, 52(12):7651–7657, 2014.

[62] Godard, B., Budnik, F., Muñoz, P., Morley, T., and Janarthanan, V. Orbit determination of rosetta around comet 67p/churyumov–gerasimenko. In *Proceedings 25th International Symposium on Space Flight Dynamics–25th ISSFD, Munich, Germany*, 2015.

[63] Corso, M., Lampariello, R., Rackl, W., and Gasbarri, P. *Modelling, Dynamic Analysis and Robotic Control Strategies for the Deorbiting Operations of the ESA Satellite Envisat.* PhD thesis, Institut für Robotik und Mechatronik, 2016.

[64] Schilder, J., Ellenbroek, M., and de Boer, A. Superelements in a minimal coordinates floating frame of reference formulation. 2018.

A

Skew Symmetric Matrix

A skew-symmetric matrix $\tilde{\boldsymbol{a}}$ associated with an algebraic vector $\boldsymbol{a} = [a_x \; a_y \; a_z]^T$ is defined as:

$$\tilde{\boldsymbol{a}} = \begin{bmatrix} 0 & -a_z & a_y \\ a_z & 0 & -a_x \\ -a_y & a_x & 0 \end{bmatrix} \tag{A.1}$$

The tilde ("~") symbol on the vector $\boldsymbol{a}$ indicates that the components of the vector are used to generate a 3×3 skew-symmetric matrix. The vice-versa can be written for a 3×3 matrix of skew-symmetric form, given by:

$$\boldsymbol{B} = \begin{bmatrix} 0 & b_{12} & b_{13} \\ -b_{12} & 0 & b_{23} \\ -b_{13} & -b_{23} & 0 \end{bmatrix} = \tilde{\boldsymbol{b}} \tag{A.2}$$

So, for $\boldsymbol{B} = \tilde{\boldsymbol{b}}$, the elements of vector $\boldsymbol{b}$ become $b_x = -b_{23}, b_y = b_{13}$ and $b_z = -b_{12}$. Therefore, the matrix $\boldsymbol{b}$ can be written as:

$$\boldsymbol{b} = [-b_{23} \quad b_{13} \quad -b_{12}]^T \tag{A.3}$$

A vector cross-product $\boldsymbol{c} = \boldsymbol{a} \times \boldsymbol{b}$ can be written in algebraic vector form as:

$$\boldsymbol{c} = \tilde{\boldsymbol{a}}\boldsymbol{b} = \begin{bmatrix} a_y b_z - a_z b_y \\ a_z b_x - a_x b_z \\ a_x b_y - a_y b_x \end{bmatrix} \tag{A.4}$$

Therefore, the tilde operator provides an algebraic representation, which is a convenient and computationally efficient formulation of vector products. Some additional properties of the skew-symmetric matrix are:

- Transpose:

$$\tilde{\boldsymbol{a}}^{\boldsymbol{T}} = -\tilde{\boldsymbol{a}} = \begin{bmatrix} 0 & a_z & -a_y \\ -a_z & 0 & a_x \\ a_y & -a_x & 0 \end{bmatrix} \tag{A.5}$$

- Multiplication with a scalar quantity, α:

$$\alpha\tilde{\boldsymbol{a}} = \begin{bmatrix} 0 & -\alpha a_z & \alpha a_y \\ \alpha a_z & 0 & -\alpha a_x \\ -\alpha a_y & \alpha a_x & 0 \end{bmatrix} = \widetilde{\alpha \boldsymbol{a}} \tag{A.6}$$

- Multiplication with another vector, $\boldsymbol{b}$

$$\tilde{\boldsymbol{a}}\boldsymbol{b} = -\tilde{\boldsymbol{b}}\boldsymbol{a} \tag{A.7}$$

- Multiplication with associated vector:

$$\tilde{\boldsymbol{a}}\boldsymbol{a} = (\tilde{\boldsymbol{a}}\boldsymbol{a})^T = \boldsymbol{a}^T\tilde{\boldsymbol{a}}^T = -\boldsymbol{a}^T\tilde{\boldsymbol{a}} = 0 \tag{A.8}$$

- Addition with another skew-symmetric matrix:

$$\widetilde{(\boldsymbol{a}+\boldsymbol{b})} = \tilde{\boldsymbol{a}} + \tilde{\boldsymbol{b}} \tag{A.9}$$

- Transformation from one frame (E_j) to another frame (E_i):

$$(\tilde{\boldsymbol{a}}^j) = \boldsymbol{R}_i^j\tilde{\boldsymbol{a}}^i\boldsymbol{R}_j^i \tag{A.10}$$

B

Proof of Assumption for Rotation Matrices

To understand the rotation matrix, first its algebraic properties should be discussed. As stated before, the rotations in this research are finite. Therefore, $\boldsymbol{C}$ is a 3×3 matrix, with three independent parameters to define rotation. These characteristics constitute the special orthogonal group, SO(3), also called Lie group of proper orthogonal linear transformations represented by (Cardona, 1990):

$$SO(3) = \{C : \boldsymbol{C}^3 \rightarrow \mathscr{C}^{\mathbf{3}} \mid \boldsymbol{C}^{\boldsymbol{T}}\boldsymbol{C} = \boldsymbol{I},\ \det(\boldsymbol{C}) = +1\} \tag{B.1}$$

Another concept closely associated with the Lie Groups is, Lie Algebra. It consists of real skew symmetric matrices that represent a corresponding set of infinitesimal rotations. The essential geometric link between the Lie group and Lie algebra that should be understood is that the Lie Algebra is depictive of the tangent space to the Lie Group, which can be visualised in Figure B.1. The map (or projection) from tangent space to the Lie Group is called exponential map. Another description for this would be; the Lie Algebra is the linearisation of the Lie Group about the identity point (For instance, P_j in Figure B.1) and the exponential map is the delinearisation back to Lie group. This operation is required because, rotations are objects in a non-linear manifold, like SO(3) in this case. Since SO(3) cannot be defined in vector space, the rotations cannot be interpolated (Cardona, 1990). Therefore, computations would require introduction of a tangential vector space to account for the increments in the rotation matrix $\boldsymbol{C}$.

According to Ellenbroek and Schilder (2017), when the deformations are small, the rotation matrix, $\boldsymbol{C}^{\boldsymbol{i}}_{\boldsymbol{j}}$ can be directly related to the nodal rotations $\boldsymbol{\theta}^{\boldsymbol{i},\boldsymbol{i}}_{\boldsymbol{j}}$, because in case of linear theory, all parametrisations of $\boldsymbol{C}^{\boldsymbol{i}}_{\boldsymbol{j}}$ yield the same results. This can be projected on the non-linear model by

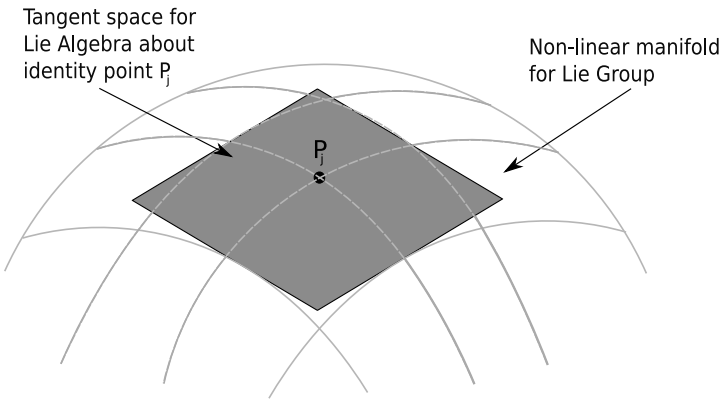

Figure B.1: Visualisation of tangent space on Lie Group

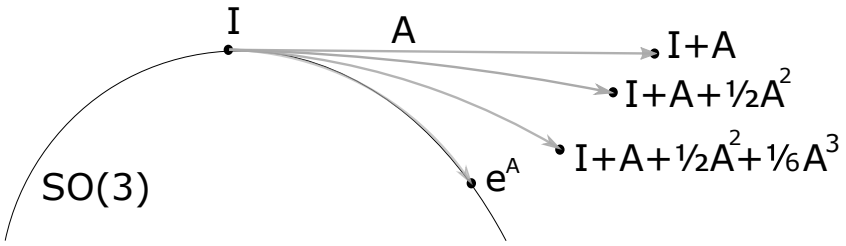

Figure B.2: Visual example of exponential mapping

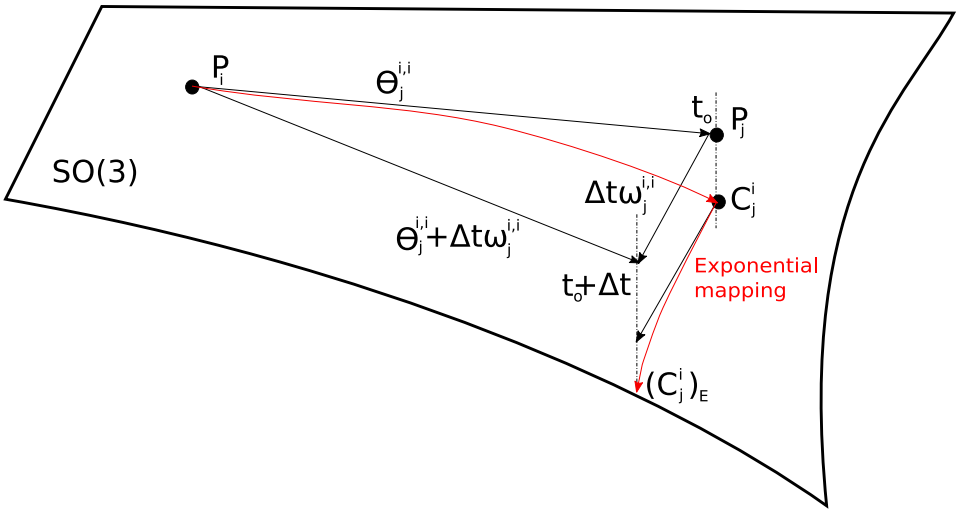

Figure B.3: Exponential mapping for rotation of point P_j

performing Taylor series expansion for exponential mapping, given by the general equation:

$$e^A = \sum_{n=0}^{\infty} \frac{1}{n!} A^n \tag{B.2}$$

This can be visualised in Figure B.2, which shows how the exponential mapping transforms from linear to a non-linear formulation with the addition of terms in the Taylor series. A more specific and simplified formulation for exponential mapping of the SO(3) group (also known as Rodrigues rotational formulation) is provided in Sola (2017), using which $\boldsymbol{C}_j^i$ can be approximated at time, $t = t_0 + \Delta t$ about undeformed configuration, given by:

$$(\boldsymbol{C}_j^i)_E = \boldsymbol{C}_j^i\,(\boldsymbol{\theta}_j^{i,i} + \Delta t.\boldsymbol{\omega}_j^{i,i}) = \exp(\tilde{\boldsymbol{\theta}}_j^{i,i} + \Delta t.\tilde{\boldsymbol{\omega}}_j^{i,i}) \approx \boldsymbol{I}_{3,3} + \tilde{\boldsymbol{\theta}}_j^{i,i} + \Delta t.\tilde{\boldsymbol{\omega}}_j^{i,i} \tag{B.3}$$

where $\tilde{\boldsymbol{\omega}}_j^{i,i}$ (a skew-symmetric matrix)is the local angular velocity of point P_j with respect to the floating frame at $t = t_0$. The vector representation of Equation (B.3) can be visualised in Figure B.3. For small Δt, the equation remains valid, and the nodal rotations, $\tilde{\boldsymbol{\theta}}_j^{i,i}$ at $t = t_0$ can be approximated by inverting the exponential map, or in other words, by applying a logarithmic mapping (Sola, 2017). This can be denoted by:

$$\mathrm{Log}: SO(3) \rightarrow \mathscr{so}(3); \boldsymbol{C} \rightarrow \ln(\boldsymbol{C}) = \boldsymbol{u}\theta \tag{B.4}$$

where,

$$\boldsymbol{u} = \frac{(\boldsymbol{C}_j^i - \boldsymbol{C}_j^{iT})}{2\sin\theta} \tag{B.5}$$

Considering very small Δt in Equation (B.3) gives:

$$\ln(\boldsymbol{C}_j^i) = \tilde{\boldsymbol{\theta}}_j^{i,i} \tag{B.6}$$

Using Equations (B.4), (B.5) and (B.6), the final expression for nodal rotations can be derived in terms of rotation matrix as:

$$\tilde{\boldsymbol{\theta}}_j^{\boldsymbol{i},\boldsymbol{i}} \approx \frac{1}{2}(\boldsymbol{C}_j^{\boldsymbol{i}} - \boldsymbol{C}_j^{\boldsymbol{i}\boldsymbol{T}}) \tag{B.7}$$

At $t = t_0$, the time derivative of $\tilde{\boldsymbol{\theta}}_j^{\boldsymbol{i},\boldsymbol{i}}$ will be approximately equal to the local angular velocity vector.